

STUDIES OF PULSAR POPULATIONS:
SEARCHING, TIMING,
AND MODELING

by

Jason Boyles

Dissertation submitted to
the Faculty of
the Department of Physics of
West Virginia University
in partial fulfillment of
the requirements for
the degree of
Doctor of Philosophy

2011

Advisory Committee:
Dr. Duncan Lorimer, Chair
Dr. Maura McLaughlin
Dr. James Lewis
Dr. Daniel Pisano
Dr. Tom Wilson

ABSTRACT

Title of dissertation: **STUDIES OF PULSAR POPULATIONS:
SEARCHING, TIMING, AND MODELING**

Jason Boyles, Doctor of Philosophy, 2011

Dissertation directed by: Dr. Duncan Lorimer
Department of Physics
West Virginia University

Pulsars are interesting astronomical objects in their own right but, they are also great instruments to use for astronomy. Their clock-like periodicity allows them to be used to study the interstellar medium, detect gravitational waves, and study binary evolution. In this work we take a look at a general view of the pulsar population through searching for new pulsars, measuring the properties of pulsars through a technique called pulsar timing, and modeling of the pulsar population using Bayesian techniques.

We took advantage of the immobilization of the Robert C. Byrd Green Bank Telescope during the track refurbishing to search the sky for radio pulsars at a frequency of 350-MHz. This survey has excellent sensitivity off the Galactic plane but suffers from scattering and dispersion measure smearing in the Galactic plane. So far in this survey we have found 26 new pulsars including five millisecond pulsars of which some have become interesting sources that have been studied across the electro-magnetic spectrum.

Rotating radio transients have interesting emission that is periodic but is not always apparent using normal pulsar techniques. These sources may represent a new part of the spectrum of neutron stars but present difficulties in studying them. Here we present some properties of five rotating radio transients and some comments on how they relate to normal radio pulsars.

Globular clusters host a large number of millisecond pulsars which is expected due to the stellar evolution of the globular cluster, but also have a few pulsars much younger than the globular cluster itself. We examined this population of younger pulsars putting constraints of the possible total population and examined the globular clusters for evidence of how they could be formed without massive progenitors that are needed for core collapse supernovae. The most likely scenario is accretion induced collapse of a O-Ne-Mg white dwarf.

Acknowledgments

This journey could not have been completed alone, and thus many people deserves my thanks and gratitude for their help along the way.

I would like to first start off with my committee chair Dr. Duncan Lorimer. Without his knowledge, guidance, and encouragement this journey may have not taken place.

Next I would like to thank my co-adviser Dr. Maura McLaughlin. Though our points of view differed sometimes, she always helped and kept my best interests in mind.

Next I would like to acknowledge my remaining committee members, Dr. D. J. Pisano, Dr. James Lewis, and Dr. Thomas Wilson, and commend them on enduring what seemed to be the longest oral examination in history.

Of course none of this could be possible without the Physics department of West Virginia University and all of its dedicated employees. Our department chair Dr. Earl Scime gave me the opportunity to come and work here and worked to improve and expand the department especially to add astronomy research to the department. The office staff, Sherry, Siobhan, Devon, Sandy, Amy, and Lori, who all are very helpful and enjoyable people to work with.

I would also like to thank the late Dr. Jack Littleton. Without his many years of dedication work within the University involving astronomy, the department may have never seen the days where astrophysics is a major research area here at WVU.

Many collaborators have helped and influenced my work, and deserve to be

mentioned. This is a long list but I would personal like to thank our former post-doc Dr. Vlad Kondratiev, and his many hours of assistance at the beginning of my career, Dr. Joris Verbiest, for his many interesting and useful hours of pulsar and non-pulsar related discussion, and Dr. Scott Ransom for his software packages and hands-on help learning how to use his software and operating the Green Bank Ultimate Pulsar Processing Instrument (GUPPI).

I have spent many hours in my windowless office of Hodges 111 and would like to thank Josh R., Josh M., Mitch, Ben, and Priya for their immediate availability to help me when I knew they had the knowledge needed and I did not, and for their conversation when my mind would wander.

Apart from the many hours in Hodges 111, some were spent playing team trivia on Fridays nights and these people helped me relax and realize that there is more to life then just sitting at a computer. Thanks Josh, Steph, Will, Kelly, Sam, Evan, Matt, and Peter for our many accomplishments we obtained in the pursuit of using our knowledge for fun.

Last but not least, I would like to thank my loving Mother, Kathryn Boyles. Without her years of working crappy shifts, putting a roof over my head, and food on the table none of this other thanks would be needed. Thanks Mom.

Table of Contents

List of Tables	vi
List of Figures	viii
List of Abbreviations and Symbols	xi
1 Introduction	1
1.1 Pulsar Basics	1
1.2 Propagation Effects	5
1.3 Types of Pulsars	10
1.3.1 Normal pulsars	10
1.3.2 Millisecond Pulsars	12
1.3.3 Rotating Radio Transients	13
1.4 Pulsar Searching	14
1.4.1 De-dispersion	14
1.4.2 Frequency Domain Searches	15
1.4.3 Time Domain Searches	16
1.4.4 Acceleration Searches	17
1.4.5 Radio Frequency Interference	18
1.4.6 Candidate Selection	19
1.5 Pulsar Timing	20
1.6 Outline of Thesis	27
2 A 350-MHz Drift-scan Pulsar Survey with the GBT.	36
2.1 Introduction	36
2.2 Survey Observations	39
2.3 Discovery Analysis	48
2.4 Timing Observations and Analysis	53
2.5 Other measured parameters	58
2.5.1 820 MHz Fluxes	58
2.5.2 Rotation Measures	59
2.5.3 Pulse Widths at 820 MHz	59
2.6 Discussion	60
2.6.1 PSR J1327–0755	62
2.6.2 PSR J1623–0841	62
2.6.3 PSR J1737–0814	63
2.6.4 PSR J1941+0121	64
2.6.5 PSR J2222–0137	64
2.7 Conclusions and Future Work	68

3	Timing Observation of RRATs	79
3.1	Introduction	79
3.2	Timing and Analysis Techniques	80
3.2.1	TOAs	80
3.2.2	Pulse Profiles and Widths	82
3.3	Timing Results	84
3.3.1	PSR J1623–0841	84
3.3.2	PSR J1739–2521	87
3.3.3	PSR J1754–3014	87
3.3.4	PSR J1839–0141	88
3.3.5	PSR J1848–1243	90
3.4	Summary and Further Work	92
4	Young Radio Pulsars in Galactic Globular Clusters	98
4.1	Introduction	99
4.2	The current sample of young pulsars in GCs	101
4.3	Sensitivity limits for young pulsars in GCs	103
4.4	The potentially observable population of young pulsars in GCs	105
4.5	The intrinsic population and birth rates of young GC pulsars	108
4.5.1	Results for all GCs	108
4.5.2	Metal-rich GCs	110
4.6	Discussion	111
4.6.1	Flux Luminosity Limits	111
4.6.2	Birth Rates in GCs	112
4.6.3	Role of cluster metallicity	113
4.6.4	Formation scenarios	114
4.6.4.1	Blue Stragglers	114
4.6.4.2	Electron Capture Supernovae	115
4.6.4.3	Galactic Bulge Pulsars	117
4.6.5	Suggested Future Work	121
5	Conclusions and Future Work	132
5.1	Green Bank 350-MHz surveys	132
5.2	Rotating Radio Transients	134
5.3	Globular Cluster Pulsars	135
5.4	Next Generation Radio Telescopes	135

List of Tables

1.1	Parameter file for J1939+2134 created using the ATNF pulsar catalog. For a listing of each parameter's definition see the TEMPO website (http://tempo.sourceforge.net).	22
1.2	An example TEMPO TOA files for J2111+2108 showing one year's worth of TOAs with the TOAs being in Princeton format.	23
2.1	Observations	42
2.1	cont.	43
2.1	cont.	44
2.1	cont.	45
2.1	cont.	46
2.1	cont.	47
2.2	Start MJD, total time, azimuth, elevation, and data number of bits for each observation.	47
2.3	Table of parameters for DM searched during data processing. Each de-dispersed time series was processed using 128 subbands.	48
2.4	Post-gridding best-fit positions of pulsars. ΔP is the difference between the true position and the discovery and post-gridding positions.	54
2.5	Observational parameters for timing observations.	56
2.6	RVM model fit results for PSR J1941+0121. Here ϕ_0 is the pulse phase of magnetic meridian, ψ_0 is position angle at ϕ_0 , α is the colatitude of magnetic axis, and ζ is the colatitude of the observer's line of sight.	65
2.7	Timing and derived parameters for newly discovered pulsars.	70
2.8	Timing and derived parameters for newly discovered pulsars.	71
2.9	Timing and derived parameters for newly discovered pulsars.	72
2.10	Timing and derived parameters for newly discovered pulsars.	73
2.11	Timing and derived parameters for newly discovered pulsars.	74
2.12	Timing and derived parameters for newly discovered pulsars.	75
2.13	Timing and derived parameters for newly discovered PSR J2222–0137.	
	76	
3.1	Table containing all observations of PSR 1839–0141. Integer MJDs have no detection of PSR 1839–0141 in either periodicity searches or singlepulse searches.	89
3.2	Table containing the discovery position and final position for five RRATs. PSR J1739–2521 and J1839–0141 were both discovered outside the FWHM of the telescope beam size of their survey. PSR J1623–0841 was discovered at 350 MHz with the GBT and its beam is $\sim 36'$	90
3.3	Fitted and derived parameters for newly discovered RRATs.	93
3.4	Fitted and derived parameters for newly discovered RRATs.	94
3.5	Fitted and derived parameters for newly discovered RRATs.	95

4.1	The four young pulsars currently known in GCs	103
4.2	Parameters for Bulge Globular Clusters. D_{GC} is the distance from the Galactic center and D is the distance from the Sun to the Globular cluster.	118
4.3	Parameters for globular clusters searched for pulsars. GC parameters from Harris (1996).	128
4.3	Continued	129
4.4	Binomial analysis of young pulsars in globular clusters.	130
4.4	Continued	131

List of Figures

1.1	Frequency dependent time delay in the pulse arrival due to ISM effects. The sloped vertical black lines are the pulses from the pulsar, parts of three pulses are shown.	5
1.2	Profile of 431 ms PSR B1900–06 at a DM of 195 pc cm^{-3} showing the $1/e$ scattering tail induced by the pulses traveling through the ISM.	7
1.3	The measured distribution of P and \dot{P} for all known pulsars. Data are taken from the ATNF pulsar catalog (Manchester et al. 2005).	11
1.4	Top: Time series of a fake pulsar created with a period of 0.975 s and a pulse width of 24%. The individual pulses can not be seen. Bottom: FFT of the time series with only the first 2000 FFT bins shown for clarity. The first and second harmonics are clearly visible.	28
1.5	Single pulse search output of PSR J1754–30. The top middle and top right plots show excess number of detections at the DM of the pulsar while the bottom plot shows detections as a function of time and DM with circle size being proportional to signal-to-noise of the pulse. In this observation, about a dozen pulses can be seen centered around a DM of 99 pc cm^{-3}	29
1.6	A set of diagnostic plots for an observation of PSR J2221–01. The left hand side shows a pulse profile at the top and a plot of intensity versus time and pulse phase on the bottom. Along the plot of intensity versus time is a plot of χ^2 versus time. The middle top plot shows frequency versus pulse phase and the bottom shows χ^2 versus DM. The right hand side (from top to bottom) shows χ^2 versus period, χ^2 versus \dot{P} , and an intensity plot of period- \dot{P} phase space.	30
1.7	An example of a weak redetected pulsar in the 350-MHz drift-scan survey. B1829–08 has a period of 647 ms and a DM of 301 pc cm^{-3} and pulse scattering has reduced the pulsar’s signal to almost an undetectable level.	31
1.8	Example of pure noise showing none of the characteristics of a detected pulsar.	32
1.9	A diagnostic plot showing a 1.2 s RFI signal. Besides the plot of significant versus DM, this plot shows all the characteristics of a pulsar.	33
1.10	Timing residuals for PSR B1133+16. (a) Shows a timing model with no systematics and a random distribution of TOAs indicating a good model fit. (b) Timing model showing the parabolic signature of underestimating \dot{P} by 4%. (c) Timing model showing the constant amplitude yearly sinusoidal signature of a offset in position (here 1 arcmin in declination). (d) Timing model showing the linearly increasing amplitude, yearly sinusoidal signature of not including proper motion in the timing model. Figure used with permission from the Handbook of Pulsar Astronomy (Lorimer & Kramer 2005).	34

1.11	A sinusoidal fit to the barycentered data for PSR J2222–0137. The fit is slightly imperfect due to the pulsar’s non-zero orbital eccentricity.	35
2.1	A plot in equatorial coordinates showing the sky coverage of the survey. The PSC portion is shown in gray and the red line shows the Galactic plane. New discoveries presented in this paper are shown as red stars.	40
2.2	Single pulse search output showing the discovery observations of new pulsar J2111+2108.	51
2.3	Example of the search output diagnostic plot for newly discovered pulsar J2222–0137. Left-hand side shows a pulse profile at the top and a plot of intensity versus time on the bottom. Along the plot of intensity versus time is a plot of χ^2 versus time. The middle top plot show frequency versus pulse phase and the bottom shows χ^2 versus DM. The right hand-side (from top to bottom) shows χ^2 versus period, χ^2 versus \dot{P} , and an intensity plot of period– \dot{P} phase space.	52
2.4	Example fit for RM for PSR J1941+0121.	60
2.5	$P - \dot{P}$ diagram showing the new discoveries as green diamonds. The lines on the plot show constant spin-down luminosity (dots), constant magnetic field (dash), and constant characteristic age (dot-dash). The pulsar population is taken for the ATNF pulsar catalog (Manchester et al. 2005).	61
2.6	RVM model fit for the radio emission of PSR J1941+0121. The top plot show parallactic angle versus pulse phase, while the bottom plot shows integrated pulse flux density versus pulse phase for total intensity (black line), linearly polarized flux (red line), and circularly polarized flux (blue line).	65
2.7	TEMPO2 simulations showing the Shapiro delay expected for PSR J2222–0137 for multiple inclination angles. The x-axis is the orbital phase of the pulsar with respect to periastron and the y-axis is the excess time delay caused by the companion as the pulsar’s signal passes through the warped space-time around the companion. From top to bottom: $i = 90^\circ$ (red), $i = 80^\circ$, (green), and $i = 70^\circ$ (blue).	67
2.8	Profiles at 820-MHz for nine newly discovered isolated pulsars created from multi-epoch data.	77
2.9	Profiles at 820-MHz for four newly discovered pulsars created from multi-epoch data.	78
3.1	A single observation plot of TOAs for PSR J1848–12 showing TOAs varying by more than the error bars on short time scales, possibly indicating that pulse jittering is occurring.	82

3.2	A $P - \dot{P}$ diagram showing the new RRATs as black triangles and previously timed RRATs as blue squares. The lines on the plot show constant spin-down luminosity (dots), constant magnetic field (dash), and constant characteristic age (dot-dash). The pulsar population is taken from the ATNF pulsar catalog (Manchester et al. 2005).	83
3.3	Two singlepulse plots for J1623–0841 at two different pointing in the sky taken at 350 MHz with the GBT. The top being offset by $20'$ and the bottom being on source.	85
3.4	Three separate observations of PSR J1739–2521 showing the intermittent nature of this source.	86
3.5	A singlepulse plot of PSR J1848–1243 (top) and a folded detection (bottom) shown.	91
3.6	Pulse profiles for PSR J1625–0841 and PSR J1754–3014 at 350 MHz and 820 MHz. The profiles are created by folding each observation and summing all profiles together.	96
3.7	Pulse profile at 820 MHz for the rest for the rest of the RRATs. Both of PSR J1739–2521 and PSR J1839–0141 profiles are a sum of data only when the pulsar is on. PSR J1848–1243’s profile is created in the same way as PSR J1625–0841 and PSR J1754–3014.	97
4.1	$P - \dot{P}$ diagram showing young globular cluster pulsars as black stars and PSR J1750–37A as a red square. PSR B2127+11A is shown as a blue arrow with the arrow representing the limit on period derivative at the bottom of the diagram. Dashed lines are lines of constant magnetic field and dot dash lines are lines of constant characteristic age. The pulsar population data are taken from the ATNF pulsar database (Manchester et al 2005).	104
4.2	Examples of discrete posterior probability density functions for the number of potentially observable pulsars in GCs using the Bayesian analysis.	123
4.3	1400 MHz luminosity survey limits as a function of metallicity with six GCs excluded with distances greater than 20 kpc. The luminosities are randomly distributed and show no bias against low or high metallicity GCs.	124
4.4	CDF of young pulsars predicted by the binomial analysis as a function of metallicity.	125
4.5	CDF of birth rate versus metallicity.	126
4.6	Histogram of number of predicted observable young pulsars per Globular Cluster using a model only dependent on the mass of the GC.	127

List of Abbreviations and Symbols

α	Rotational Axis Inclination Angle
β	Magnetic Axis Inclination Angle
η	Pulse Duty Cycle
Ω	Angular Frequency
ν	Frequency
$\dot{\nu}$	Frequency Derivative
τ_c	Characteristic Age
τ_{scat}	Scattering Time
B	Magnetic Field
b	Galactic Latitude
c	Speed of Light
CDF	Cumulative Distribution Function
DFT	Discrete Fourier Transform
DM	Dispersion Measure
e	Charge of an Electron
\dot{E}	Spin-down Luminosity
EoS	Equation of State
f	Observing Frequency
FFT	Fast Fourier Transform
GC	Globular Cluster
GHz	Gigahertz
GUPPI	Green Bank Ultimate Pulsar Processing Instrument
i	Orbital Inclination Angle
I	Moment of Inertia
ISM	Interstellar Medium
Jy	Jansky
kpc	Kiloparsec
L	Luminosity
l	Galactic Longitude
M[number]	Messier Object [number]
M_\odot	Mass of the Sun
m_e	Mass of an Electron
MHz	Megahertz
Myr	Megayear
MJD	Modified Julian Day
MSP	Millisecond Pulsar

n	Braking Index
n_e	Electron Density
NGC	New Galactic Catalog
NS	Neutron Star
P	Rotational Period
\dot{P}	Rotational Period Derivative
PMPS	Parkes Multibeam Pulsar Survey
PSR	Pulsar
PDF	Probability Density Function
R	Radius of a Neutron Star
RRAT	Rotating Radio Transient
RFI	Radio Frequency Interference
s	second
S	Flux Density
S/N	Signal-to-Noise Ratio
WD	White Dwarf

Chapter 1

Introduction

Pulsars are rapidly rotating, highly magnetized neutron stars, whose radio emission we see as a pulse as its radio beam crosses our line of sight. In the following sections, the details of pulsars will be discussed and general introduction will be provided. We pay particular attention to those properties which are the most relevant for this dissertation. For further details, see the Handbook of Pulsar Astronomy (Lorimer & Kramer 2005) and references therein.

1.1 Pulsar Basics

Pulsars are highly compact astrophysical objects. It was proposed by Baade & Zwicky (1934) that neutron stars might form during the collapse of massive stars (e.g. in supernova). The discovery of the first pulsar (CP 1919; Hewish et al. 1968) provided the first evidence that neutron stars may exist. Further theoretical work provided solid proof that only neutron stars could match the observed parameters seen in pulsar observations (Gold 1969).

The exact structure and equation of state (EoS) of neutron stars are not well understood, but observational evidence has proved some clues. The crust is a crystallized solid, probably made of iron, with a super-fluid, superconducting core. This has been deduced from glitches, sudden increases in spin period, in pulsars, most no-

ticeably the Vela pulsar (Anderson & Itoh 1975). The exact composition of the core is unknown but most models suggest a sea of mostly neutrons but some more exotic models suggestions the inner most core could be strange quark matter (Kurkela et al. 2010). Pulsars are the most dense objects in the universe outside of stellar mass black holes. EoSs predict masses (M) in the range $1.0 - 2.0 M_{\odot}$ and radii (R) of $10 - 15$ km, with $M = 1.4 M_{\odot}$ and $R = 10$ km taken as the canonical values for each parameter. The average density for a canonical pulsar ($6.7 \times 10^{14} \text{ g cm}^{-3}$) is slightly in excess of nuclear matter ($2.7 \times 10^{14} \text{ g cm}^{-3}$). Assuming a uniform spherical distribution of mass for a pulsar, a canonical value of 10^{45} g cm^2 is obtained for the moment of inertia (I).

The rotational period (P) for pulsars ranges from 1.396 ms for J1748–2446ad (Hessels et al. 2006) to 8.510 s for J2144–3933 (Manchester et al. 1996). Pulsar periods are not constant over their lifetimes and are observed to spin-down (increase in P) with time, i.e. they exhibit a rotational period derivative (\dot{P}). The distribution in P and \dot{P} is bimodal, separating pulsars in two main categories: “normal pulsars” and “millisecond pulsars”. The properties of these two types of pulsars are to follow in section 1.3.1 and 1.3.2.

The spin-down of a pulsar is the result of the star losing its rotational kinetic energy. Assuming a constant moment of inertia, I , this can be represented as:

$$\dot{E} = \frac{d}{dt} \frac{1}{2} I \Omega^2 = I \Omega \dot{\Omega}, \quad (1.1)$$

where Ω is the angular frequency. This is known as the total spin-down luminosity

of the pulsar. Inserting the canonical value for I and transforming into the more often used variables of P and \dot{P} we get

$$\dot{E} = 3.95 \times 10^{31} \text{ erg s}^{-1} \left(\frac{\dot{P}}{10^{-15}} \right) \left(\frac{P}{\text{s}} \right)^{-3}. \quad (1.2)$$

Due to conservation of magnetic flux during the supernova explosion, the surface magnetic field (B) of pulsars are predicted to range from $10^8 - 10^{14}$ Gauss (G). Though a direct measurement of the pulsar's B can not be made, an inferred value can be produced. By assuming all the spin-down energy is dominated by magnetic dipole braking, it can be shown that

$$B_S = B(r = R) = \sqrt{\frac{3c^3 I P \dot{P}}{8\pi^2 R^6 \sin^2 \alpha}}, \quad (1.3)$$

where α is the angle between the magnetic field and spin axis. Setting I and R to their canonical values and choosing the magnetic field and spin axis to be perpendicular ($\alpha = 90^\circ$), we get

$$B_S = 3.2 \times 10^{19} \text{ G} \sqrt{P \dot{P}}. \quad (1.4)$$

Caution should be taken in use of this value because the magnetic field on the surface is not uniform and should be used as only an order of magnitude estimate of the magnetic field strength.

Another order-of-magnitude estimate we can make for a pulsar is its characteristic age (τ_c). This can be derived from assuming the radiation power is equal to

the spin-down luminosity and has a power law form of

$$\nu = -K\nu^n, \quad (1.5)$$

where ν is the rotational frequency ($1/P$), $\dot{\nu}$ is the frequency derivative, K is a constant, and n is the braking index ($n = 3$ for pure dipole braking). Changing the variables to P and \dot{P} in equation 1.5 and integrating over dP we obtain the age of the pulsar

$$T = \frac{P}{(n-1)} \left[1 - \left(\frac{P_o}{P} \right)^{n-1} \right], \quad (1.6)$$

where P_o is the initial period of the pulsar. Assuming pure magnetic dipole radiation and the initial period being much less than the current period, the above equation simplifies down to the characteristic age

$$\tau_c = \frac{P}{2\dot{P}} = 15.8 \text{ Myr} \left(\frac{P}{\text{s}} \right) \left(\frac{\dot{P}}{10^{-15}} \right)^{-1}. \quad (1.7)$$

Caution needs to be taken when using the τ_c , but unlike B_S , we do have measured ages for pulsars. The Crab pulsar (B0531+21) was produced in a supernova in 1054 AD and has a τ_c of 1240 yrs. But larger differences have been seen in other pulsars (e. g. J0538+2817 Kramer et al. 2003).

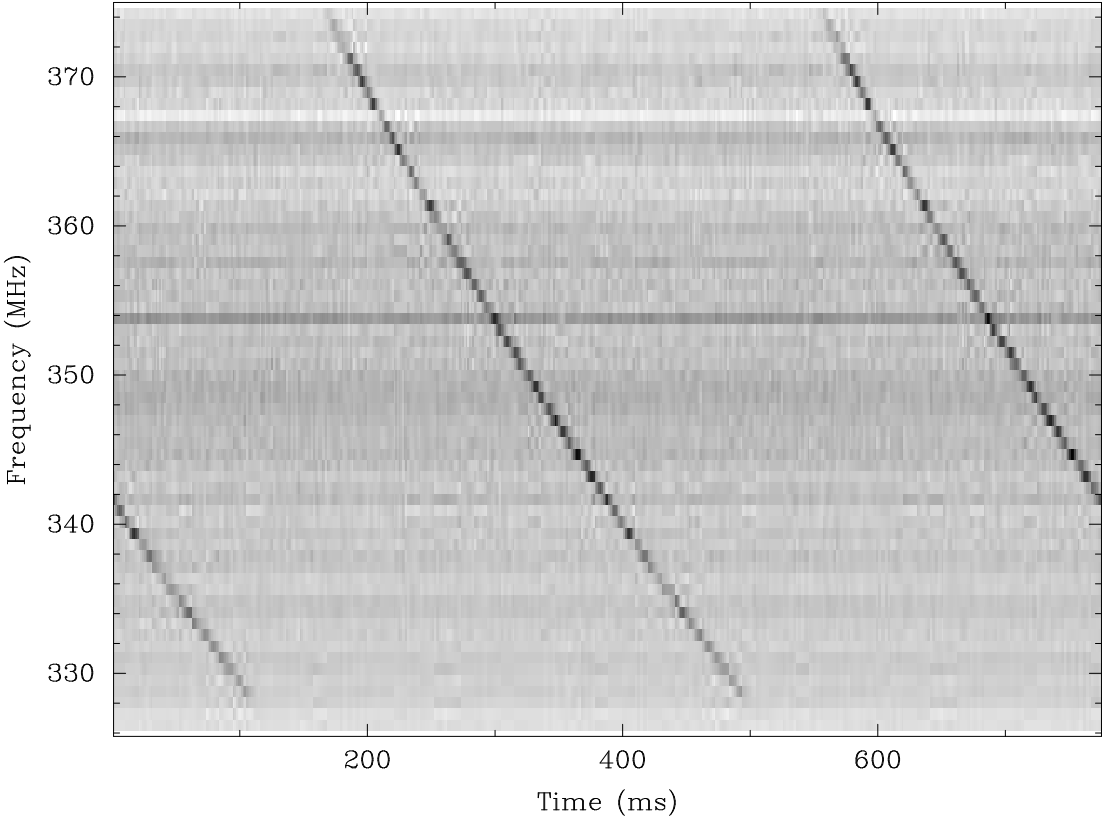


Figure 1.1: Frequency dependent time delay in the pulse arrival due to ISM effects. The sloped vertical black lines are the pulses from the pulsar, parts of three pulses are shown.

1.2 Propagation Effects

The interstellar medium (ISM) can be modeled as a cold homogeneous plasma characterized by a frequency dependent index of refraction. The dependence causes a time delay that disperses the pulsar's signal. To recover the full flux density of the pulsar, a correction must be applied to the data. The time delays between two frequencies is

$$\Delta t = 4.148808 \times 10^6 \text{ ms} \times (f_1^{-2} - f_2^{-2}) \times \text{DM}, \quad (1.8)$$

where the two frequencies, f_1 and f_2 are measured in MHz and DM is measured in

pc cm^{-3} and is given by

$$\text{DM} = \int_0^d n_{\text{e}} dl, \quad (1.9)$$

where n_{e} is the electron density along the line of sight and d is the distance to the pulsar. Figure 1.1 shows this propagation effect with the GBT at a center frequency of 350 MHz and 50 MHz of bandwidth. The DM can be used as an estimate to determine the distance to the pulsar using an electron density model of the Galaxy and the most common one used is the NE2001 electron model by Cordes & Lazio (2002) which incorporates Galactic spiral-arm structure.

The time delay across the bandwidth also occurs within individual frequency channels and is a result of a continuous signal being quantized due to finite frequency channel widths. This introduces so-called “DM smearing” within an individual frequency channel and is characterized by a smearing time scale

$$t_{\text{DM}} = 8.3 \times 10^6 \text{ms} \times \text{DM} \times \Delta f \times f^{-3}, \quad (1.10)$$

where Δf is the width of the frequency channel in MHz and f is the center frequency of the channel in MHz. When observing pulsars, careful choice needs to be made to ensure that the DM smearing is not a significant fraction of the pulse period.

Along with DM time delays, the ISM can always cause multi-path propagation of wavefront resulting in a scattering tail in pulsar’s pulse profiles. This scattering can be characterized by a $1/e$ tail on the back of the pulse profile with a time constant τ_{scat} and Figure 1.2 shows a pulsar with this scattering tail. Through this

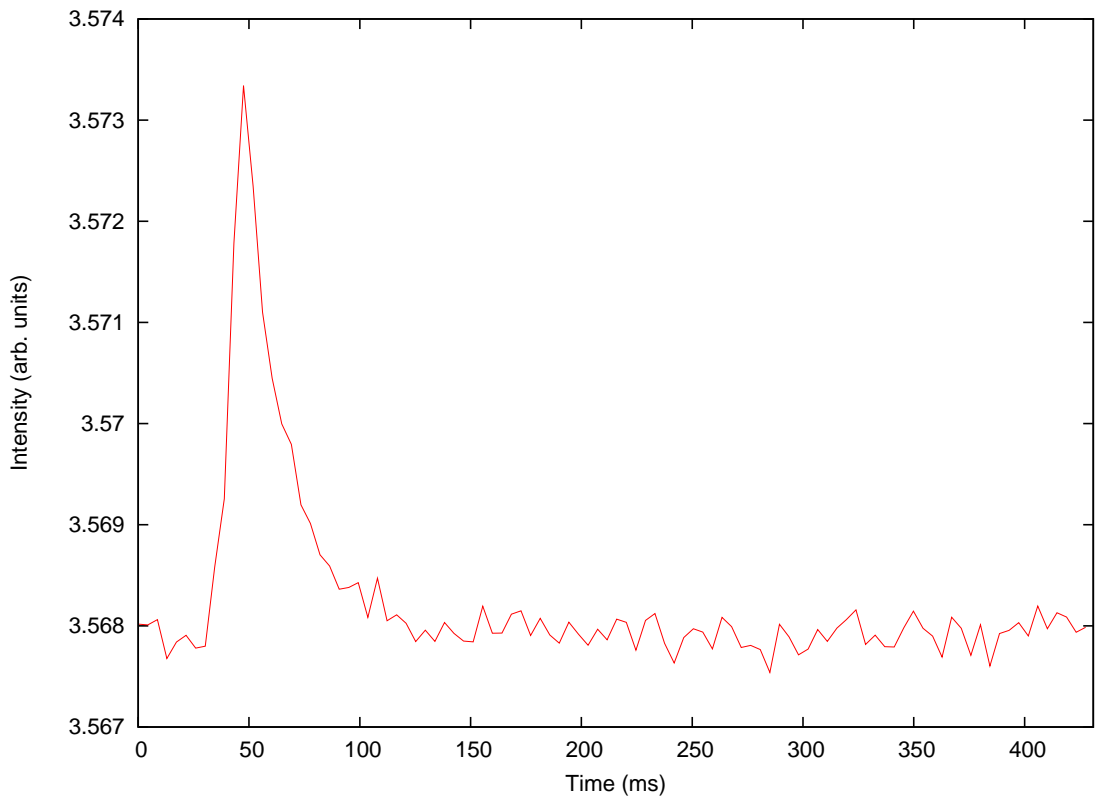


Figure 1.2: Profile of 431 ms PSR B1900–06 at a DM of 195 pc cm^{-3} showing the $1/e$ scattering tail induced by the pulses traveling through the ISM.

scattering is not uniform, it depends on frequency, DM, and the ISM in the line of sight. An empirical relationship has been derived from real data and has the form

$$\log_{10}\tau_{\text{scat}} = -6.46 + 0.154\log_{10}(\text{DM}) + 1.07(\log_{10}\text{DM})^2 - 3.86\log_{10}f, \quad (1.11)$$

where τ_{scat} is measured in ms, DM is measured in pc cm⁻³ and f is frequency measured in GHz (Bhat et al. 2004). This expression can be used to estimate the scattering time for a given observation, though the scatter between this relation and observed pulsars is quite large.

The magnetic field of the Galaxy acts as a Faraday screen causing a rotation in the position angle of polarization of the pulsar's signal. Due to pulsars being some of the most polarized astronomical sources, this effect can be seen in many pulsars. This causes a change in the polarization position angle of

$$\Delta\Psi_{\text{PPA}} = \Delta\Psi_{\text{Faraday}}/2 = \lambda^2 \times \text{RM}, \quad (1.12)$$

where λ is wavelength and the rotation measure (RM) is defined as

$$\text{RM} = \frac{e}{2\pi m_e^2 c^4} \int_0^d n_e B_{||} dl, \quad (1.13)$$

where e is the charge of the electron, m_e is the mass of the electron, c is the speed of light, and $B_{||}$ is the average Galactic magnetic field along the line of sight. A measurement of DM and RM will provide the average magnetic field strength along

the line of sight, but caution needs to be taken using this measurement. The electron density is not homogeneous and the magnetic field can change directions which may results in incorrect interpretation of the measurement if not treated properly.

Many types of scintillation exist, weak and strong, refractive and diffractive, but here we are going to address the one that dominates the observations presented in the dissertation, strong diffractive scintillation. Diffractive interstellar scintillation (DISS) shows up as strong intensity variations in both time and frequency. DISS is caused by diffraction of electromagnetic radiation as it travels through the ISM creating constructive and destructive interference patterns analogue to the interference patterns in the double and single slit experiment. These patterns have measurable properties that can be used to understand the ISM through which the radiation passed through.

Two characteristic quantities can be measured from the dynamic spectrum of a pulsar. The first is a timescale

$$\Delta t_{\text{DISS}} = \frac{s_o}{V_{\text{ISS}}}, \quad (1.14)$$

where s_o is the field coherence scale and V_{ISS} is the transverse velocity of the pulsar and the other is a frequency scale

$$\Delta f_{\text{DISS}} = \frac{1.16}{2\pi\tau_{\text{scat}}}, \quad (1.15)$$

for a Kolmogorov spectrum. With both Δt_{DISS} and Δf_{DISS} measured from a dynamic spectrum, a transverse velocity

$$V_{\text{ISS}} = A \left(\frac{d}{\text{kpc}} \right)^{1/2} \left(\frac{\Delta f_{\text{DISS}}}{\text{MHz}} \right)^{1/2} \left(\frac{f}{\text{GHz}} \right)^{-1} \left(\frac{\Delta t_{\text{DISS}}}{\text{s}} \right)^{-1} \quad (1.16)$$

can be measured. Here d is the distance to the pulsar, f is the frequency of the observation, and A is a constant whose value varies from author to author but has a value in the few thousand kilometers per second range. For most pulsar observations diffractive scintillation is a hindrance but it has been used to help discover pulsars only detectable during DISS maximums when constructive interference increases the pulsar's flux to the point of detection. This technique has been used to detect pulsars in the globular cluster 47 Tucanae (Camilo et al. 2000).

1.3 Types of Pulsars

As stated in the previous section, pulsars can be grouped into different classes. In the following section, three types of radio pulsars will be introduced and discussed: normal pulsars, millisecond pulsars (MSPs) and rotating radio transients (RRATs). In each section the properties that make each class distinct will be discussed.

1.3.1 Normal pulsars

Normal pulsars are the most common variety of pulsar. In Figure 1.3 they are seen as the large group of pulsars clustered around a period of 1 s and \dot{P} of 10^{-15} . These pulsars have typical B between 10^{11} and 10^{13} G and τ_c between 10^6 and 10^8 years. The spin-down luminosity of normal pulsars cover the whole spectrum, with young pulsars ($\tau_c < 10,000$ yrs) being the most energetic.

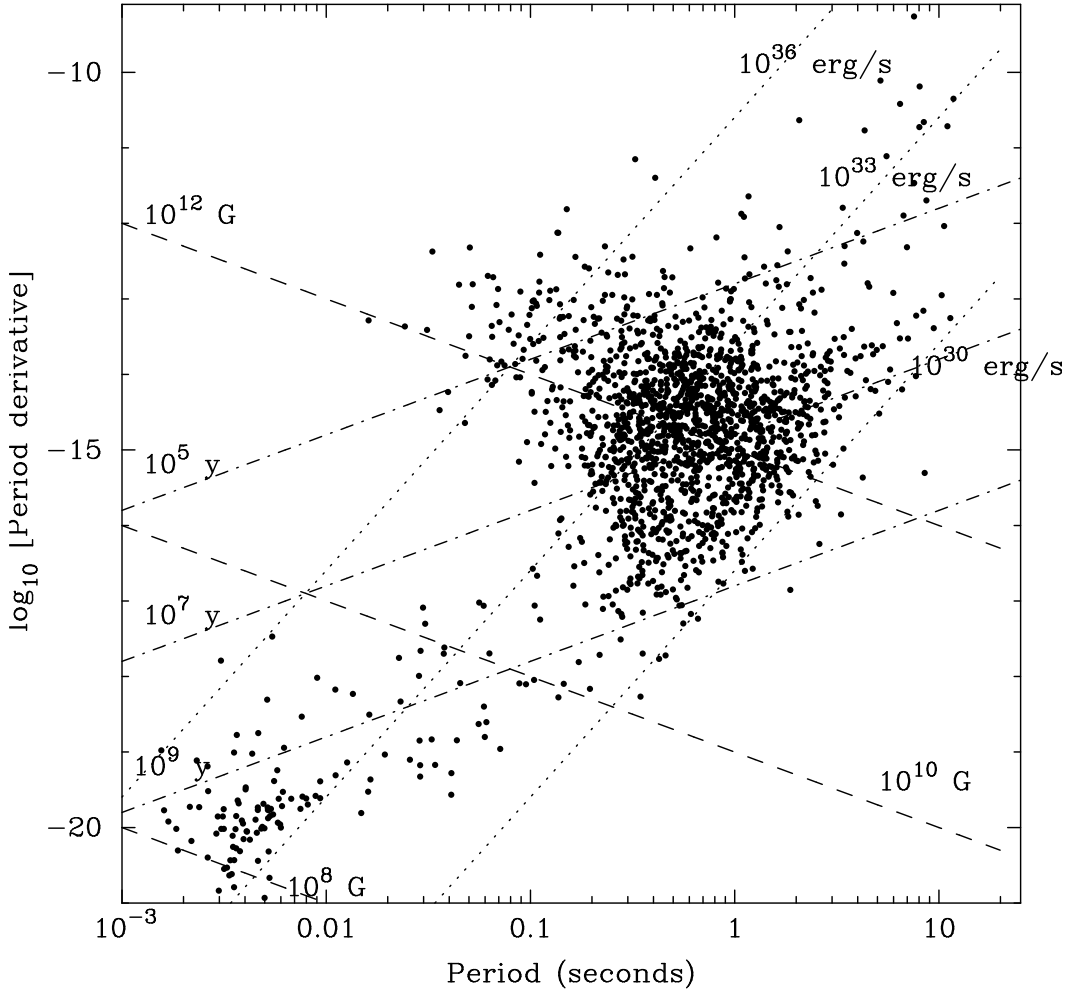


Figure 1.3: The measured distribution of P and \dot{P} for all known pulsars. Data are taken from the ATNF pulsar catalog (Manchester et al. 2005).

Many normal pulsars just have their properties measured and later are used for population studies, but some interesting ones do arise. For example J1740–3052 is a young pulsar orbiting around an $11 M_{\odot}$ star (Stairs et al. 2001), B1718–19 the first non-recycled pulsar found in a globular cluster (Lyne et al. 1993), and B0531+21 shows nanosecond duration bursts of radio emission called giant pulses (Hankins et al. 2003). Only a small fraction of normal pulsars are in binary systems; there will be a reverse of this trend when millisecond pulsars are examined.

1.3.2 Millisecond Pulsars

Millisecond pulsars (MSPs) are defined here to have periods less than 20 ms¹. As seen in Figure 1.3, MSPs have \dot{P} in the range of 10^{20} ss⁻¹, B between 10^8 and 10^9 G, and τ_c between 10^9 and 10^{12} years. The first MSP was discovered by Backer et al. (1982) and was the fastest rotating pulsar until the recent discovery of J1748–2446ad (Hessels et al. 2006). These can be seen at the bottom left corner of Figure 1.3.

Most MSPs are found in binary systems. They are thought to have been formed after a pulsar's radio emission creases and entered the pulsar graveyard (lower right corner of $P - \dot{P}$ diagram), and the companion over flows its Roche lobe and begins to accrete matter onto the pulsar. The accretion spins the pulsar up (decreases the pulsar's spin period) through the transfer of angular momentum to periods on the order of a few to tens of milliseconds. Some pulsars are only partially spun up and make up the stream of pulsars on the $P - \dot{P}$ diagram that connects the two populations together and are known are partially recycled pulsars.

The stage between being a dead pulsar and a MSP is when it is a low-mass X-ray binary (LMXB) and no radio emission is seen from the pulsar during its time as a LMXB. The recent discovery of J1023+0038 (Archibald et al. 2009) has provided us with experimental evidence of this transition from a LMXB and a radio pulsar. The origin of isolated MSPs is unknown but they could result from either the companion's supernova disrupting the binary system or the MSP destroying

¹There is no true formal definition to a MSP, some authors define them to be pulsars with periods less than 10 ms, others impose a limit of 30 ms

the companion as seen in black widow systems (Ruderman et al. 1989). Other MSP binary systems like the triple system in M3 (Backer et al. 1993), the highly eccentric Galactic binary system J1903+0327 (Champion et al. 2008), and the pulsar planetary system B1257+12 (Wolszczan & Frail 1992), pose more currently unanswered questions as to how MSP binary systems evolve.

Millisecond pulsars are known to be much more stable rotators than normal pulsars. This stability allows us to measure their properties much more precisely than that of normal pulsars. This fact has motivated large campaigns to find as many MSPs as possible with many goals in mind. Among these goals are finding the fastest spinning pulsar to help put constraints on the neutron star EoS, tests of general relativity (Taylor et al. 1992), and the detection of gravitational waves (Hobbs et al. 2010).

1.3.3 Rotating Radio Transients

The first rotating radio transients (RRATs) were discovered in a re-processing of the Parkes Multi-beam survey using a single pulse search with 11 of these presented in their discovery (McLaughlin et al. 2006). Since then about 56 RRATs in total have been discovered² and the single pulse search used to detect them has become a part of any standard search pipeline (Cordes & McLaughlin 2001).

When RRATs were initially discovered, their exact nature of them was not known. As time went on and more observations of them occurred, it became apparent that they were neutron stars with emission properties that deviated somehow

²<http://www.as.wvu.edu/~pulsar/rratalog/>

from those of normal pulsars. Many theories have been put forward to explain the RRATs including radio emission being disrupted by fall back of supernova material (Li 2006), trapped plasma being released from radiation belts (Luo & Melrose 2007), and circumstellar material interacting with the pulsar (Shannon & Cordes 2008). A less radical idea is proposed by looking at observations of B0656+14. If this pulsar were located at 12 times its current distance, it too would only be found in a single pulse search (Weltevrede et al. 2006).

Though the nature of the RRAT's emission is not understood, they are erratic radio emitters and further studies are needed to define their place among the neutron star population.

1.4 Pulsar Searching

Pulsar searching amounts to detecting signals with unknown periodicity and dispersion in noisy data sets and is a very computationally demanding task. A brief description of the standard algorithm will be discussed in the following sections.

1.4.1 De-dispersion

The ISM causes a frequency dependent time delay on the pulsar's signal across the bandwidth (shown in Figure 1.1). This effect decreases our sensitivity to finding the pulsar's signal. This effect can be correct for by breaking up the bandpass into multiple frequency channels and adding the channels together correcting with the appropriate time delay. This process is known as de-dispersion.

While searching for pulsars, the DM is unknown at the time of the searching, and many trial DMs must be tried when searching a given time series of data. As the DM value increases, scattering and DM smearing lower the effective time resolution, so it is optimal to choose DM steps with this in mind. A sensible choice is to make the dispersive delay time to be a multiple of the sampling time (τ_{samp}). Using this as a guide, the i^{th} DM is given by

$$\text{DM}_i = 1.205 \times 10^{-7} \text{cm}^{-3}\text{pc}(i - 1)\tau_{\text{samp}}(f^3/\Delta f), \quad (1.17)$$

where f and Δf are in MHz and τ_{samp} is in ms.

When the effective time smearing due to scattering and DM smearing becomes greater than τ_{samp} , the data can be decimated without loss of sensitivity to short period pulsars. This is done by simply adding consecutive time samples together and allows for faster processing of the resulting time series.

1.4.2 Frequency Domain Searches

Though the first pulsars were discovered in time domain searches looking for individual pulse trains, it quickly became apparent that searches in the frequency domain would be fruitful due to the periodical natures of pulsars. Time series data are transformed into the frequency domain via a Fast Fourier Transform (FFT). Figure 1.4 shows a time series and its resulting FFT. The pulsar is completely undetectable in the time domain, but shows up easily in the frequency domain.

To improve the sensitivity of searches, the data can be modified to help find

more legitimate candidates. Low frequency correlated red noise commonly shows up in the FFT of a time series. This can be removed by calculating a running mean, subtracting the mean off, and setting the standard deviation to unity.

For pulsars with narrower pulse widths, the higher harmonics may be used to help detect the pulsar using harmonic summing (Taylor & Huguenin 1969). This is done by stretching the FFT by factors of 2 and adding them together. The noise adds by a factor of $\sqrt{2}$ but the pulsar's signal doubles resulting in a gain of $\sqrt{2}$.

RFI can also be mitigated in the frequency domain. Frequencies of known RFI and their harmonics can be identified and removed from the data by replacing the corresponding FFT bins with the local mean to eliminate their effects on the data. This is known as birdie zapping and can also be used to eliminate the signal from a strong pulsar that may be overwhelming other potential candidates in a given data set.

1.4.3 Time Domain Searches

The first pulsars were discovered through their single pulses but this technique fell out of favor when frequency domain searches became popular. Presented in Nice et al. (1999), the single pulse search was revived and this resulted in the discovery of Rotating Radio Transients (RRATs; McLaughlin et al. 2006) and now is common to most pulsar search pipelines.

The single pulse search is accomplished by looking for events in a time series above a certain threshold. For purely Gaussian noise, the number of pulses expected

by chance above some threshold S/N_{\min} is

$$n(> S/N_{\min}) \sim 2n_{\text{samples}} \int_{S/N_{\min}}^{\infty} \exp(-x^2) dx, \quad (1.18)$$

where n_{samples} is the number of samples in the time series. Requiring $n < 3$, usually leads to $S/N_{\min} = 4$. In practice usually S/N_{\min} is chosen to be 5 or 6 because RFI or correlated signals may exist in the time series making the distribution non-Gaussian. Since the signal may be smeared due to multiple time samples occurring during a pulse, the data are smoothed (consecutive samples added together) many times and each smoothed time series is searched for events above the chosen threshold. Duplicate events that occur at the same time in many smoothings are removed and diagnostic plots like Figure 1.5 are produced from the results.

1.4.4 Acceleration Searches

Isolated pulsars show no change in their period with the time frame of a single observation, but pulsars in binary systems show a change in their period in a single observation caused by a Doppler shift due to orbital motion. This change in period results in power being spread across multiple bins in the frequency domain, hence reducing our sensitivity to them. Early techniques to correct for possible (and unknown!) change in period with time were to resample the time series with a constant acceleration and then FFT the data (Anderson 1992). This requires a new FFT for each acceleration tried and is computationally expensive. This method has been used for many years resulting in the discovery of many binary systems (see

Camilo et al 2000 for discoveries using this method).

A newer technique (and the one used in this work) is to do the correction entirely in the frequency domain and does not require a new FFT to search each acceleration for a given DM value. An inverse finite impulse response filter is applied to the Fourier coefficients which effectively gathers the power into a single Fourier bin (Ransom et al. 2002). The exact form of this filter depends on the center frequency of the Fourier bin and the number of bins being swept up into one bin. This technique is equivalent to the time domain acceleration correct but, computationally is much faster.

1.4.5 Radio Frequency Interference

Radio frequency interference (RFI) occurs in most astronomical observations even with the dedicated work of telescope personnel and the government to limit its effect on observations. Many techniques have been developed to combat RFI and can be used in various stages of data processing. One already mentioned in Section 1.4.2 is birdie zapping, where known RFI frequencies are removed from the frequency domain data.

Another common tactic is to eliminate the RFI in the raw data by applying a mask to the data. This mask is created by looking at the raw data and finding events in time or frequency that stand out above a certain threshold, which can be adjusted by the user. Using this method a whole frequency channel can be ignored if the interference is narrow band or a small chunk of data in the time domain if the

RFI is just present for a small period of time. This mask is applied to the raw data and smoothes out any places in the data that deviate greatly from a statistically mean or power.

1.4.6 Candidate Selection

After each DM for a given observation has been searched, many thousands of candidates are found that need further filtering before being looked at by a human eye. At this point, a list of candidates can be narrowed down by putting restrictions that each candidate has to be in a certain period range, a certain DM range that depends on the observation's position on the sky, or that a candidate must be detected in multiple consecutive DMs. After this winnowing, the candidates are ranked by some significant factor (usually signal-to-noise ratio) and the best candidates are then revised to create diagnostic plots to be examined by eye (shown in Figure 1.6). Figures 1.7, 1.8, and 1.9 show examples of a weakly detected pulsar, noise, and RFI. The most common plots include a folded pulse profile at the detected period, a plot of profile significant versus DM, and a two-dimensional plot of intensity versus frequency and pulse phase.

For each of the above mentioned plots, certain characteristics should be seen. For a folded pulse profile, binning the time domain data by the period of the pulsar, the profile will have a signal-to-noise ratio about the same as the Fourier amplitude found in the Fourier domain search and for most pulsars the pulse width will be less than 10% of the pulse period. The plot of profile significant versus DM, the peak

should occur at a non-zero DM near that of the most significant detected DM in the Fourier domain search. A peak at zero DM means the signal is terrestrial and is not a pulsar. The plot of intensity versus frequency and pulse phase, should show signal across the full frequency range of the observation, since pulsars are coherent emitters. Exceptions to the rules do exist for most pulsar characteristics used for discovering pulsars and a legitimate candidate can only be determined by the usage of all the information available in a given diagnostic plot.

1.5 Pulsar Timing

Pulsar timing is a powerful technique which uses the periodic nature of a pulsar to measure its properties, the companion's properties (for binaries), and even the properties of the ISM along the line of site to the pulsar. A pulsar must have an integer number of pulses between each observed pulse and pulsar timing uses this fact to produce high precision measurements of pulsar parameters that are unparalleled in other astronomical and many other physical observations.

Pulsar timing uses times of arrivals (TOAs) to obtain the properties of the pulsar, binary system, and the ISM along the line of site. The TOAs reference some fiducial point in the pulse profile which is determined by comparing the observed pulse profile to some standard template, a noiseless pulse profile that mimics the observed profile. This may be done in the time domain, but analysis has shown that this can be done more precisely in the frequency domain by Fourier transforming both the observed profile and template and sifting the Fourier transforms to match

using χ^2 minimization (Taylor 1992). This shift is then added to the start time of the observations of the pulse nearest to the center of the observation to measure a TOA.

Each parameter measurable from pulsar timing is related to a time delay that is a signature for each parameter. Figure 1.5 shows examples of the functional form when a parameter is unmodeled or off by a small percentage and these function can be related to time delays as a function of time and/or ecliptic latitude. Pulsar timing uses a χ^2 minimization process to match the TOA with the closest integer pulse in the model. A commonly used package for pulsar timing is TEMPO³ and this package is the one used for the work presented in this dissertation. TEMPO requires a list of TOAs known as a “tim” file and a parameter (“par”) file as its input (see Tables 1.1 and 1.2 for examples). The parameters for the par files are taken from the discovery observations and the value of \dot{P} is initially set to zero.

Pulsar timing is an iterative process and phase-coherent (all pulses accounted for) solutions often require a considerable amount of work. A standard procedure for timing an isolated pulsar is to follow. From a discovery observations, a rough estimate for the spin period, position, and DM can be obtained. For a starting point, three or four observations need to be taken within a week, with at least two observations on consecutive days if possible. This will form the basis to obtain a very precise measurement of the pulse period and the effects of a position error will be negligible on this short of a time scale. The next observation should occur about a week later, then a further one two weeks later. This will allow a phase coherent

³<http://www.atnf.csiro.au/research/pulsar/tempo/>

Parameter	Value	Error
PSRJ	J1939+2134	
RAJ	19:39:38.558720	2.000e-06
DECJ	+21:34:59.13745	3.000e-05
DM	71.0398	2.000e-04
PEPOCH	47899.5	
F0	641.9282611068082	1.300e-12
F1	-4.331749E-14	9.000e-20
PMRA	-0.46	2.000e-02
PMDEC	-0.66	2.000e-02
POSEPOCH	47500	
F2	4.0E-26	2.000e-27
RM	-10	9.000e+00
PX	0.12	8.000e-02
DM1	-0.0012	1.000e-04
EPHVER	2	

Table 1.1: Parameter file for J1939+2134 created using the ATNF pulsar catalog. For a listing of each parameter’s definition see the TEMPO website (<http://tempo.sourceforge.net>).

solution to be maintained while fitting for a least one additional parameter, usually one of the positions (right ascension or declination).

At this point I would like to remind the reader there is not a single path to obtaining a phase coherent solution, and fitting for one parameter or another first will not change the final outcome. After the initial set of close observations, it is common to have monthly observations and add fitting parameters as the solution begins to show any systematics. One measured parameter, DM, can be added into a timing model at any point in the process as long as multiple frequency observations have been obtained. DM can be fitted most easily at the beginning of the process when the spin period is the only other parameter to be fitted or at the end when all other parameters have been accounted for.

One digit site code	Frequency (MHz)	TOA (MJD)	Error (μs)	DM (pc cm $^{-3}$)
1	350.024	54635.1855866360913	4724.34	58.9692
1	350.024	54635.3270274613273	1218.34	58.9692
1	350.024	54635.3305967224120	763.82	58.9692
1	350.024	54635.3336626022885	1633.34	58.9692
1	350.024	54635.3368200142955	1161.67	58.9692
1	820.024	54649.1010862025466	2295.77	56.4605
1	820.024	54651.0756557255164	4225.02	56.4606
1	820.024	54655.0880919218542	2031.62	56.4608
1	820.024	54660.3650753525734	1397.15	61.1662
1	820.024	54662.0587921884389	1073.28	61.1662
1	820.024	54672.0115769060159	2182.13	61.1669
1	820.024	54672.0136819386650	1918.02	61.1669
1	820.024	54672.0603119562970	1393.80	61.1669
1	820.024	54712.9446744331688	2875.19	61.1702
1	990.024	54741.9785042888195	1184.31	62.3980
1	820.024	54771.8042972519088	1751.32	61.1738
1	820.024	54788.9349653136534	823.57	61.1741
1	820.024	54826.8261669399877	1229.77	61.1731
1	820.024	54885.5935857104819	1604.78	61.1685
1	820.024	54917.4351944806540	773.25	61.1660
1	820.024	54947.3577423199548	862.03	61.1645
1	820.024	54976.2348945594538	1476.65	61.1641

Table 1.2: An example TEMPO TOA files for J2111+2108 showing one year's worth of TOAs with the TOAs being in Princeton format.

A few techniques can be used that will minimize the uncertainties in a timing model before doing pulsar timing. The first is a process known as gridding and is used to refine the position of a pulsar. In this process, five observations are taken of a given pulsar, with the same integration times and occur on source (discovery position) and in each of the four cardinal directions with the offset being about one-half the telescope beam width at that frequency. Each time series is de-dispersed and folded at the period of the pulsar and along with right ascension and declination were used for determining the most likely position of the pulsar. The weighted means for right ascension and declination were computed using the reduced χ^2 for each profile. If a pulsar is not detected in an observation, it was not used in the weighted mean. For MSPs a better determination of DM can be obtained from a single observation where there is a large time delay compared to the period between the highest and lowest frequencies of the bandpass. This is done by simply breaking the bandpass into four separate frequency channels, creating an individual TOA for each of the four frequencies, and using TEMPO to fit these four TOAs with DM as the only unfixed parameter. This will result in about an order of magnitude more precision DM than what can be acquired working in the time domain.

The difference between timing an isolated normal pulsar and an isolated millisecond pulsar is that the pulse counts are much higher for millisecond pulsars and losing a single rotation of the pulsar is much easier to do. This can easily be overcome by properly scheduling the timing observations.

Binary pulsars need more prior information before pulsar timing can be done with them. They require at least three more parameters to be fitted for and must

be fitted from the start of the timing procedure. The additional parameters, known as the Keplerian parameters, are the orbital period P_b , the projected semi-major axis x , the epoch of periastron passage T_o , orbital eccentricity e , and longitude of periastron, ω . Of the five parameters, P_b , x , and T_o must be known prior to timing a pulsar, e and ω are unmeasurable for many binary pulsars because of their orbits being circularized during recycling.

From the Keplerian parameters, one can use Kepler's third law and obtain a mass function for the binary system

$$f(m_p, m_c) = \frac{(m_c \sin i)^3}{(m_p + m_c)2} = \frac{4\pi^2(a_p \sin i)^3}{GP_b^2} = \frac{4\pi^2x^3}{T_\odot P_b^2}, \quad (1.19)$$

where m_p and m_c are the masses of the pulsar and its companion, i is the orbital inclination angle, a_p is the size of the pulsar orbit around a common center of mass, G is the gravitational constant, T_\odot is a constant = 4.925490947 μ s. The mass function is usually expressed in solar masses. Assuming a canonical pulsar mass of 1.4 M_\odot , and $i = 90^\circ$ a minimum mass of a companion can be determined and this information can be used to plan further observations in radio and other wavelengths. A first-order estimate that can be made to obtain binary parameters is to fit the solar system barycentered periods of each observation of the pulsar to a sine wave as a function of time. This will allow for the determination of the spin period of the pulsar, the orbital period of the pulsar, the projected semi-major axis of the binary system, and the epoch of periastron. Figure 1.11 show an example of this fitting procedure for recycled pulsar PSR J2222–0137.

Along with binary parameter, Post-Keplerian parameters, general relativistic effects on the binary system's orbit, can be measured for some binary system. Expressed in their lowest post-Newtonian order, they are as follows:

$$\dot{\omega} = 3T_{\odot}^{2/3} \left(\frac{P_b}{2\pi} \right)^{-5/3} \frac{1}{1-e^2} (m_p + m_c)^{2/3}, \quad (1.20)$$

$$\gamma = T_{\odot}^{2/3} \left(\frac{P_b}{2\pi} \right)^{1/3} e \frac{m_c(m_p + 2m_p)}{(m_p + m_c)^{4/3}}, \quad (1.21)$$

$$r = T_{\odot} m_c, \quad (1.22)$$

$$s = \sin i = T_{\odot}^{-1/3} \left(\frac{P_b}{2\pi} \right)^{-2/3} x \frac{(m_p + m_c)^{2/3}}{m_c}, \quad (1.23)$$

$$\dot{P}_b = -\frac{192\pi}{5} T_{\odot}^{5/3} \left(\frac{P_b}{2\pi} \right)^{-5/3} f(e) \frac{m_p m_c}{m_{(p)} + m_c)^{1/3}}, \quad (1.24)$$

where all masses are in solar units and

$$f(e) = \frac{(1 + (73/24)e^2 + (37/96)e^4)}{(1 - e^2)^{7/2}}. \quad (1.25)$$

In the above expressions $\dot{\omega}$ is the relativistic advance in periastron, γ is the Einstein delay, r and s give the Shapiro range and shape, and \dot{P}_b being the orbital decay due to gravitational waves being emitted. Only a small fraction of binary systems have any observable Post-Keplerian parameters with the double pulsar being the only

system to have all 5 measurable (Kramer et al. 2006) and with the most common being $\dot{\omega}$.

A full description of the mathematics, formulae, and time corrections needed to do pulsar timing is behind the scope of this dissertation and for the interested reader a good introduction can be found in the Handbook of Pulsar Astronomy (Lorimer & Kramer 2005) and the reference therein.

1.6 Outline of Thesis

The goals of this work are to apply the techniques discussed in this chapter and future chapters to advance our knowledge of the pulsar population in variety of ways. Chapter 2 will discuss the observations and discovery of 13 pulsars in the GBT 350-MHz drift-scan survey. Chapter 3 will present some recent timing observations of RRATs and a brief discussion comparing them to the normal pulsar population. Chapter 4 will present an analysis of normal period pulsars in Globular Clusters and draw a conclusion on their origin and Chapter 5 will summarize the work presented in this dissertation and suggest future work.

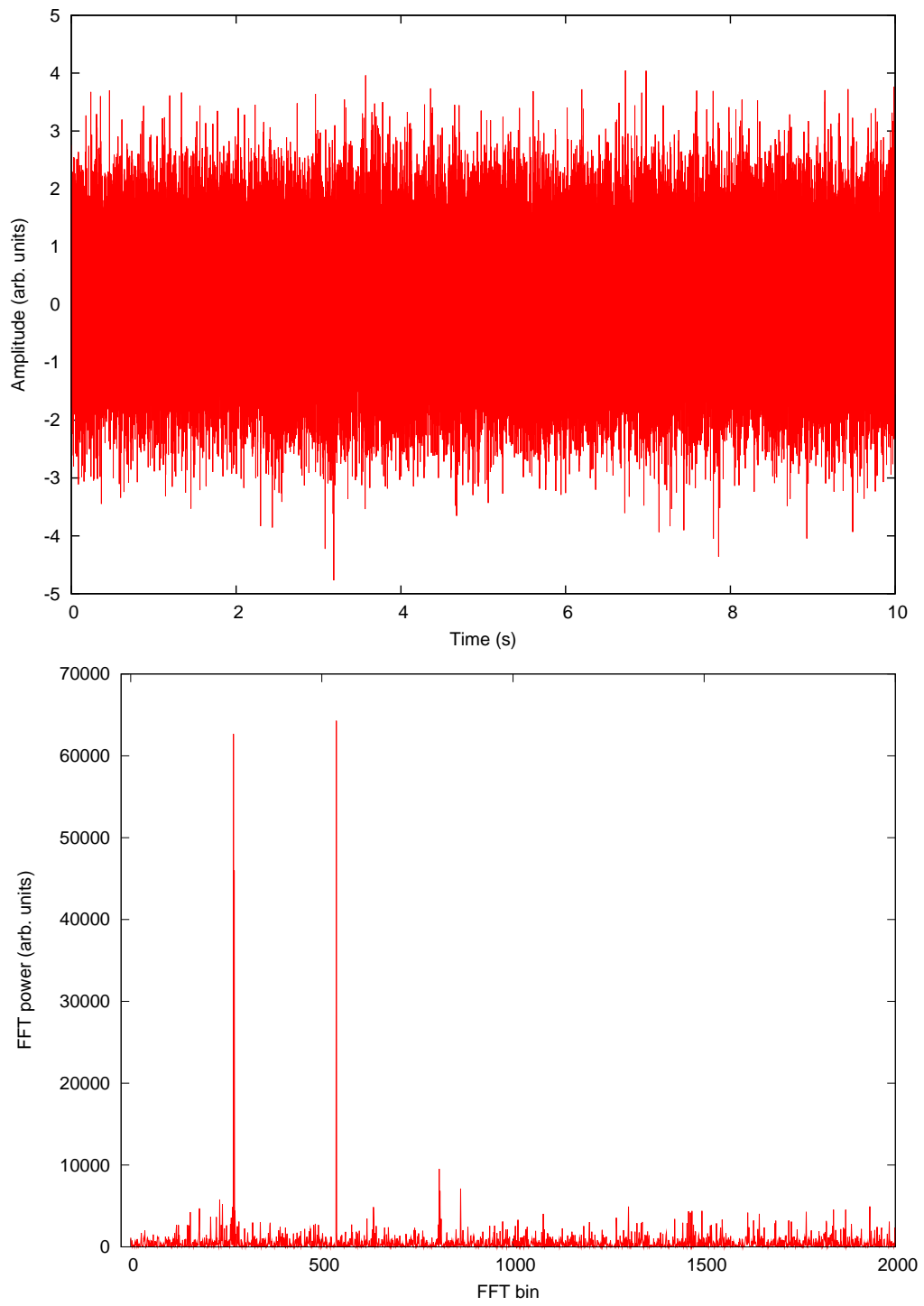


Figure 1.4: Top: Time series of a fake pulsar created with a period of 0.975 s and a pulse width of 24%. The individual pulses can not be seen. Bottom: FFT of the time series with only the first 2000 FFT bins shown for clarity. The first and second harmonics are clearly visible.

Single pulse results for 'single_J1754-30_55078_0001'

Source: 1754-30
 Telescope: GBT
 Instrument: GUPPI

RA (J2000): 17:54:15.8880
 DEC (J2000): -30:11:46.3200
 MJD_{topo}: 55078.864259259259

N samples: 7311360
 Sampling time: 245.76 μ s
 Freq_{ctr}: 350.0 MHz

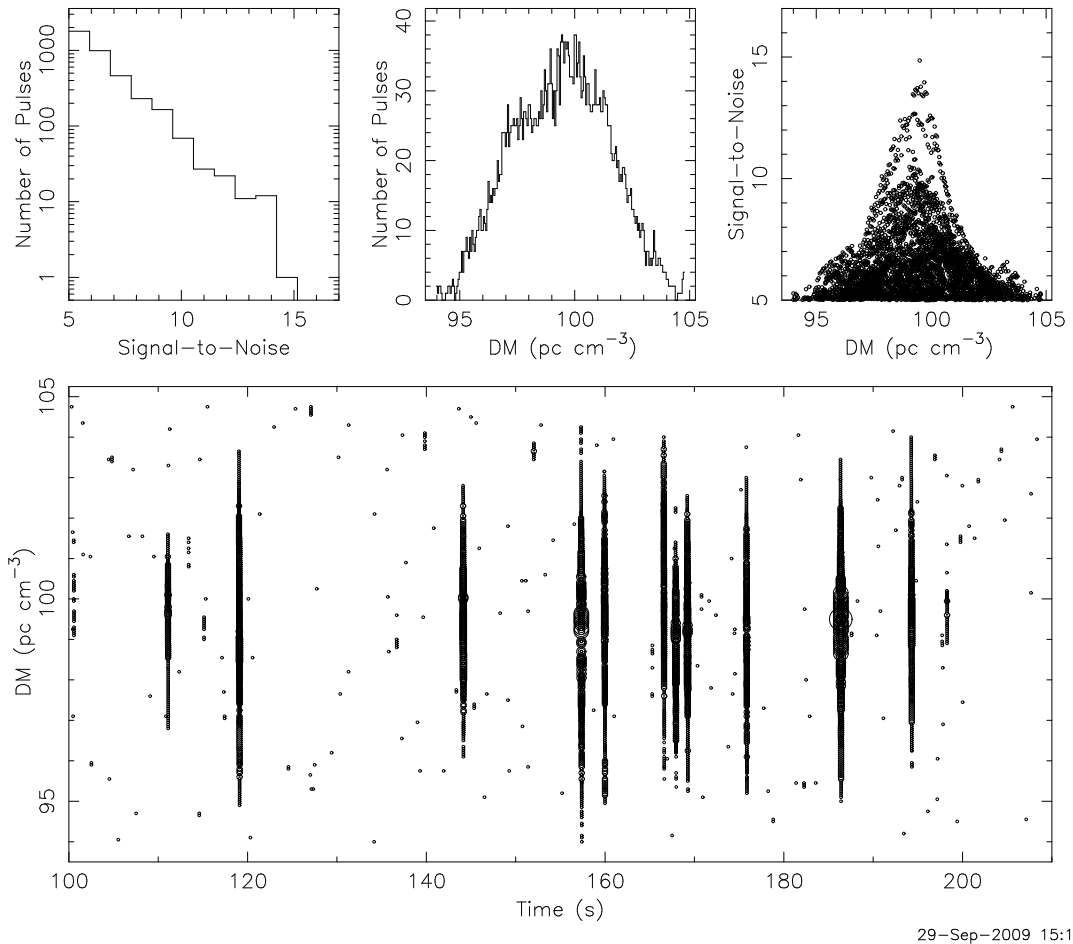


Figure 1.5: Single pulse search output of PSR J1754-30. The top middle and top right plots show excess number of detections at the DM of the pulsar while the bottom plot shows detections as a function of time and DM with circle size being proportional to signal-to-noise of the pulse. In this observation, about a dozen pulses can be seen centered around a DM of 99 pc cm^{-3} .

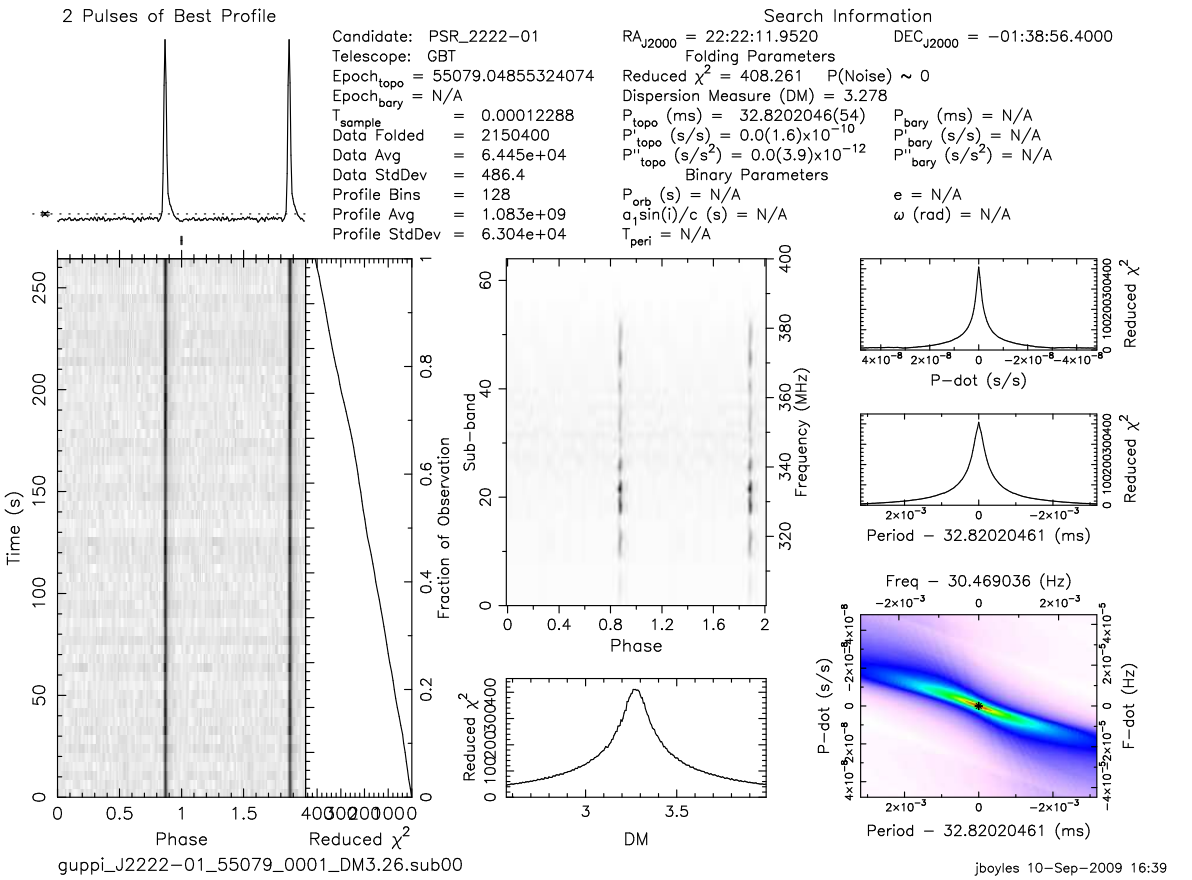


Figure 1.6: A set of diagnostic plots for an observation of PSR J2221-01. The left hand side shows a pulse profile at the top and a plot of intensity versus time and pulse phase on the bottom. Along the plot of intensity versus time is a plot of χ^2 versus time. The middle top plot shows frequency versus pulse phase and the bottom shows χ^2 versus DM. The right hand side (from top to bottom) shows χ^2 versus period, χ^2 versus \dot{P} , and an intensity plot of period- \dot{P} phase space.

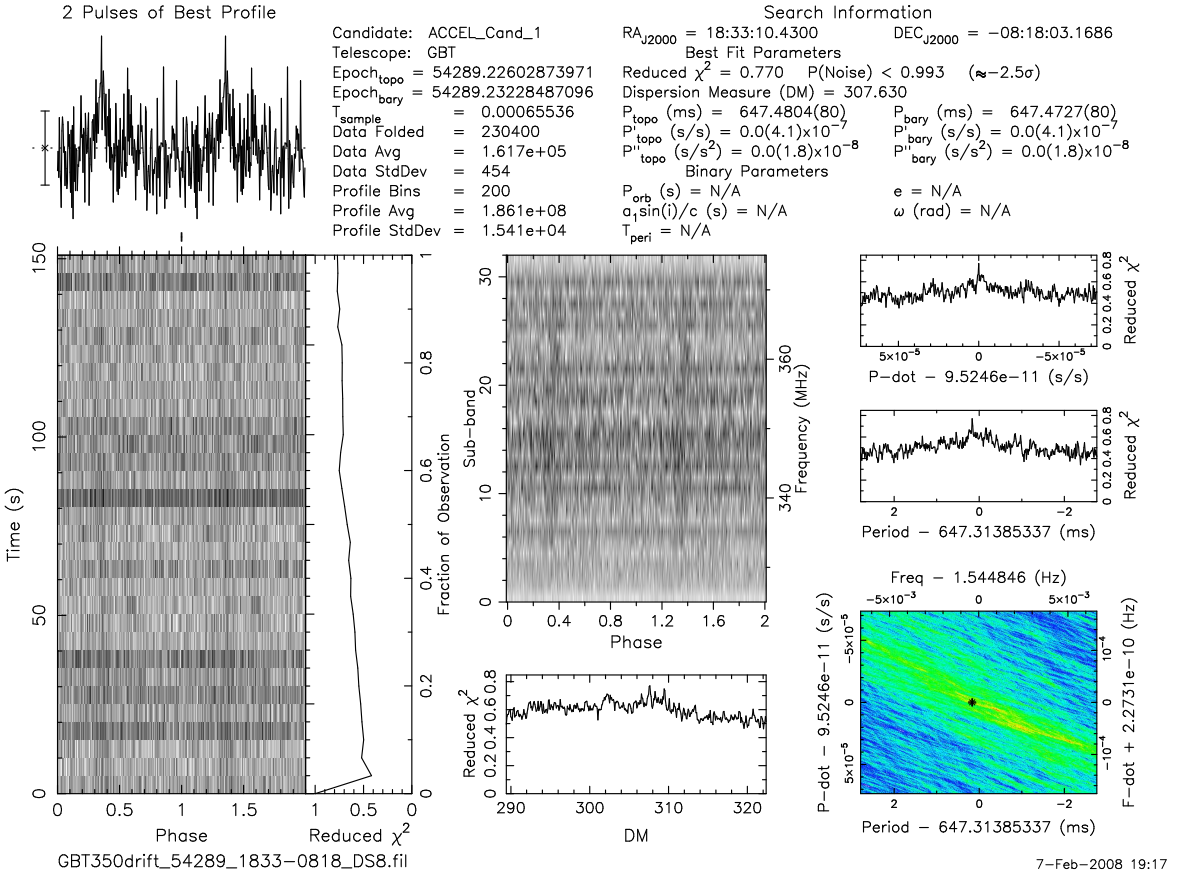


Figure 1.7: An example of a weak redetected pulsar in the 350-MHz drift-scan survey. B1829–08 has a period of 647 ms and a DM of 301 pc cm⁻³ and pulse scattering has reduced the pulsar's signal to almost an undetectable level.

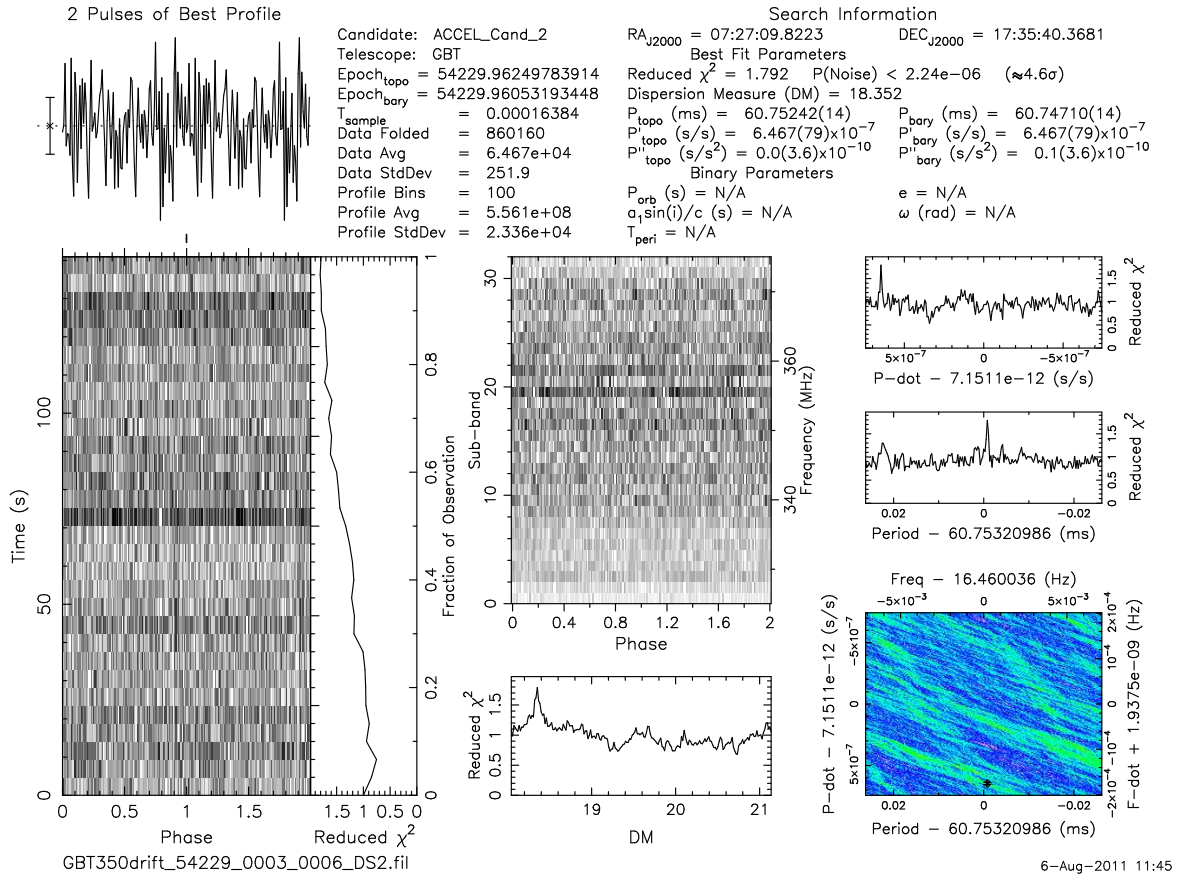


Figure 1.8: Example of pure noise showing none of the characteristics of a detected pulsar.

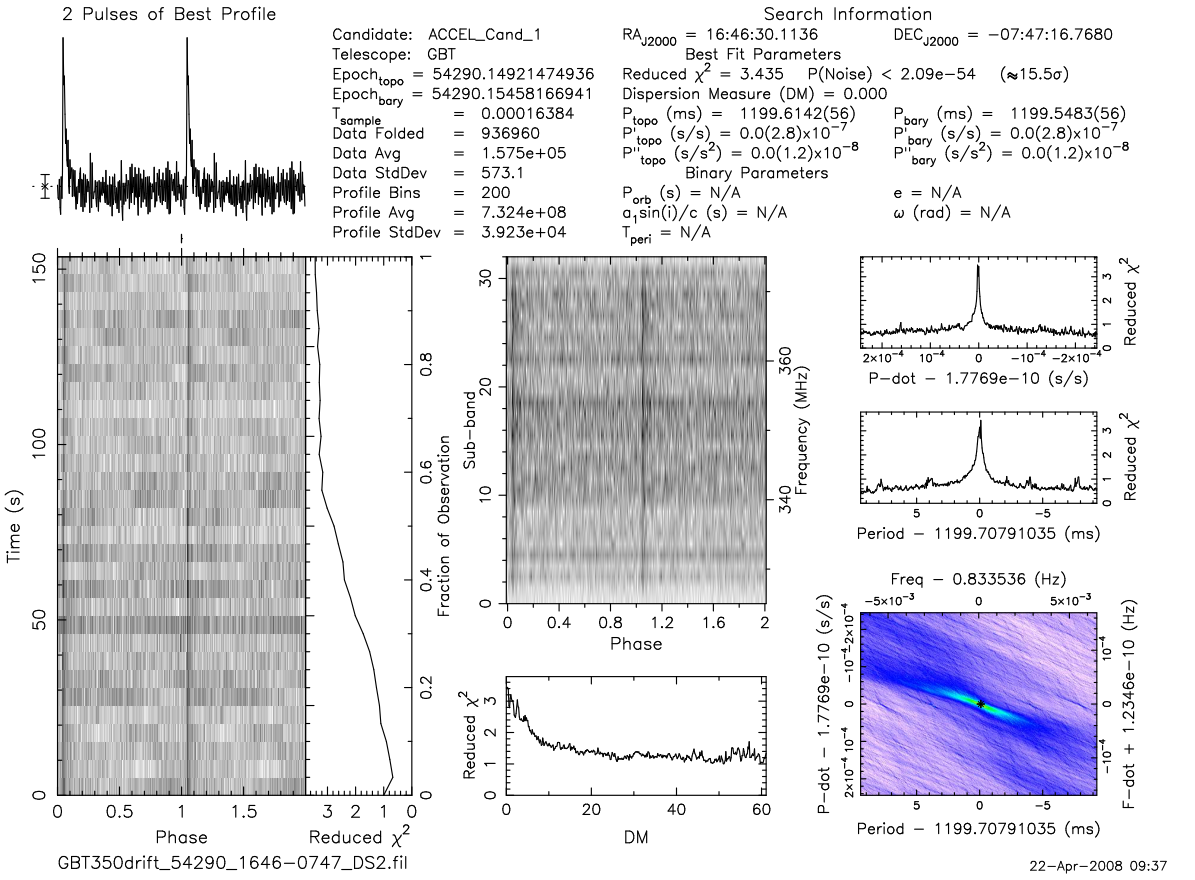


Figure 1.9: A diagnostic plot showing a 1.2 s RFI signal. Besides the plot of significant versus DM, this plot shows all the characteristics of a pulsar.

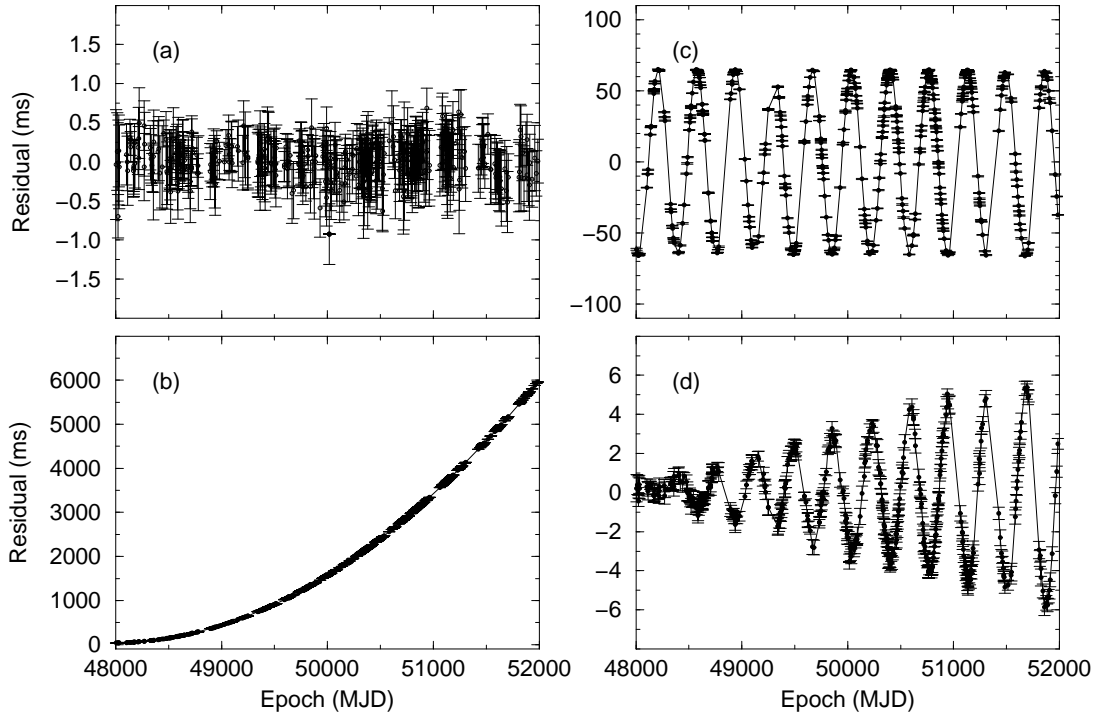


Figure 1.10: Timing residuals for PSR B1133+16. (a) Shows a timing model with no systematics and a random distribution of TOAs indicating a good model fit. (b) Timing model showing the parabolic signature of underestimating \dot{P} by 4%. (c) Timing model showing the constant amplitude yearly sinusoidal signature of a offset in position (here 1 arcmin in declination). (d) Timing model showing the linearly increasing amplitude, yearly sinusoidal signature of not including proper motion in the timing model. Figure used with permission from the Handbook of Pulsar Astronomy (Lorimer & Kramer 2005).

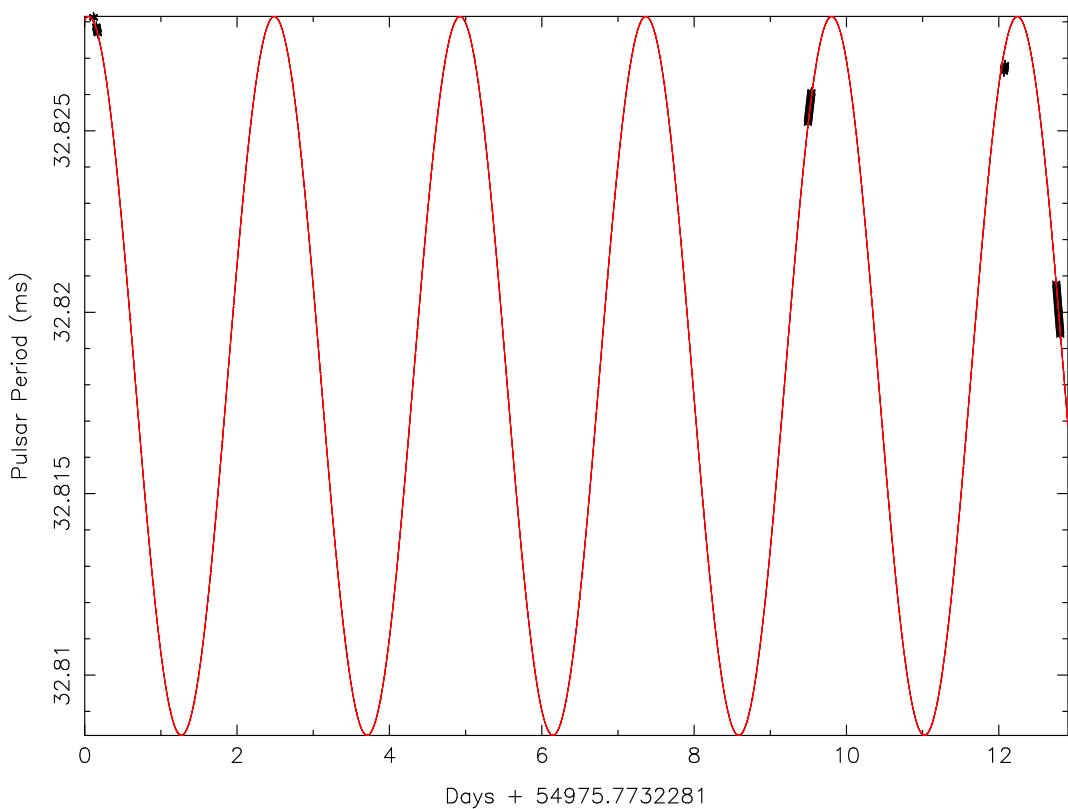


Figure 1.11: A sinusoidal fit to the barycentered data for PSR J2222–0137. The fit is slightly imperfect due to the pulsar’s non-zero orbital eccentricity.

Chapter 2

A 350-MHz Drift-scan Pulsar Survey with the GBT.

Abstract

Over the summer of 2007, we obtained 1191 hours of ‘drift-scan’ data with the GBT to search for pulsars at a low radio frequency of 350 MHz. Here we describe the survey setup, search procedure, and present the discovery and follow-up timing of 13 pulsars. Of these thirteen pulsars, PSR J1623–0841 was discovered only through its single pulses, two are millisecond pulsars (PSR J1327–0755 and PSR J1737–0814), and another, PSR J2222–0137, is a mildly recycled pulsar. J1327–0755 is a 2.7 ms pulsar at a DM of 27.9 pc cm^{-3} in a 8.7 day orbit with a minimum mass companion of $0.22 M_{\odot}$. PSR J1737–0814 is a 4.2 ms pulsar at a DM of 55.3 pc cm^{-3} in a 79.3 day orbit with a minimum mass companion of $0.06 M_{\odot}$. PSR J2222–0137 is a 32.8 ms pulsar at a DM of 3.27 pc cm^{-3} in a 2.4 day orbit with a minimum mass companion of $1.11 M_{\odot}$ and could possibly be a low eccentricity double neutron system.

2.1 Introduction

Since the discovery of the first pulsar in 1967 (Hewish et al. 1968), many fascinating discoveries and experiments have been associated with pulsars. These

include but are not limited to tests of general relativity (Lyne et al. 2004), studies of binary evolution (Phinney 1993), probes of electron density models of the interstellar medium (Cordes & Lazio, 2002), constraints on the neutron star equation of state (Lattimer & Prakash 2001), and use in a pulsar timing array for gravitational wave detection (Hobbs et al. 2010).

Searches for pulsars are very demanding, requiring both significant amounts of computational and human resources. The high time and frequency resolution needed for pulsar searches result in data rates greater than for most astronomical projects (typically 100 GB/hr or more). Large computing clusters are needed to thoroughly search for both periodic and transient dispersed signals. After all the computer searching is complete, candidates are typically inspected with the human eye to determine legitimate pulsar candidates, though automated algorithms, such as neural nets, are becoming increasingly important for sifting through large numbers of candidate signals (e.g., Eatough et al. 2010).

Most modern large scale non-targeted pulsar surveys (Parkes Multi-beam Pulsar Survey; Manchester et al, 2001, High Time Resolution Universe Pulsar Survey; Bailes et al. 2010, PALFA; Cordes et al. 2006), occur around 1.4 GHz and target the Galactic plane. The choice of 1.4 GHz is to limit the effects of the interstellar medium on pulsar observations. Lower frequency observations (< 500 MHz) are better used to locate weak sources away from the Galactic plane where the effects of scattering and dispersion boarding are minimized.

The National Radio Astronomy Observatory (NRAO) at Green Bank, WV has a long history of successful searches for radio pulsars at low frequencies. Damashek

et al. (1978) discovered 17 new pulsars with the 92 meter transit telescope at a frequency of 400 MHz. Later, using the same telescope at a frequency of 390 MHz, Dewey et al. (1985) found 34 new long period pulsars but was not sensitive to newly discovered millisecond pulsars (MSPs; $P < 20$ ms; Backer et al. 1982). The first low-frequency survey to be sensitive to MSPs was conducted by Stokes et al. (1985) at 390 MHz. While this survey did not discover any MSPs, it did find 20 new long period pulsars. Sayer et al. (1997) used the 43 meter telescope at Green Bank at a frequency of 370 MHz and discovered 8 new pulsars including one MSP. New backend software and higher data rates now allow frequency resolution that was previously unattainable by previous observing systems. Most recently, a Galactic plane survey was conducted with the Robert C. Byrd Green bank Telescope¹ (GBT) by Hessels et al. (2008) at 350 MHz and discovered 33 new pulsars, none of which are MSPs. Our survey took advantage of a unique opportunity when GBT was immobilized for track refurbishing during the northern summer of 2007. During this time, we recorded data at a radio frequency of 350 MHz as the sky passed through the beam of the telescope. We will discuss these drift-scan observations in Section 2. In Section 3 we describe the follow-up observations and timing analysis. In Section 4 we describe the properties of the thirteen pulsars and in Section 5 we describe interesting individual pulsars. Finally in Section 6 we present the conclusions and the future survey planned in light of the results obtained in this survey. The survey sensitivity, pipeline, and the remaining new pulsars will be discussed in Lynch et al.

¹The Robert C. Byrd Green Bank Telescope (GBT) is operated by the National Radio Astronomy Observatory which is a facility of the U.S. National Science Foundation operated under cooperative agreement by Associated Universities, Inc.

(2012 ,hereafter Paper II).

2.2 Survey Observations

The drift-scan observations occurred from May through August in the northern hemisphere's summer of 2007. The telescope was parked at a set azimuth during the track refurbishing and data were recorded while the sky drifted through the telescope's beam. The elevation of the telescope had a limit of 60° during the weekdays and 30° during the weekends. The azimuth was set at $\sim 229^\circ$ for the first half of the observations and $\sim 192^\circ$ for the second half of the observations. These azimuth restrictions allowed us to access declination ranges of $-7.72^\circ < \delta < 38.43^\circ$ and $-20.66^\circ < \delta < 38.43^\circ$ for azimuths of 229° and 192° , respectively. All right ascensions were available for us to observe.

We chose a frequency of 350 MHz for this survey for many reasons. Firstly, at 350 MHz, the radio frequency interference (RFI) environment at the GBT is remarkably manageable. Pulsars generally have very steep spectral indexes (Sieber 1973) making 350 MHz an optimal choice for our survey, which mostly covers high Galactic latitudes, where propagation effects in the interstellar medium are generally less severe. Lastly, the GBT's beam size at 350 MHz is $\sim 36'$, allowing us to cover a greater amount of the sky than would be possible with higher frequency receivers. The sky coverage rate (210 deg^2 per day) is faster than that achieved by the Parkes Multi-beam Pulsar Survey (PMPS) at 1.4 GHz (26.25 deg^2 per day; Manchester et al. 2001).

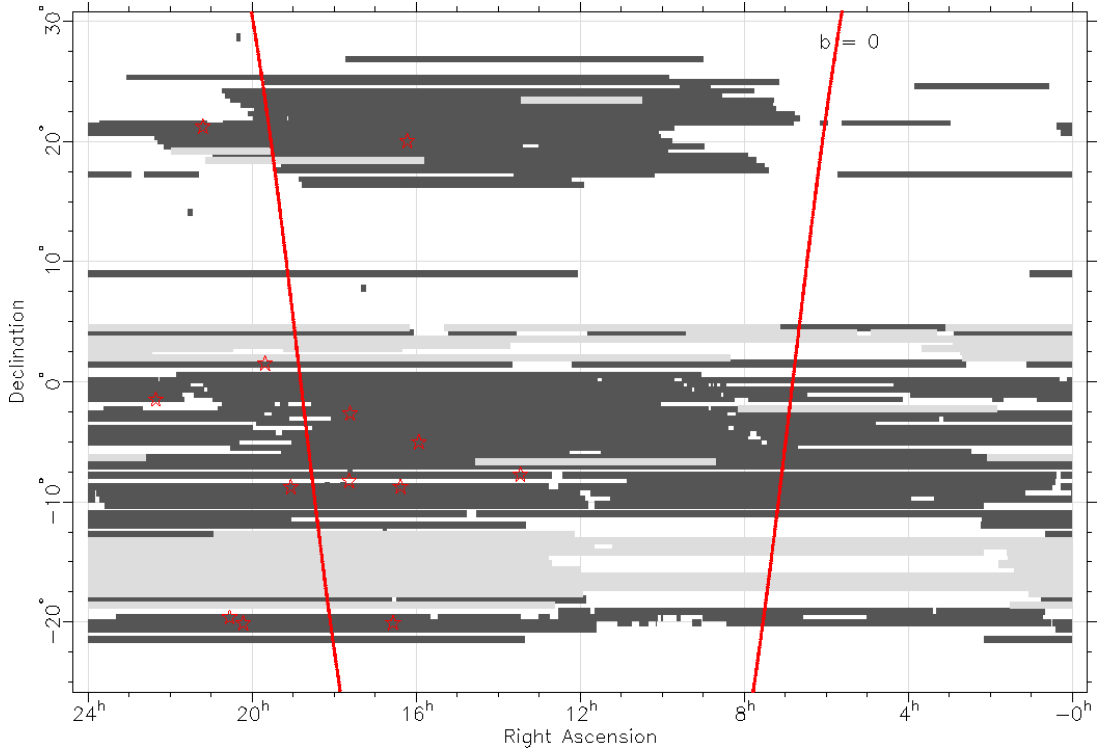


Figure 2.1: A plot in equatorial coordinates showing the sky coverage of the survey. The PSC portion is shown in gray and the red line shows the Galactic plane. New discoveries presented in this paper are shown as red stars.

The now retired Spigot autocorrelation spectrometer (Kaplan et al. 2005) was used for the GBT drift-scan observations. During the data recording we used 50 MHz of bandwidth with 81.92 μ s sampling time. For the first week of observations (MJDs 54222 – 54230) data were recorded with 1024 three-level auto-correlation functions (ACFs) which were digitized to 16-bit samples for analysis. Afterwards, and until the conclusion of the observations, a new 2048 three-level ACF mode was used which was digitized to 8-bit samples.

Data were recorded every night on each weekday and for 24 hours a day during the weekends. During this time, 1491 hours of data were taken, amounting to 134 TB (see Table 2.1 for observation list and Figure 2.1). This amounts to a sky coverage

of 10347 square degrees, of which \sim 2800 went to the Pulsar Search Collaboratory (PSC; Rosen et al. 2010).² A source passing through the center of the beam is visible for roughly 140s. Assuming a detection significance of 8σ and a total system temperature of 80 K results in a survey flux density limit

$$S_{\min} \cong 4.5 \text{ mJy} \sqrt{\frac{\epsilon}{1 - \epsilon}}, \quad (2.1)$$

where $\epsilon = W/P$ is the observed pulse duty cycle for a pulse of width W and period P . For $\epsilon = 0.04$, typical for normal pulsars, this corresponds to a sensitivity limit of roughly 0.9 mJy. Scaling our flux density limit with an average pulsar spectral index of -1.6 (Lorimer et al. 1995) gives us a limit of 0.10 mJy at 1400 MHz, about a factor of two less than the PMPS survey (\sim 0.16 mJy), but our observations are hampered more by dispersion smearing and scattering. A more detailed discussion about the survey sensitivity is presented by Lynch et al. (2012). Data processing was done with the PRESTO³ pulsar package (Ransom 2001).

²The PSC is a collaboration between NRAO and WVU that involves high-school students in searching for pulsars. <http://www.pulsarsearchcollaboratory.com/>

³<http://www.cv.nrao.edu/~sransom/presto/>

Table 2.1: Observations

Start MJD	Time (s)	Azimuth (deg)	Elevation (deg)	bits
54222.171759	24640	229.240	60.0	16
54223.181169	23840	229.380	60.5	16
54224.093518	12320	229.450	61.0	16
54224.554143	4720	229.450	61.0	16
54224.621643	24320	229.450	61.0	16
54224.907592	33280	229.480	35.0	16
54225.301921	20320	229.480	35.0	16
54225.959525	43200	229.480	35.0	16
54226.500116	28800	229.480	35.5	16
54226.837373	37040	229.480	35.5	16
54227.267766	16240	229.480	35.5	16
54227.934375	45040	229.470	71.0	16
54228.963969	42320	229.470	61.9	16
54229.958403	43200	229.470	61.4	16
54230.998090	31360	229.470	73.5	8
54231.516273	9360	229.470	66.5	8
54231.760058	9440	229.470	66.5	8
54231.883657	640	229.470	66.5	8
54231.917535	25120	229.470	66.5	8
54232.210949	24800	229.470	66.5	8
54232.508356	44800	229.480	36.0	8
54233.037835	39760	229.480	36.0	8
54233.519282	44000	229.480	34.5	8
54234.035555	36400	229.480	34.5	8
54234.902870	44720	229.470	67.0	8
54235.423958	2960	229.470	67.0	8
54235.922326	45600	229.470	68.0	8
54236.901933	47840	229.470	67.5	8
54237.919329	46480	229.470	68.5	8
54238.483819	44000	229.470	34.0	8
54239.000810	40960	229.470	34.0	8
54239.478183	43920	229.470	33.5	8
54240.001851	42960	229.470	33.5	8
54240.516273	39920	229.470	33.0	8

Table 2.1: cont.

Start MJD	Time (s)	Azimuth (deg)	Elevation (deg)	bits
54240.982708	41120	229.470	33.0	8
54241.905486	27840	229.468	69.0	8
54242.229594	19760	229.468	69.0	8
54242.954803	43440	229.468	69.5	8
54243.918924	46560	229.468	70.0	8
54244.935972	49680	229.481	32.5	8
54245.613970	11760	229.467	70.5	8
54245.759641	32400	229.481	32.0	8
54246.167789	25200	229.481	32.0	8
54246.470150	47200	229.480	31.5	8
54247.020729	4720	229.480	31.5	8
54247.077268	32960	229.480	31.5	8
54247.466794	42800	229.480	30.5	8
54247.967894	42640	229.481	30.5	8
54248.468171	46480	229.481	31.0	8
54249.015174	38320	229.481	31.0	8
54249.944896	2720	229.468	70.5	8
54250.911273	47280	229.472	62.5	8
54251.916400	46800	229.471	63.0	8
54252.590255	31840	231.674	30.0	8
54252.964919	42640	231.674	30.0	8
54253.463414	44000	231.674	29.5	8
54253.975706	41760	231.674	29.5	8
54254.464803	44000	231.674	29.0	8
54254.980926	41200	231.674	29.0	8
54265.957755	43200	229.463	63.5	8
54266.537500	3360	229.443	36.5	8
54266.671968	24720	229.443	36.5	8
54266.960000	42960	229.443	36.5	8
54267.490463	11520	229.443	37.5	8
54267.658148	960	229.443	37.5	8
54267.759062	13520	229.443	37.5	8
54267.929884	45600	229.443	37.5	8
54268.467071	43200	229.471	38.5	8

Table 2.1: cont.

Start MJD	Time (s)	Azimuth (deg)	Elevation (deg)	bits
54268.968426	42320	229.471	38.5	8
54269.909664	14480	229.463	64.0	8
54270.095347	31440	229.463	64.0	8
54270.937789	45040	229.463	64.5	8
54271.945729	44320	229.463	65.0	8
54272.991632	30560	229.472	37.0	8
54273.370602	720	229.471	37.0	8
54273.384676	4560	229.471	37.0	8
54273.476377	22320	229.470	38.0	8
54273.839005	5460	229.471	38.0	8
54273.926203	46080	229.471	38.0	8
54274.462858	24560	229.470	39.0	8
54274.916898	480	229.470	39.0	8
54274.925775	240	229.470	39.0	8
54274.929537	160	229.470	39.0	8
54274.934016	1920	229.470	39.0	8
54274.959525	42000	229.470	39.0	8
54275.450104	160	229.470	39.5	8
54275.454421	3120	229.470	39.5	8
54275.491967	6640	229.470	39.5	8
54275.575879	33040	229.470	39.5	8
54275.965486	6320	229.471	39.5	8
54276.045961	35680	229.470	39.5	8
54276.933912	45040	229.462	65.5	8
54277.914537	46800	229.462	66.0	8
54278.906203	47520	229.459	71.5	8
54279.926539	45920	229.471	40.0	8
54280.566597	34000	192.468	40.5	8
54280.966203	42320	192.468	40.5	8
54281.466296	12720	192.468	41.0	8
54281.637153	26240	192.468	41.0	8
54281.965694	42480	192.468	41.0	8
54282.464317	640	192.467	41.5	8
54282.518310	38000	192.467	41.5	8

Table 2.1: cont.

Start MJD	Time (s)	Azimuth (deg)	Elevation (deg)	bits
54282.968159	42320	192.468	41.5	8
54283.916424	47040	192.457	72.0	8
54284.899815	48320	192.468	44.0	8
54285.464826	36000	192.467	44.5	8
54285.885255	8000	192.467	44.5	8
54285.987454	40800	192.468	44.5	8
54286.915197	46800	192.461	72.5	8
54287.477118	43200	192.450	42.0	8
54287.986250	41280	192.450	42.0	8
54288.471088	37520	192.450	42.5	8
54289.467257	43200	192.467	43.0	8
54289.977025	41600	192.468	43.0	8
54291.115521	320	192.466	51.5	16
54291.146539	320	192.469	38.3	16
54291.157419	400	192.463	58.8	16
54291.183704	1200	192.469	37.5	16
54292.121817	240	192.469	37.5	16
54292.139722	640	192.467	47.6	16
54292.164282	320	192.470	34.0	16
54292.175278	400	192.468	43.4	16
54292.183299	400	192.468	42.1	16
54292.199479	400	192.468	42.1	16
54293.268194	320	192.448	80.0	16
54293.306574	320	192.467	46.5	16
54293.312894	400	192.470	34.4	16
54293.324572	400	192.461	65.2	16
54293.927188	45920	192.471	30.0	8
54294.465220	28400	192.470	30.5	8
54294.817917	800	192.470	30.5	8
54294.863518	80	192.470	30.5	8
54294.872187	720	192.471	30.5	8
54294.888507	1200	192.471	30.5	8
54294.924201	46240	192.471	30.5	8
54295.470521	15360	192.470	31.0	8

Table 2.1: cont.

Start MJD	Time (s)	Azimuth (deg)	Elevation (deg)	bits
54295.712188	8800	192.470	31.0	8
54295.836157	320	192.471	31.0	8
54295.854398	160	192.471	31.0	8
54295.859109	8720	192.471	31.0	8
54295.969039	960	192.471	31.0	8
54296.000903	7200	192.471	31.0	8
54296.092211	27440	192.471	31.0	8
54296.465394	9440	192.470	31.5	8
54296.578426	960	192.471	31.5	8
54296.589977	28560	192.471	31.5	8
54296.924653	2800	192.471	31.5	8
54297.937616	45040	192.463	60.0	8
54298.918518	30960	192.463	60.0	8
54299.278715	15600	192.463	60.0	8
54299.920439	16560	192.471	32.5	8
54300.119456	29280	192.471	32.5	8
54300.924063	46000	192.469	33.0	8
54301.465451	42320	192.469	33.5	8
54301.958924	43040	192.469	33.5	8
54302.461389	43040	192.468	34.0	8
54302.962083	43040	192.468	34.0	8
54303.463102	43040	192.468	34.5	8
54303.966111	43120	192.468	34.5	8
54304.942164	44640	192.469	32.0	8
54305.912500	47200	192.469	35.0	8
54306.938345	45040	192.469	35.5	8
54307.938993	44880	192.469	36.0	8
54308.494872	40000	192.469	36.5	8
54308.960949	43200	192.469	36.5	8
54309.465902	33760	192.469	37.0	8
54309.886470	6320	192.469	37.0	8
54309.962072	42960	192.469	37.0	8
54310.462013	43040	192.468	37.5	8
54310.971840	42000	192.468	37.5	8

Table 2.1: cont.

Start MJD	Time (s)	Azimuth (deg)	Elevation (deg)	bits
54311.900220	44640	192.468	38.0	8
54312.927303	45920	184.493	30.0	8
54313.921898	46320	184.491	39.5	8
54315.159768	25600	184.491	40.0	8
54315.458194	44000	184.491	40.5	8
54315.976192	41760	184.490	40.5	8
54316.466701	34560	184.486	53.0	8
54316.925914	41040	184.486	53.0	8
54317.705150	22000	184.487	53.5	8
54317.970023	42560	184.487	53.5	8
54319.288796	12800	184.487	54.0	8
54321.007917	10240	170.950	54.0	8
54321.179548	24160	170.950	54.0	8
54321.917928	46480	184.472	54.5	8
54322.459421	46800	184.472	55.0	8
54323.004595	39200	184.472	55.0	8
54323.479722	5360	184.472	55.5	8
54323.560520	23360	184.471	55.5	8
54323.902118	5920	184.472	55.5	8
54324.008414	38880	184.472	55.5	8
54324.464317	39120	184.471	56.0	8
54324.920891	4400	184.471	56.0	8
54325.011007	38560	184.471	56.0	8

Table 2.2: Start MJD, total time, azimuth, elevation, and data number of bits for each observation.

Low DM pc cm ³	DM step size pc cm ³	Number of DMs	Down sample factor
0.0	0.03	3700	2
111.0	0.05	1700	4
196.0	0.10	1900	8
386.0	0.20	1900	16
766.0	0.50	500	32

Table 2.3: Table of parameters for DM searched during data processing. Each de-dispersed time series was processed using 128 subbands.

2.3 Discovery Analysis

These long scans of data then had to be searched for pulsars. Each scan was broken up into 150 second overlapping beams. Each beam overlapped the next beam by about 70 seconds.

The beams were then searched for pulsars. The data were down sampled into multiple files. This was done to increase the search speed at higher dispersion measures (DM). The data were dedispersed at 9700 DM values when processed. Table 2.3 shows the DM values chosen for processing.

The data were downsampled by factors of 2, 4, 8, 16, and 32 to allow for quicker processing in the search code. The data were searched for incidences of RFI using the `rfifind` program from PRESTO. This program compiles a list of the most significant and numerous birdies along with mask which is applied to the raw data before dedispersion. The median and mode of the RFI masked is 0.56% and 0.36% respectively.

The data are dedispersed for the given range of DMs with the RFI mask being applied to the data. This is accomplished by creating 128 subbands and creating

time series files in accordance of the DM plan in Table 2.3 with 100 de-dispersed time series being created at one time.

A single pulse search is done on the de-dispersed time series files and records all events with a signal-to-noise ratio greater ($S/N > 5$). This single pulse search attempts to find pulses by matched-filtering the data with a series of different width boxcar functions. The results are stored until the completion of all DMs.

The time series file are then fast Fourier transformed (FFT) into the frequency domain. Immediately after the FFT, red noise (low frequency, correlated noise) was removed from the data. Also in the frequency domain frequencies that are a common source of RFI are removed from the data. The most common frequency of 60 Hz and its harmonics are masked along with a 1.2 Hz signal and its harmonics were found in the data later in the search.

The frequency domain series are searched for harmonic signals. Each series is harmonically stretched and summed with the most significant results sorted after each summation. After the completion of all harmonics sums, the results are filtered to exclude duplicate candidates which may occur over multiple harmonics.

Two searches of the Fourier domain are conducted. The first is a non-acceleration search from here on will be referred as a low acceleration search. This is designed to target long-period pulsars with narrow pulse profiles. The low acceleration search sums 2, 4, 8, and 16 harmonics and searches after each summation. All candidates are stored until the completion of all DM values.

The second search is an acceleration search. This will be referred to as high acceleration search and is designed to look for short-period pulsars, pulsars with

wide pulse profiles, or pulsars in tight binary orbits. The high acceleration search sums 2, 4, and 8 harmonics and searches after each summation. All candidates are stored separately from the low acceleration candidates until the completion of all DM values.

After the completion of all the searches for each DM, diagnostic plots are created to view the results of the searches. The singlepulse plots are the first to be created. Four DM ranges ($0\text{-}30 \text{ pc cm}^{-3}$, $20\text{-}110 \text{ pc cm}^{-3}$, $100\text{-}310 \text{ pc cm}^{-3}$, $300\text{-}1015 \text{ pc cm}^{-3}$) were chosen to cover all the data with a minimum singlepulse S/N > 5.5 . An example of an output singlepulse diagnostic plot is shown in Figure 2.3.

Sifting is conducted separately for both the low acceleration search and the high acceleration search. In the sifting procedure candidates are removed from the list if the DM is less than 1 or if the candidate was not seen at least two consecutive DM values. Next duplicate entries are removed from the candidate lists. The final step is sort the remaining candidates by their presto sigma value.

The best 20 low acceleration candidates and 10 high acceleration candidates are chosen to produce diagnostic plots for. The parameters for each candidate are used as input with the PRESTO program `prepfold` to create diagnostic plots with the raw data. An example diagnostic plot is shown in Figure 2.3.

After the creation of the diagnostic plots, the associated files for all candidates are compressed and archived to a long-term storage area for human inspection.

Single pulse results for 'GBT350drift_54287_2111+2114'

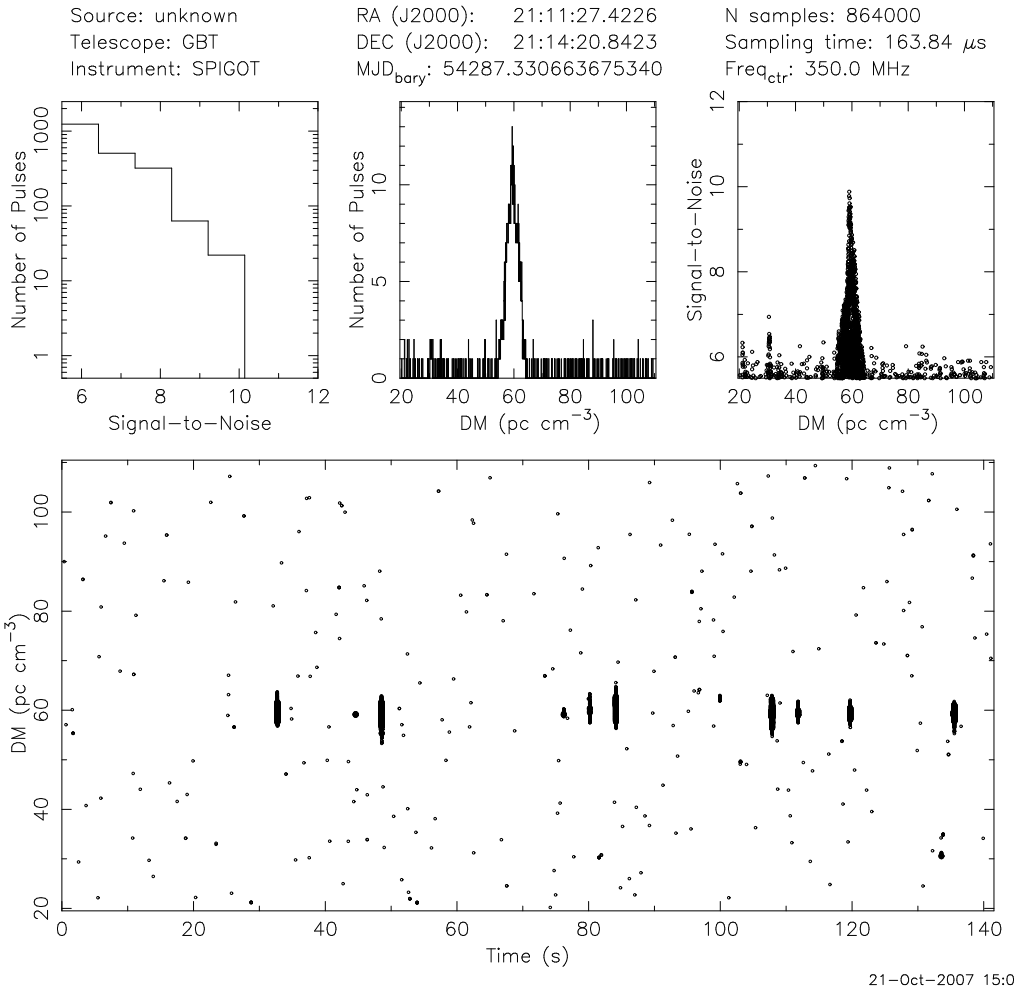


Figure 2.2: Single pulse search output showing the discovery observations of new pulsar J2111+2108.

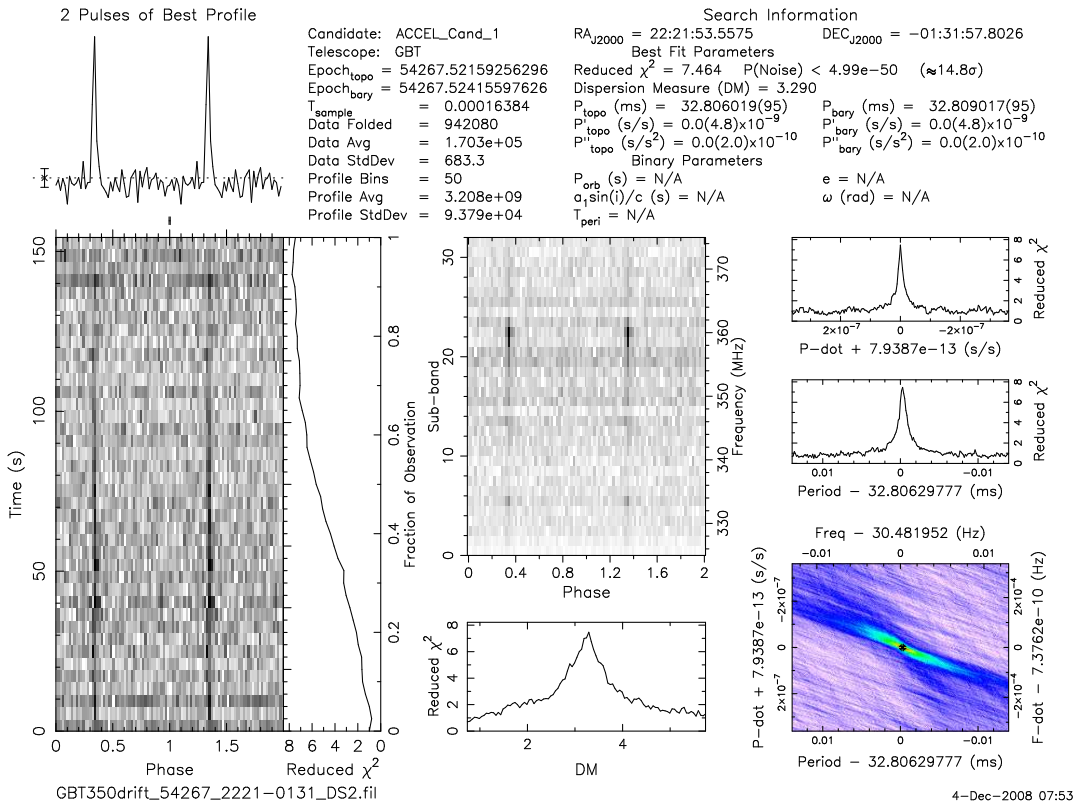


Figure 2.3: Example of the search output diagnostic plot for newly discovered pulsar J2222-0137. Left-hand side shows a pulse profile at the top and a plot of intensity versus time on the bottom. Along the plot of intensity versus time is a plot of χ^2 versus time. The middle top plot show frequency versus pulse phase and the bottom shows χ^2 versus DM. The right hand-side (from top to bottom) shows χ^2 versus period, χ^2 versus \dot{P} , and an intensity plot of period– \dot{P} phase space.

2.4 Timing Observations and Analysis

Timing observations began in the northern Summer of 2008. At that stage, nine new pulsars had been discovered and were observed. The first session was conducted at 350 MHz with the GBT using the Spigot backend with 50 MHz of bandwidth and $81.92 \mu\text{s}$ sampling time. With observations spread across six hours, this session was used to establish a very accurate period and to grid the pulsars.

Gridding is a method of observing a pulsar at multiple locations to determine a more precise position (Morris et al. 2002). A good estimate in Right Ascension (RAJ) can be obtained from the discovery plot by looking for the point of inflection of the χ^2 versus time graph and finding the corresponding RAJ or looking for the maximum intensity in the plot of phase versus observation time (see Figure 2.3 for example). The χ^2 value is a measure of the profile's significance. Each pulsar was observed with the best discovery position and four other positions in each of the cardinal directions with the same observation time. Each cardinal position was offset by $15'$ from the discovery position. A folded profile was made from each data set and along with each observation's RAJ and Declination (DecJ) were used for determining the most likely position of the pulsar. The weighted means for RAJ and DecJ were computed using the reduced χ^2 for each profile (see, e.g., Lorimer & Kramer 2005). If a pulsar was undetected in an observation, it was not used in the weighted mean. The positions given from the gridding are then used for the next observation and also as the beginning position for pulsar timing with TEMPO⁴.

⁴<http://www.atnf.csiro.au/research/pulsar/tempo/>

Pulsar PSR	RAJ HH:MM:SS	DecJ DD:MM	ΔP discovery arcmin	ΔP gridding arcmin
J1555–0515	15:55:38(5)	–05:07(1)	12.5	8.5
J1612+2008	16:12:31(8)	+20:05(2)	8.0	3.2
J1735–0243	17:35:55(4)	–02:41(1)	4.1	4.0
J1737–0814	17:37:39(4)	–08:15(1)	4.2	2.0
J1903–0848	19:03:22(5)	–08:49(1)	2.9	2.8
J2012–2029	20:12:52(9)	–20:18(1)	21.0	11.6
J2033–1938	20:33:52(4)	–19:39(1)	1.5	1.2
J2111+2108	21:11:28(5)	+21:08(2)	8.2	2.4

Table 2.4: Post-gridding best-fit positions of pulsars. ΔP is the difference between the true position and the discovery and post-gridding positions.

Table 2.4 shows the pulsars’ best-fit position from gridding and the difference between the pre- and post-gridding positions with respect to the true position (i.e. that from the final timing solution). The results vary, but all pulsars showed an improved position with respect to the final TEMPO position, with pulsars having a larger initial offset showing greater improvement. The improvement in position offers three benefits: (i) a position closer to the true position lessens the time to a timing solution; (ii) it moves the pulsar closer to the center of the beam of the telescope, improving the S/N and yielding smaller errors on the times of arrivals (TOAs); and (iii) it allows higher frequency observations to occur before a full timing solution is known.

Most of the rest of the timing follow-up observations in the first year (July 2008 – May 2009) were conducted using the Spigot backend at a center frequency of 820 MHz with 1024 channels and $81.92 \mu\text{s}$ sampling time (see Table 2.4 for a complete list of observations). All further observations (June 2009 onwards) were conducted using the newly commissioned Green Bank Ultimate Pulsar Processing

Instrument (GUPPI) backend (Ransom et al. 2009). Most of the observations were taken at a center frequency of 820 MHz with 200 MHz of bandwidth, 2048 channels, and 40.96 μ s sampling time. For pulsars that had satisfactory timing solutions, the data were taken in on-line folding mode with ten-second integrations, while the rest were done in search mode the data being taken in **psrfits** format (Hotan et al. 2004).

Times of arrival (TOAs) for Spigot and GUPPI search mode data are produced using PRESTO. Each data set is first subbanded, or de-dispersed at the pulsar's dispersion measure (DM) into broader frequency channels. We used 16 subbands for long period pulsars and 32 subbands for MSPs. The DM value used for subbanding is either the discovery value or a timing-derived value, if multi-frequency TOAs were available for fitting DM. For on-line folded GUPPI data no subbanding was needed.

Folded pulsar profiles were created from the subbanded data using PRESTO; an example output plot is shown in Figure 2.3. These folds were done using a TEMPO parameter (par) file and profiles were folded using 128 bins for normal period pulsars or 64 bins for MSPs. On-line folded GUPPI data were scrunched in time and frequency to form a profile using the PSRCHIVE package with 256 pulse phase bins.

TOAs are measured from the folded profiles using PRESTO for all search mode data. The program uses the frequency domain algorithm for this process described by Taylor (1992). The TOAs are produced in the Princeton format, with one TOA being produced per observation for each isolated pulsar and three per observation for each binary pulsar for easier determination of binary parameters. TOAs for the

MJD range (days)	Machine	Center Frequency (MHz)	Bandwidth (MHz)	Channels	Sampling Time (μ s)
54634–54635	Spigot	350	50	1024	81.92
54644–54726	Spigot	820	50	1024	81.92
54741	Spigot	990	50	1024	81.92
54767–54856	Spigot	820	50	1024	81.92
54866	Spigot	1500	800	1024	81.92
54885	Spigot	820	50	1024	81.92
54902–54906	Spigot	1500	800	1024	81.92
54917	Spigot	820	50	1024	81.92
54935	Spigot	1500	800	1024	81.92
54947	Spigot	820	50	1024	81.92
54964	Spigot	2000	800	1024	81.92
54976	Spigot	820	50	1024	81.92
54985	GUPPI	1420	200	2048	61.44
54988–54996	GUPPI	1500	800	2048	61.44
54997	GUPPI	2000	800	2048	40.96
55005–55011	GUPPI	820	200	2048	61.44
55015	GUPPI	2000	800	2048	81.92
55016–55017	GUPPI	820	200	2048	40.96
55023	GUPPI	350	100	2048	122.88
55023–55024	GUPPI	350	100	2048	81.92
55025	GUPPI	350	100	2048	122.88
55026	GUPPI	350	100	2048	81.92
55033–55069	GUPPI	820	200	2048	40.96
55079	GUPPI	350	100	2048	122.88
55093–55095	GUPPI	820	200	2048	40.96
55112	GUPPI	2000	800	2048	40.96
55121–55339	GUPPI	820	200	2048	40.96
55354	GUPPI	1400	800	2048	40.96
55359–55396	GUPPI	820	200	2048	40.96
55406	GUPPI	350	100	2048	81.92
55453–55639	GUPPI	820	200	2048	40.96

Table 2.5: Observational parameters for timing observations.

on-line folded data are created with PSRCHIVE⁵ and also used the Taylor (1992) method with the same numeration as the search mode data. Templates are created by fitting Gaussian functions to the summed pulse profile. From these Gaussian components, noise-free templates are created for each observing frequency.

An ephemeris file is created for each pulsar for use with TEMPO. These files include astrometric, spin, and if applicable binary parameters. The period is taken from the discovery plot for isolated pulsars. Binary pulsar periods change with orbital phase, so their periods require a more complicated process that will be described in the next paragraph along with determining their binary parameters. Position in RAJ and DecJ are obtained from gridding of the initial discovery position. All pulsars were assumed to have a period derivative (\dot{P}) value of zero at the start of timing but later fitted for when the data span was long enough to measure the \dot{P} . The epoch of period (PEPOCH) was initially taken to be the MJD of the first timing observation and can be adjusted as additional observations are added.

Binary pulsars require more input parameters than isolated pulsars. Initial estimates of the binary parameters are made by fitting a sinusoid to data of barycentric period versus time. Parameters acquired from this fit include the pulsar's barycentric period, orbital period, projection of semi-major axis, and the epoch of passage of periastron.

For each pulsar, the TOAs and ephemeris are used in TEMPO to carry out a standard pulse timing analysis. In this iterative process (for details, see, e.g., Lorimer & Kramer 2005), a model is generated which keeps track of each neutron

⁵<http://psrchive.sourceforge.net/current>

star rotation over the entire baseline of the observations. The result is a model for the behavior of the pulsar with a root-mean-square of the difference between the model and the TOAs. The timing parameters for each pulsar are listed in Tables 2.7 through 2.13 with typically root-mean-square of the order of a few milliperiods.

2.5 Other measured parameters

Along with timing parameters, the follow-up observations can provide other information about the pulsar. The following section discusses other measured properties obtained during the course of these observations.

2.5.1 820 MHz Fluxes

Fluxes were measured using the calibration routine associated with PSRCHIVE with the on-line folded GUPPI data. On and off source scans of the extragalactic radio source 3C190 were used for the flux calibration. Before each observation, a one minute cal-scan was taken with a 25 Hz noise diode at the receiver. RFI was removed from the pulsar and cal-scan data using the `psrzap` utility created by Paul Demorest.

Next, a database is created containing the information for each the on and off flux scans, cal-scan, and pulsar data. Using the file in the database, an absolute flux conversion factor is calculated and applied to the pulsar data. Afterwards a rotation measure fit is always applied to the data, (this procedure will be described in section 2.5.2). Lastly, a flux measurement of total intensity is taken from the

calibrated data.

2.5.2 Rotation Measures

For pulsars with enough linearly polarized flux, rotation measure (RM) values were calculated. This includes 10 of the 13 pulsars in this sample. PSRCHIVE was used with on-line folded GUPPI data for producing the RMs. The method used here is similar to that presented in recent work of Yan et al. (2011).

After the data were calibrated for polarization, we test many different RM values from $-1000 - 1000$ to find the one which provides the most polarized flux. An example plot showing this procedure for PSR J1941+0121 can be seen in Figure 2.4. A Gaussian is fit to the data of polarized flux versus RM and the mid-point of the Gaussian is taken as the best RM value. A RM correction is applied to the calibrated data before a flux is calculated (as mentioned in section 2.5.1). The RM values quoted for each pulsar are average values over multiple observations with the standard deviation as the error. This is done in case the ionosphere contaminated any RM values (see, e.g., Yan et al. 2011).

2.5.3 Pulse Widths at 820 MHz

Pulse widths at 50% intensity, W_{50} , are derived using either a Gaussian for single peak profiles or by measuring the width across the outer edge of the profile at 50% of the peak flux for multiple component profiles. This is done for each epoch. The W_{50} values for each epoch were averaged and the standard deviation was taken

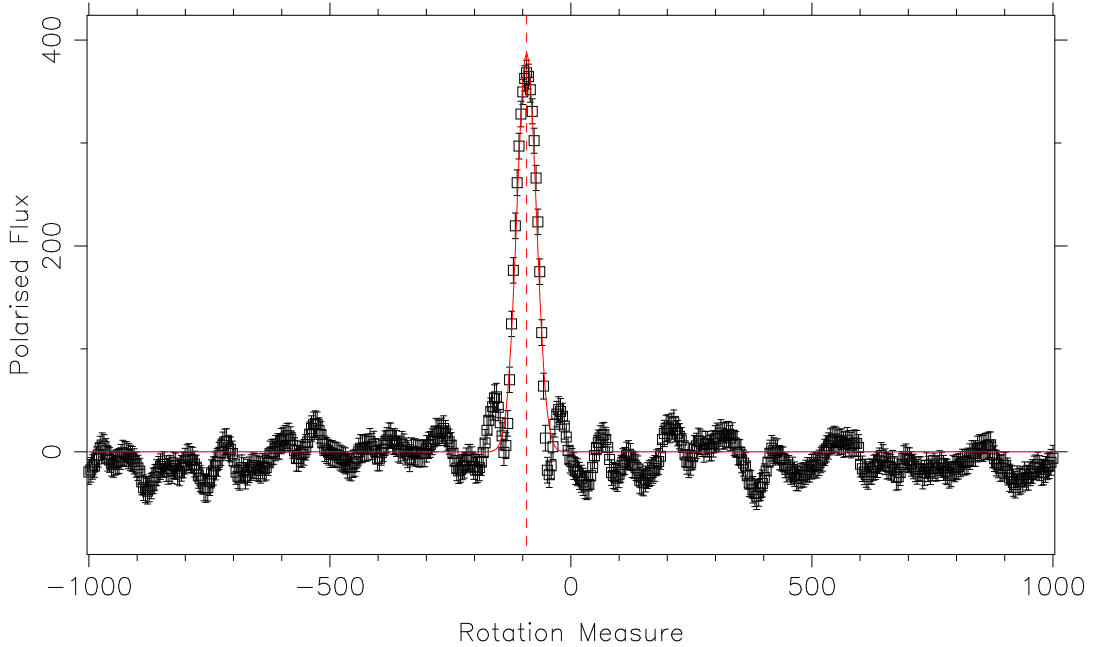


Figure 2.4: Example fit for RM for PSR J1941+0121.

as the error.

2.6 Discussion

Results from pulsar timing and the analysis mentioned in section 2.5 are located in Tables 2.7 through 2.13 for each individual pulsar and a plot showing the location of each new pulsar on the $P - \dot{P}$ diagram is shown in Figure 2.5. All properties are quoted with 1σ errors and the DM-derived distances are from the NE2001 electron model (Cordes & Lazio 2002). The distances have errors $\sim 20\%$. The equations for calculating surface magnetic field strength, characteristic age, and spin-down luminosity are taken for the Handbook of Pulsar Astronomy (Lorimer & Kramer 2005). In the following sections properties of individual pulsars that may have additional applications beyond the scope of this work will be discussed.

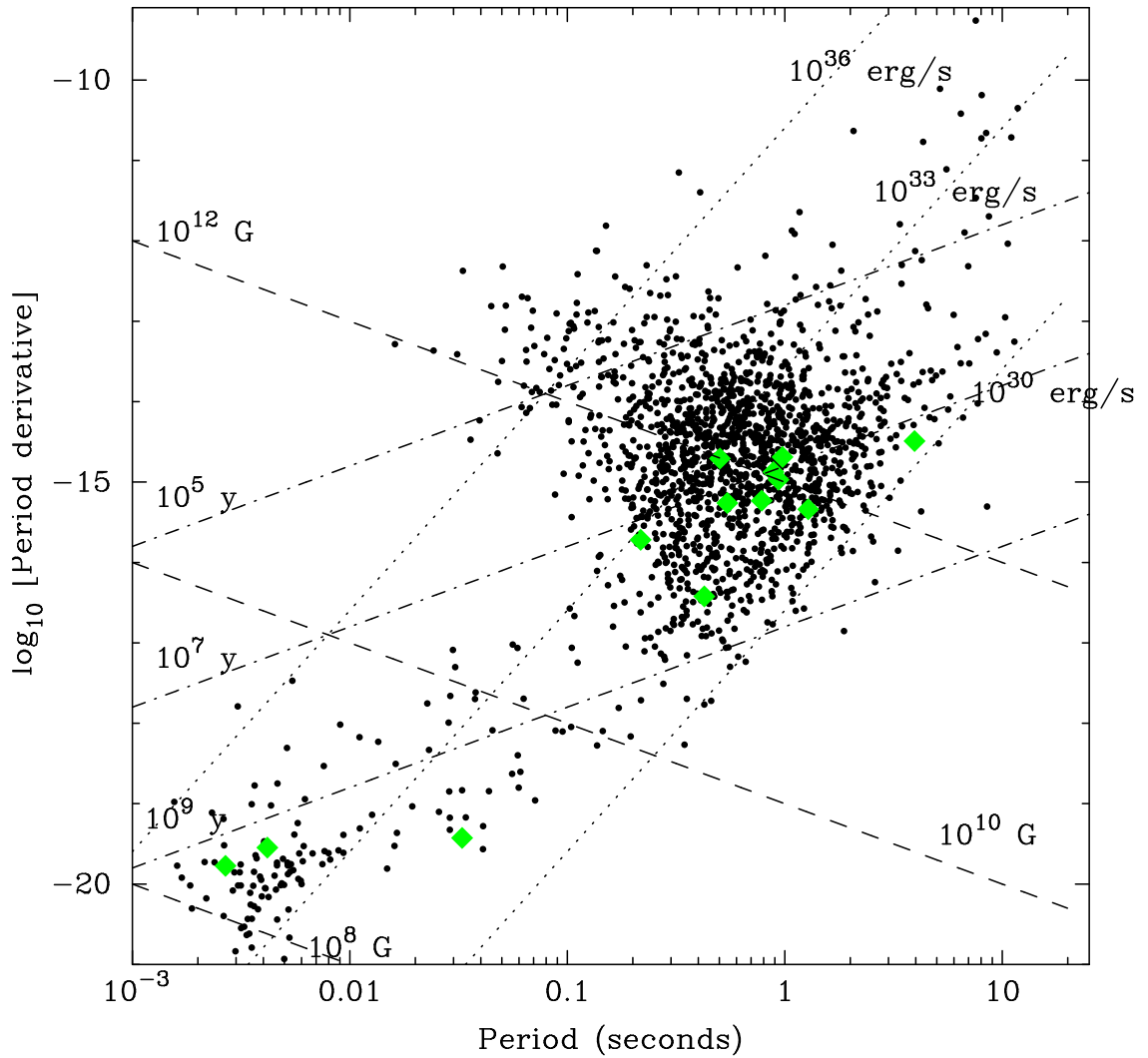


Figure 2.5: $P - \dot{P}$ diagram showing the new discoveries as green diamonds. The lines on the plot show constant spin-down luminosity (dots), constant magnetic field (dash), and constant characteristic age (dot-dash). The pulsar population is taken for the ATNF pulsar catalog (Manchester et al. 2005).

2.6.1 PSR J1327–0755

At the time of discovery, the narrow 350-MHz pulse width of 0.25 ms and location well off the Galactic plane ($b = 54.3^\circ$) of PSR J1327–0755 were encouraging signs that this pulsar may be a good addition to pulsar timing arrays (PTAs) for the search for gravitational waves (Foster & Backer 1990). However, analysis at 820 MHz indicates that PSR J1327–0755 may not meet the standards needed for a PTA pulsar due to variations in its flux from interstellar scintillation. Only \sim 35% of Spigot observations and \sim 95% of GUPPI observations resulted in a detection, with the pulsar detectable in only $\sim 25\%$ of the bandpass for GUPPI observations. The large difference in S/N between 350 and 820 MHz implies that PSR J1327–0755 has a steep spectral index but scintillation has hindered any attempt to reliably measure this. With an orbital period of 8.44 days and a projected semi-major axis of 6.65 lt-s, PSR J1327–0755 has a minimum companion mass of $0.22 M_\odot$ and with its location on the $P - \dot{P}$ diagram, its companion is most likely a white dwarf.

2.6.2 PSR J1623–0841

PSR J1623–0841 was discovered in only the single pulse search and was labeled a rotating radio transient (RRAT; McLaughlin et al. 2006). Later observations at 350 MHz with Spigot showed single pulses but no detections were made at 820 MHz. Gridding observations were unable to localize the position better than the discovery position because of its transient nature. The final TEMPO position was 20' away from the discovery position (outside the GBT's 820-MHz beam) and a

timing solution was only attainable with the increased sensitivity of GUPPI and a dense set of observations at 350 MHz. A full discussion of PSR J1623–0841 will be presented in Chapter 3.

2.6.3 PSR J1737–0814

PSR J1737–0814 is a binary pulsar in an eccentric orbit ($e = 0.013$) with an orbital period of 79.38 days and a minimum mass companion of $0.06 M_{\odot}$. Phinney (1992) predicts a relationship between orbital period and eccentricity of

$$\langle e^2 \rangle^{0.5} = 1.5 \times 10^{-4} (P_b / 100 \text{ days}) \text{ for } P_b > P_{\text{crit}} \approx 25 \text{ days}, \quad (2.2)$$

The eccentricity of PSR J1737–0814 is about two orders of magnitude greater than what is predicted by this relationship and is the second largest eccentricity for a Galactic plane MSP. This large deviation is possible though unusual for Galactic field MSPs; PSR J1903+0327 is a binary pulsar with a orbital period of 95.17 days and an eccentricity of 0.437, which has been suggested to have evolved from a triple system (Freire et al. 2011).

If we assume that the companion of PSR J1737–0814 is a white dwarf, which is very common for pulsars located in that area of the $P - \dot{P}$ diagram, and the minimum mass of the white dwarf is $0.6 M_{\odot}$, then we can obtain a maximum inclination angle of 8 degrees assuming a pulsar mass of $1.35 M_{\odot}$. With the wide pulse width (see Figure 2.9) and low inclination angle, a measure of the companion’s mass through the Shapiro delay (Shapiro 1964) would be impossible. Other Post-Keplerian parameters

such as the relativistic advance of periastron are also unattainable due to the low precision of the TOAs provided by this pulsar.

2.6.4 PSR J1941+0121

PSR J1941+0121 has the shortest period (217 ms) of the non-recycled pulsars found in this survey and about 85% of its total flux is linearly polarized. This high percentage of linearly polarized flux along with its relatively wide pulse width ($\epsilon = 0.093$) has allowed us to produce a model of the pulsar's emission using the PSRCHIVE software package. A complex-value Rotating Vector Model (RVM; Radhakrishnan & Cooke 1969) was fit to the Stokes Q and Stokes U profiles, treating them as real and imaginary numbers instead of the single parameter value of position angle. Figure 2.6 shows the fit of the model and Table 5 gives the model fit parameters. The model gives an impact parameter ($\beta = \zeta - \alpha$) of 11° and an inclination angle of 116° . Due to the large error of the impact parameter (13°), we are unable to determine if we see an inner or outer line of sight. The model has a χ^2 of 37.8 with 37 degrees of freedom (on-pulse phase bins), giving a reduced χ^2 of 1.02.

2.6.5 PSR J2222–0137

PSR J2222–0137 is in a low eccentricity orbit ($e = 0.00038$) with an orbital period of 2.4 days and a projected semi-major axis of 10.8 lt-s. The orbital parameters lead to a mass function of $0.229 M_\odot$. Assuming a pulsar mass of $1.35 M_\odot$

Parameter	Angle (degrees)	Error (degrees)
ψ_0	-82	2
ζ	127	9
α	116	10
ϕ_0	172.3	0.5

Table 2.6: RVM model fit results for PSR J1941+0121. Here ϕ_0 is the pulse phase of magnetic meridian, ψ_0 is position angle at ϕ_0 , α is the colatitude of magnetic axis, and ζ is the colatitude of the observer's line of sight.

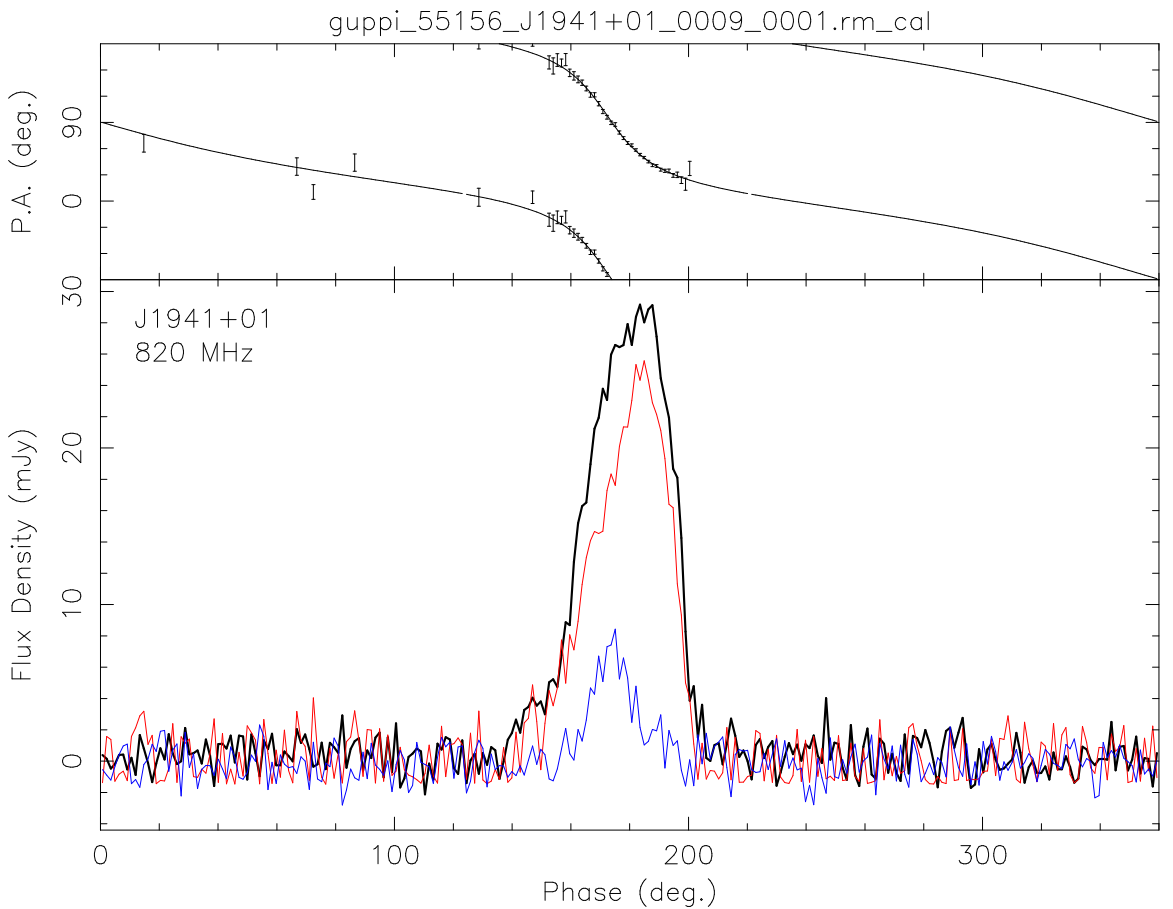


Figure 2.6: RVM model fit for the radio emission of PSR J1941+0121. The top plot shows parallactic angle versus pulse phase, while the bottom plot shows integrated pulse flux density versus pulse phase for total intensity (black line), linearly polarized flux (red line), and circularly polarized flux (blue line).

this gives us a minimum companion mass of $1.11 M_{\odot}$. The spin period of 33 ms, the binary parameters, and the lack of a significant \dot{P} indicate this pulsar is a partially recycled pulsar. Based on these parameters, and from what is known about other binary pulsars, the companion star is most likely a member of the so-called “intermediate-mass binary pulsars” (e.g. Camilo et al. 2001) in which the companion star is a CO white dwarf. It is also possible, though less likely given the low orbital eccentricity, that PSR J2222–0137 is a member of a double neutron star binary system. Many follow-up observations of PSR J2222–0137 at multiple frequencies have been searched for a second pulsar without success with a S_{max} of $11 \mu\text{Jy}$ at 1400 MHz.

A minimum companion mass of $1.11 M_{\odot}$ and timing residuals of $\sim 16 \mu\text{s}$ for PSR J2222–0137 suggest that the companion mass and orbital inclination could be measured due to Shapiro delay as the pulsar’s emission passes through the gravitational potential of the companion. In order to investigate the feasibility of observing this effect, simulations have been done using TEMPO2⁶ for different scenarios that will satisfy the mass function and are shown in Figure 2.7. These simulations assumed a TOA error of $3.5 \mu\text{s}$ and two-minute integration times. The observations were placed at each extrema in the Shapiro delay higher harmonics, with a six-hour observation at superior conjunction and two-hour observations at each other extrema. This simulated observing strategy provides detection limits only 20% less significant than observing a whole orbit with the same TOA cadence, using only one-fifth of the time.

⁶www.atnf.csiro.au/research/pulsar/tempo2/

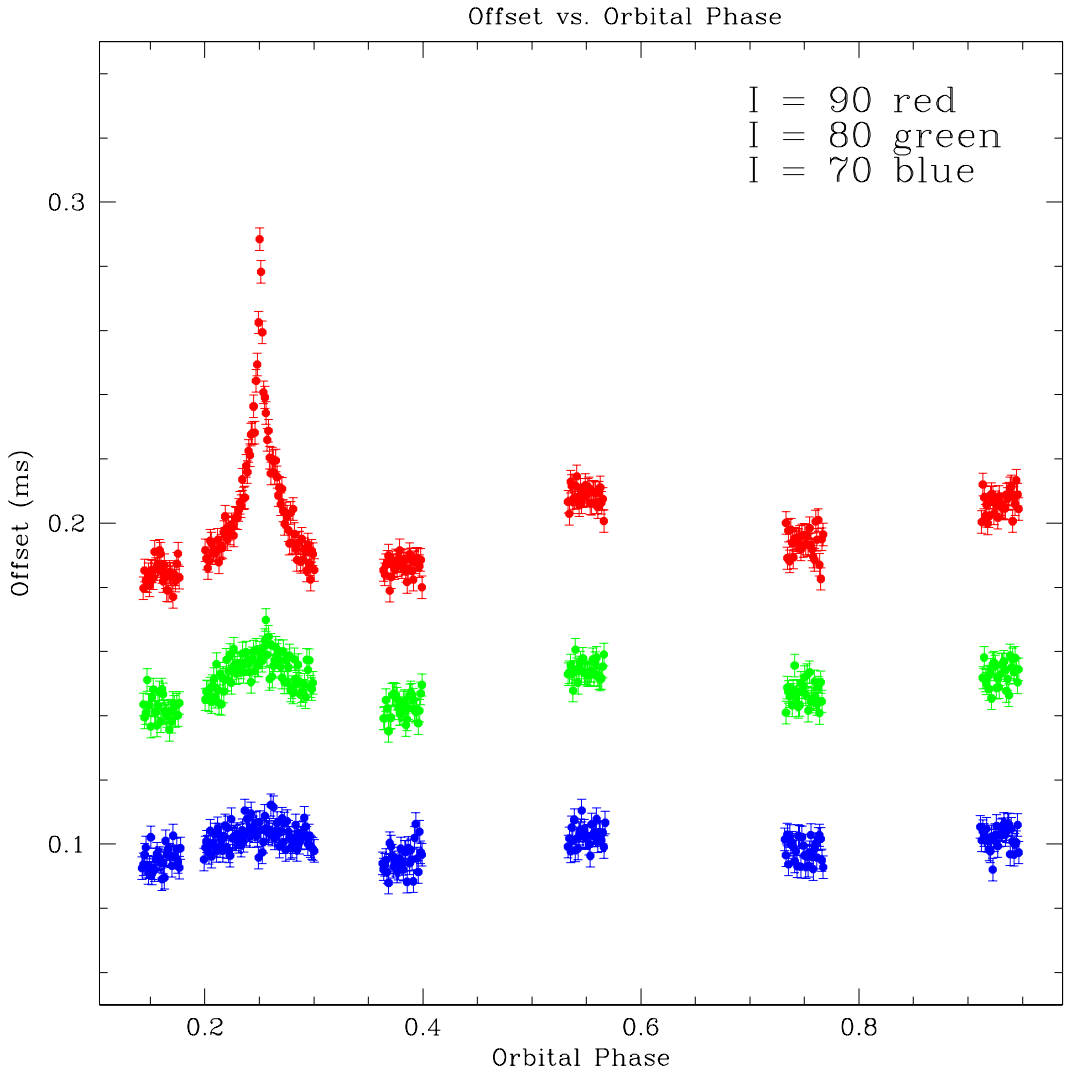


Figure 2.7: TEMPO2 simulations showing the Shapiro delay expected for PSR J2222–0137 for multiple inclination angles. The x-axis is the orbital phase of the pulsar with respect to periastron and the y-axis is the excess time delay caused by the companion as the pulsar’s signal passes through the warped space-time around the companion. From top to bottom: $i = 90^\circ$ (red), $i = 80^\circ$, (green), and $i = 70^\circ$ (blue).

Using the DM value of 3.28 pc cm^{-3} , the NE2001 electron density model predicts a distance of ~ 300 pc to PSR J2222–0137 (Cordes & Lazio 2002). Assuming this distance estimate is reliable it implies J2222–0137 is the second closest binary pulsar system after J0437–4715 at a DM of 2.64 pc cm^{-3} and a distance of 156 pc (Deller et al. 2009). For pulsars located this close to us, a large window of multi-wavelength observations opens up. These include VLBA observations to measure proper motion and parallax, optical observations to search for an optical companion, X-ray observations to look for blackbody emission from the neutron star, and gamma-ray observations to look at higher magnetosphere emission. All the observations proposed in this paragraph and the Shapiro delay observations have occurred, except the last epochs of the VLBA observations, and the results will be reported in future publications.

2.7 Conclusions and Future Work

The 350-MHz drift-scan provided many new interesting pulsars to study across the whole electromagnetic spectrum. Along with PSR J2222–0137 featured in this work, J1023+0038 (Archibald et al. 2009), J2256–1023 (Stairs et al. in prep), and J0348+0438 (Lynch et al. in prep) have all had multi-messenger studies conducted with them. This survey was the primer for a new survey called the Green Bank North Celestial Cap (GBNCC) survey. In this survey we are taking advantage of the newest pulsar instrument on the GBT, the GUPPI backend. This survey is conducted with real 8 bit sampling, 4096 frequency channels, 100 MHz of bandwidth,

120 second integration times, and $81.92 \mu\text{s}$ sampling time at a center frequency of 350 MHz. This survey will be about a factor of two more sensitive than the survey described in this paper and will be a powerful probe of the millisecond pulsar population in the northern sky. The GBNCC survey will cover the whole entire northern sky visible by the GBT.

Acknowledgments

MAM and DRL are supported by WVEPSCOR, the NSF PIRE Program, and the Research Corporation for Scientific Advancement. JRB acknowledges support from WVEPSCoR, the National Radio Astronomy Observatory, the National Science Foundation (AST 0907967), and the Smithsonian Astrophysical Observatory (Chandra Proposal 12400736).

Parameter	PSR J1555–0515	PSR J1612+2008
Timing Parameters		
Right Ascension (J2000)	15:55:40.102(8)	16:12:23.429(3)
Declination (J2000)	−05:15:56.8(3)	20:08:18.37(5)
Spin Period (s)	0.975409891127(7)	0.4266459810255(16)
Period Derivative (s s^{-1})	$2.0519(8) \times 10^{-15}$	$3.758(17) \times 10^{-17}$
Dispersion Measure (pc cm^{-3})	23.489(14)	19.539(6)
Reference Epoch (MJD)	54985	54985
Span of Timing Data	54635–55335	54635–55302
Number of TOAs	36	40
RMS Residual (μs)	640	350
Derived Parameters		
Galactic Longitude (degrees)	3.97	35.52
Galactic Latitude (degrees)	34.97	43.74
Distance (kpc)	1.2	1.3
Distance Off Plane (kpc)	0.69	0.90
Surface Magnetic Field (10^{12} Gauss)	1.41	0.126
Spin-down Luminosity (10^{31} ergs s^{-1})	2.75	0.603
Characteristic Age (Myr)	7.41	178
820 MHz Flux Density (mJy)	1.2(2)	0.83(11)
W_{50} 820 MHz (ms)	12.9(3)	3.29(10)
Rotation Measure (rad m^{-2})	1.3(3.0)	22(3)

Table 2.7: Timing and derived parameters for newly discovered pulsars.

Parameter	PSR J1623–0841	PSR J1633–2009
Timing Parameters		
Right Ascension (J2000)	16:23:42.711(9)	16:33:55.34(6)
Declination (J2000)	−08:41:36.3(5)	−20:09:59(5)
Spin Period (s)	0.503014992514(6)	0.935557045033(17)
Period Derivative (s s ^{−1})	1.958(3)×10 ^{−15}	1.0680(18)×10 ^{−15}
Dispersion Measure (pc cm ^{−3})	60.433(16)	48.20(6)
Reference Epoch (MJD)	55048	54993
Span of Timing Data	54635–55522	54651–55335
Number of TOAs	36	29
RMS Residual (μs)	765	1347
Derived Parameters		
Galactic Longitude (degrees)	5.77	357.63
Galactic Latitude (degrees)	27.37	18.33
Distance (kpc)	3.3	1.6
Distance Off Plane (kpc)	1.5	0.5
Surface Magnetic Field (10 ¹² Gauss)	1.00	1.00
Spin-down Luminosity (10 ³¹ ergs s ^{−1})	19.5	1.62
Characteristic Age (Myr)	4.07	13.8
820 MHz Flux Density (mJy)	42(13)	1.35(4)
W ₅₀ 820 MHz (ms)	11.2(3)	32.2(1.0)
Rotation Measure (rad m ^{−2})	N/A	−0.1(1.2)

Table 2.8: Timing and derived parameters for newly discovered pulsars.

Parameter	PSR J1735–0243	PSR J1903–0848
Timing Parameters		
Right Ascension (J2000)	17:35:48.31(9)	19:03:11.264(9)
Declination (J2000)	−02:43:51(3)	−08:48:56.8(4)
Spin Period (s)	0.782886976234(10)	0.887324640598(8)
Period Derivative (s s ^{−1})	5.86(6)×10 ^{−16}	1.3302(9)×10 ^{−15}
Dispersion Measure (pc cm ^{−3})	55.3(2)	66.987(15)
Reference Epoch (MJD)	54827	54987
Span of Timing Data	54352–55302	54634–55339
Number of TOAs	39	51
RMS Residual (μ s)	10585	930
Derived Parameters		
Galactic Longitude (degrees)	21.56	26.38
Galactic Latitude (degrees)	15.45	−6.60
Distance (kpc)	1.9	2.0
Distance Off Plane (kpc)	0.51	0.23
Surface Magnetic Field (10 ¹² Gauss)	0.676	1.10
Spin-down Luminosity (10 ³¹ ergs s ^{−1})	1.51	2.34
Characteristic Age (Myr)	20.9	10.5
820 MHz Flux Density (mJy)	1.3(3)	1.4(2)
W ₅₀ 820 MHz (ms)	102(2)	12.3(2)
Rotation Measure (rad m ^{−2})	28.3(1.9)	4.4(9)

Table 2.9: Timing and derived parameters for newly discovered pulsars.

Parameter	PSR J1941+0121	PSR J2012–2029
Timing Parameters		
Right Ascension (J2000)	19:41:16.042(6)	20:12:46.8(2)
Declination (J2000)	01:21:39.5(2)	−20:29:42(14)
Spin Period (s)	0.217317451824(7)	0.544001870607(8)
Period Derivative (s s^{-1})	$1.913(2) \times 10^{-16}$	$5.477(8) \times 10^{-16}$
Dispersion Measure (pc cm^{-3})	52.3(6)	37.42(8)
Reference Epoch (MJD)	55026	54987
Span of Timing Data	54712–55339	54635–55339
Number of TOAs	33	33
RMS Residual (μs)	673	1090
Derived Parameters		
Galactic Longitude (degrees)	39.91	22.41
Galactic Latitude (degrees)	−10.43	−26.70
Distance (kpc)	2.2	1.4
Distance Off Plane (kpc)	0.40	0.63
Surface Magnetic Field (10^{12} Gauss)	0.204	0.550
Spin-down Luminosity (10^{31} ergs s^{-1})	22.9	4.27
Characteristic Age (Myr)	17.8	15.5
820 MHz Flux Density (mJy)	1.7(5)	1.00(12)
W_{50} 820 MHz (ms)	20.2(1.1)	24.2(7)
Rotation Measure (rad m^{-2})	−92.0(3)	N/A

Table 2.10: Timing and derived parameters for newly discovered pulsars.

Parameter	PSR J2033–1938	PSR J2111+2106
Timing Parameters		
Right Ascension (J2000)	20:33:54.8(2)	21:11:33.12(3)
Declination (J2000)	−19:38:27(12)	21:06:07.0(7)
Spin Period (s)	1.28171902368(2)	3.95385295935(13)
Period Derivative (s s ^{−1})	4.58(2)×10 ^{−16}	3.231(13)×10 ^{−15}
Dispersion Measure (pc cm ^{−3})	23.47(3)	59.77(6)
Reference Epoch (MJD)	54987	54987
Span of Timing Data	54635–55339	54635–55339
Number of TOAs	37	35
RMS Residual (μ s)	1533	2686
Derived Parameters		
Galactic Longitude (degrees)	25.32	69.40
Galactic Latitude (degrees)	−31.04	−18.20
Distance (kpc)	1.00	3.8
Distance Off Plane (kpc)	0.51	1.2
Surface Magnetic Field (10 ¹² Gauss)	0.759	3.55
Spin-down Luminosity (10 ³¹ ergs s ^{−1})	0.269	0.0646
Characteristic Age (Myr)	43.6	19.1
820 MHz Flux Density (mJy)	1.13(15)	1.08(10)
W ₅₀ 820 MHz (ms)	32.4(3)	45(2)
Rotation Measure (rad m ^{−2})	−17.7(5)	−75.3(8)

Table 2.11: Timing and derived parameters for newly discovered pulsars.

Parameter	PSR J1327–0755	PSR J1737–0814
Timing Parameters		
Right Ascension (J2000)	13:27:57.984(10)	17:37:33.31(9)
Declination (J2000)	−07:55:16.0(4)	−08:14:08.42(15)
Spin Period (s)	0.002677923197570(2)	0.00417501702755(13)
Period Derivative (s s ^{−1})	$1.02(3) \times 10^{-20}$	$4.34(17) \times 10^{-20}$
Dispersion Measure (pc cm ^{−3})	27.9153(9)	55.349(8)
Reference Epoch (MJD)	55112	55007
Span of Timing Data	54651–55575	54651–55575
Number of TOAs ^a	147	150
RMS Residual (μ s)	38	81
Binary Parameters		
Binary Model	ELL1	BT
Orbital Period (days)	8.43908560(12)	79.37793(2)
Projected Semi-major Axis (lt-s)	6.645761(9)	9.456345(15)
Epoch Of Periastron (MJD)	54725.46(8)	54629.950(4)
Orbital Eccentricity	$2.1(2) \times 10^{-5}$	$1.2249(4) \times 10^{-2}$
Longitude of Periastron (degrees)	14.383(9)	106.102(17)
Mass Function (M_{\odot})	0.004425132(16)	0.0001440961(7)
Minimum Companion Mass ^b (M_{\odot})	0.2219572(8)	0.0661123(4)
Derived Parameters		
Galactic Longitude (degrees)	318.39	16.86
Galactic Latitude (degrees)	53.85	12.34
Distance (kpc)	1.7	1.7
Distance Off Plane (kpc)	1.4	0.36
Surface Magnetic Field (10^{12} Gauss)	1.66×10^{-4}	1.27×10^{-4}
Spin-down Luminosity (10^{31} ergs s ^{−1})	676	741
Characteristic Age (Myr)	4169	1513
820 MHz Flux Density (mJy)	0.9(2)	2.7(2)
W ₅₀ 820 MHz (ms)	0.131(5)	0.52(6)
Rotation Measure (rad m ^{−2})	N/A	71.4(1.4)

^a Three TOAs produced per observation.

^b Assumes a pulsar mass of $1.35 M_{\odot}$.

Table 2.12: Timing and derived parameters for newly discovered pulsars.

Parameter	PSR J2222–0137
Timing Parameters	
Right Ascension (J2000)	22:22:05.9637(7)
Declination (J2000)	−01:37:15.73(3)
RA Proper Motion (mas yr^{-1})	43(3)
DEC Proper Motion (mas yr^{-1})	< 9
Spin Period (s)	0.032817859051169(6)
Period Derivative (s s^{-1})	$5.82(2) \times 10^{-20}$
Dispersion Measure (pc cm^{-3})	3.27765(15)
Reference Epoch (MJD)	55369
Span of Timing Data	55005–55639
Number of TOAs ^a	169
RMS Residual (μs)	16
Binary Parameters	
Binary Model	ELL1
Orbital Period (days)	2.4457599952(2)
Projected Semi-major Axis (lt-s)	10.8480199(14)
Epoch Of Periastron (MJD)	54979.05568(11)
Orbital Eccentricity	$3.8169(13) \times 10^{-4}$
Longitude of Periastron (degrees)	119.834(17)
Mass Function (M_\odot)	0.22914294(9)
Minimum Companion Mass ^b (M_\odot)	1.1173504(5)
Derived Parameters	
Galactic Longitude (degrees)	62.02
Galactic Latitude (degrees)	−46.08
Distance (kpc)	0.31
Distance Off Plane (kpc)	0.22
Transverse Velocity (km s^{-1})	< 66
Shklovski Effect (s s^{-1})	$< 5.02 \times 10^{-20}$
Intrinsic Spin-down (s s^{-1})	$> 8.1 \times 10^{-21}$
Surface Magnetic Field ^c (10^{12} Gauss)	0.00141
Spin-down Luminosity ^c (10^{31} ergs s^{-1})	2.09
Characteristic Age ^c (Myr)	8710
820 MHz Flux Density (mJy)	2.6(5)
W_{50} 820 MHz (ms)	0.570(5)
Rotation Measure (rad m^{-2})	1.8(6)

^a Three TOAs produced per observation.

^b Assumes a pulsar mass of $1.35 M_\odot$.

^c Values are not corrected for Shklovskii effect (Shklovskii 1970).

Table 2.13: Timing and derived parameters for newly discovered PSR J2222–0137.

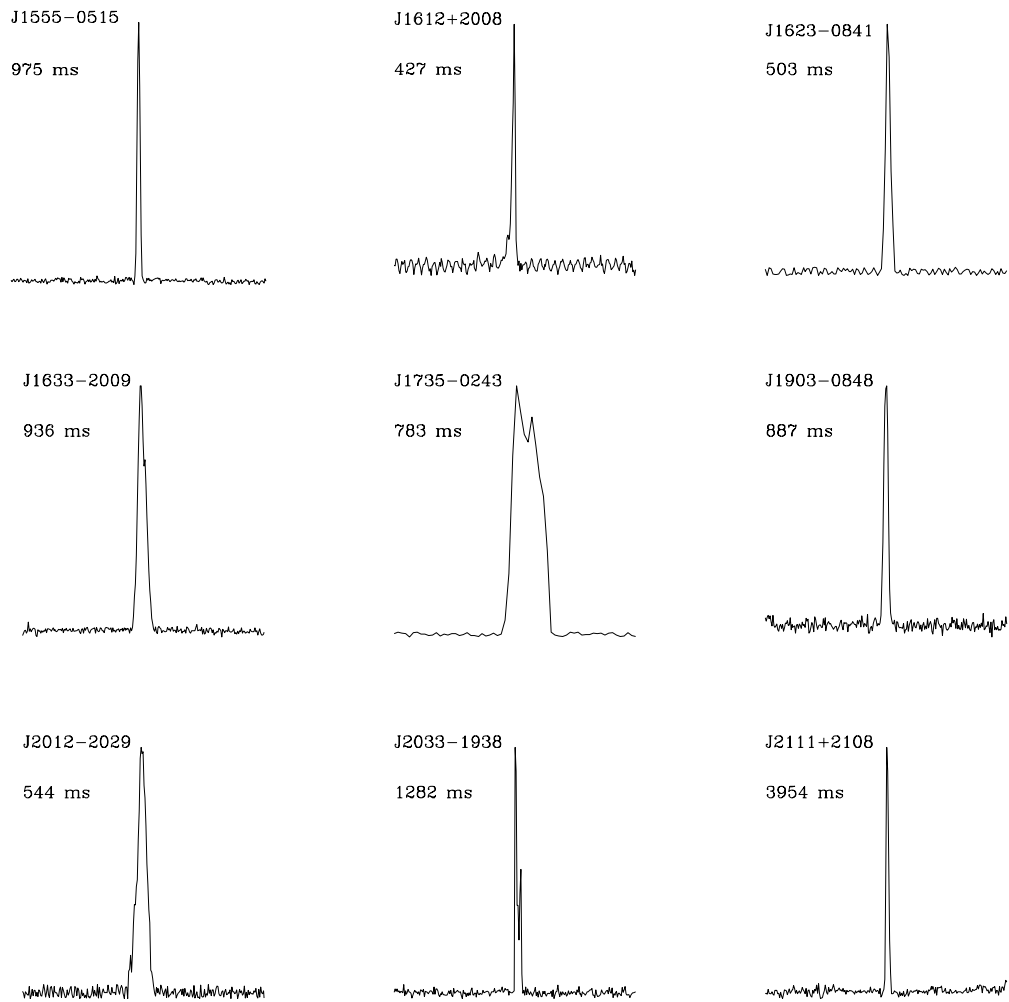


Figure 2.8: Profiles at 820-MHz for nine newly discovered isolated pulsars created from multi-epoch data.

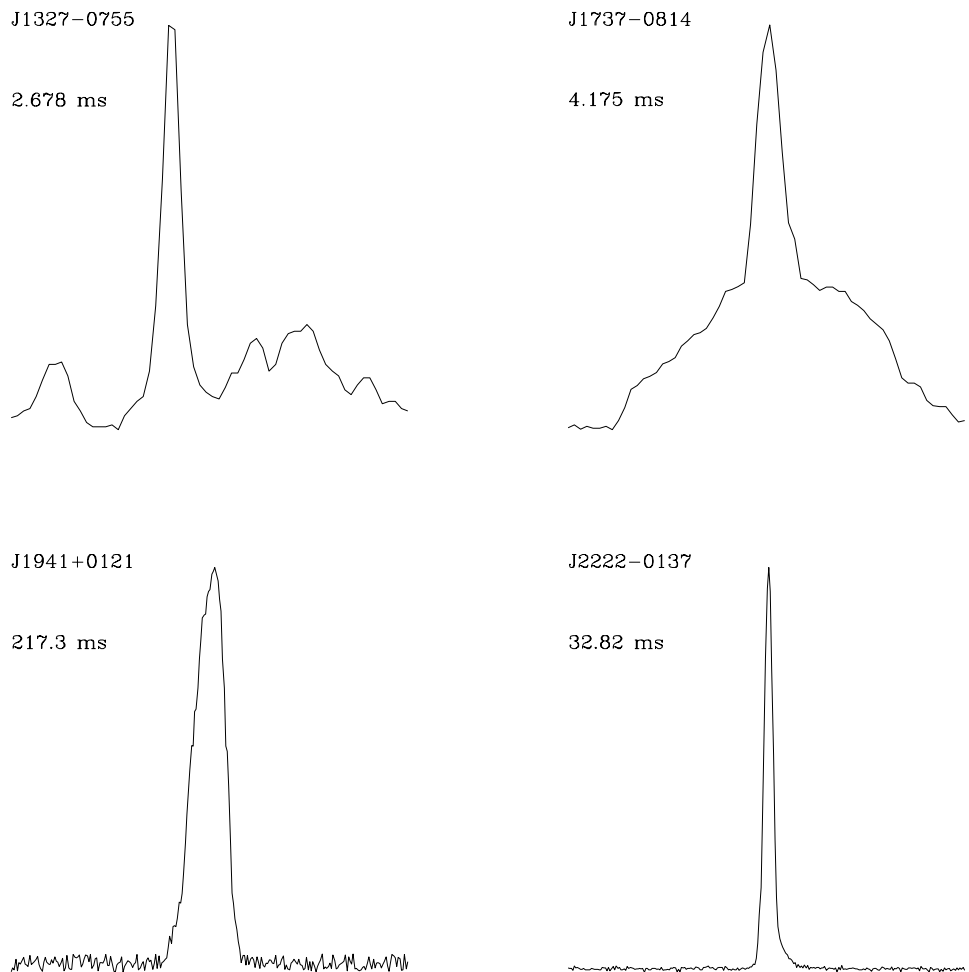


Figure 2.9: Profiles at 820-MHz for four newly discovered pulsars created from multi-epoch data.

Chapter 3

Timing Observation of RRATs

3.1 Introduction

Rotating radio transients (RRATs) are neutron stars that emit radio pulses that are not detectable using frequency domain techniques but are seen in time domain analysis. The first RRATs were discovered in a re-processing of the Parkes Multibeam Pulsar Survey (PMPS) using a single pulse search (see Section 1.4.3 for a description of this process). There were 11 of these presented in McLaughlin et al. (2006). Since then about 56 RRATs in total have been discovered¹ and the single pulse search (described in section 1.4.3) used to detect them has become a part of all standard search pipelines.

When RRATs were initially discovered, their exact nature was not known. As time went on and more observations of them occurred, it became apparent that they were neutron stars with emission properties that deviated from those of normal pulsars because the RRATs could not be detected in a periodicity search like many known pulsars from the past had. Many theories have been put further to explain the RRATs including radio emission being disrupted by fall back of supernova material (Li 2006), trapped plasma being released from radiation belts (Luo & Melrose 2007), and circumstellar material interacting with the pulsar (Cordes & Shannon 2008).

¹<http://www.as.wvu.edu/~pulsar/rratalog/>

RRATs may be just one part of the neutron star spectrum, and an analogy can be proposed by looking at observations of PSR B0656+14. If this pulsar were located at 12 times its current distance, it too would only be found in a single pulse search (Weltevrede et al. 2006).

In the following sections we will discuss some of the properties that differ between pulsars and RRATs. In section 3.2 the discussion will include the different techniques that are used to time the RRATs. On section 3.3, we will talk about the timing results and properties of individual RRATs. In section 3.4 we will present further work that will be done with these data to explore the RRATs population.

3.2 Timing and Analysis Techniques

3.2.1 TOAs

The RRATs' sporadic emission makes them difficult to time using standard pulsar timing techniques. In the standard procedure, it is necessary to fold the data of the entire length of the observation to measure a pulse time-of-arrival (TOA), but with RRATs no pulse profile is detected when this is done. In spite of this fact, TOAs can still be created for a observation; we will describe two ways of doing this.

The first method is the simplest and involves using just a section of data where many bright pulses are seen. The data can be split up in time and only parts of the data where the pulsar is ‘on’ will be used to fold the data and measure a TOA. This has no disadvantages compared to the normal process and is also used when strong RFI affects parts of the observations of regular pulsars.

The second method involves using just a single pulse to measure a TOA. In this method the data are not folded, but are just binned for a single pulse period. This requires knowledge of when a single pulse occurs in a time series. A few disadvantages do exist using this method. Usually (almost always) a single pulse will not be as bright as a folded pulse profile would be for a pulsar. The error on a TOA can be expressed by the pulse width (W) and S/N by

$$\sigma_{\text{TOA}} \simeq \frac{W}{\text{S/N}} \propto \frac{S_{\text{sys}}}{\sqrt{t_{\text{obs}} \Delta f}} \times \frac{P \epsilon^{3/2}}{S_{\text{mean}}}, \quad (3.1)$$

where S_{sys} is the system equivalent flux density, t_{obs} is the observation time, or the pulse period for a single pulse, Δf is the observed bandwidth, ϵ is the duty cycle (W/P), and S_{mean} is the mean flux density of the source. For a given pulsar or RRAT an increase in observation time will decrease the error of a TOA. In addition the emission of individual pulses does not occur at exactly the same pulse phase, a phenomenon called pulse jittering. This is seen in regular pulsars and can be seen in TOAs of RRATs that are created from a single observation (see Figure 3.1). Both of these phenomena decrease our ability to accurately time RRATs but do not prevent us from timing them.

Aside from the slicing up of the data, TOAs for RRATs are produced by the same algorithm as regular pulsars though it is not necessary. In McLaughlin et al (2006) the peak of the individual pulses in the time domain were used instead of transferring it to the Fourier domain to find the fiducial point for the TOA.

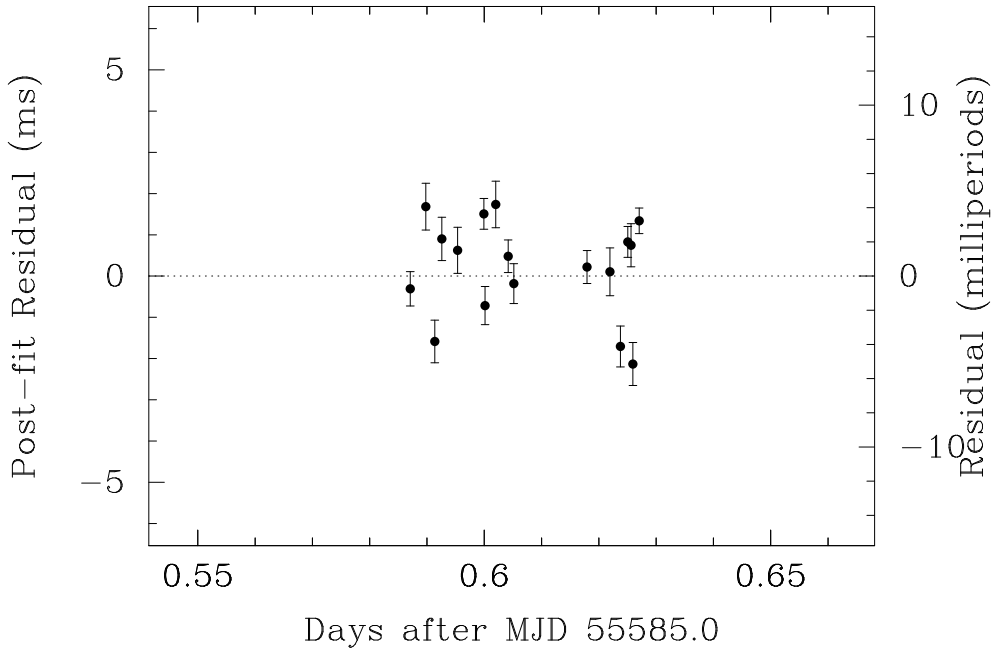


Figure 3.1: A single observation plot of TOAs for PSR J1848–12 showing TOAs varying by more than the error bars on short time scales, possibly indicating that pulse jittering is occurring.

3.2.2 Pulse Profiles and Widths

Pulse widths (W_{50}) are measured from summed pulse profiles which are created through aligning the observations using polycos (a set of polynomial coefficients that predicts when the pulse will arrive) and summing the observations together. Except for PSR J1739–2521 and PSR J1839–0141, all observations where the RRAT was detected were summed together. For PSR J1739–2521 and PSR J1839–0141, the data were used only when the pulsar was on. W_{50} values were measured by fitting a single Gaussian to the summed profile with the exception of PSR J1739–2521, where the W_{50} value was taken across both peaks at the FWHM of each peak.

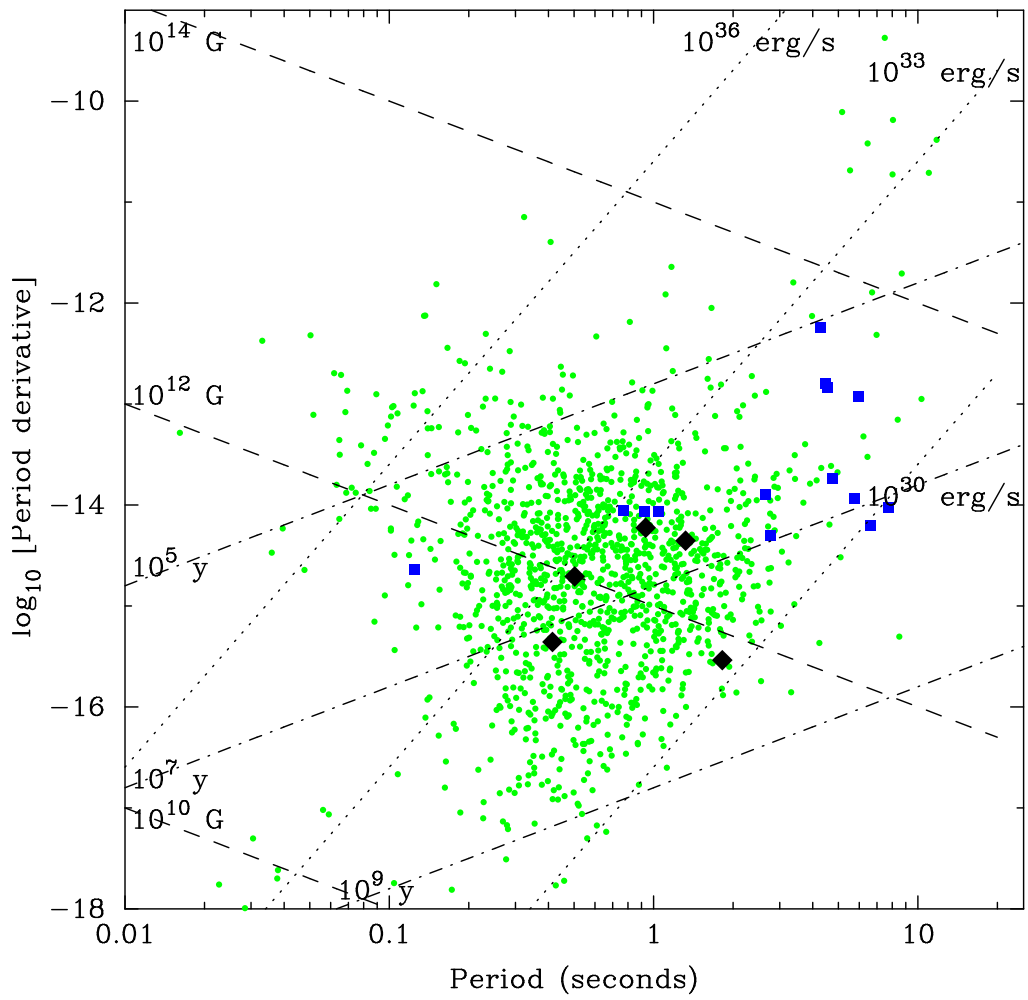


Figure 3.2: A $P - \dot{P}$ diagram showing the new RRATs as black triangles and previously timed RRATs as blue squares. The lines on the plot show constant spin-down luminosity (dots), constant magnetic field (dash), and constant characteristic age (dot-dash). The pulsar population is taken from the ATNF pulsar catalog (Manchester et al. 2005).

3.3 Timing Results

The timing derived parameters for all the RRATs presented in this work are given in Tables 3.3–3.5. Figure 3.2 show a $P - \dot{P}$ diagram with the new RRATs shown as black triangles and all other RRATs as blue squares. In the following subsections some properties of each RRAT will be discussed. All the RRATs with the exception of PSR J1623–0841 were discovered in the PMPS.

3.3.1 PSR J1623–0841

PSR J1623–0841 was discovered in only the single pulse search during processing of the GBT 350-MHz drift-scan pulsar survey and was labeled a RRAT. Later observations at 350 MHz with Spigot showed single pulses but no detections were made at 820 MHz. Gridding observations were unable to localize the position better than the discovery position because of its transient nature. The final TEMPO position was $20'$ away from the discovery position (outside the GBT's 820-MHz beam) and a timing solution was only attainable with the increased sensitivity of GUPPI and a dense set of observations at 350 MHz.

With such a huge offset between observation pointing, a comparison can be made between each observation. An offset in position during an observation acts like a decrease in gain of the telescope, thus decreasing the sensitivity. Figure 3.3 shows single pulses detected from PSR J1623–0841 while pointing at two different sky positions. The top plot shows an observations with a position offset of $20'$ from the bottom plot which was observed much closer to the final position. The bottom

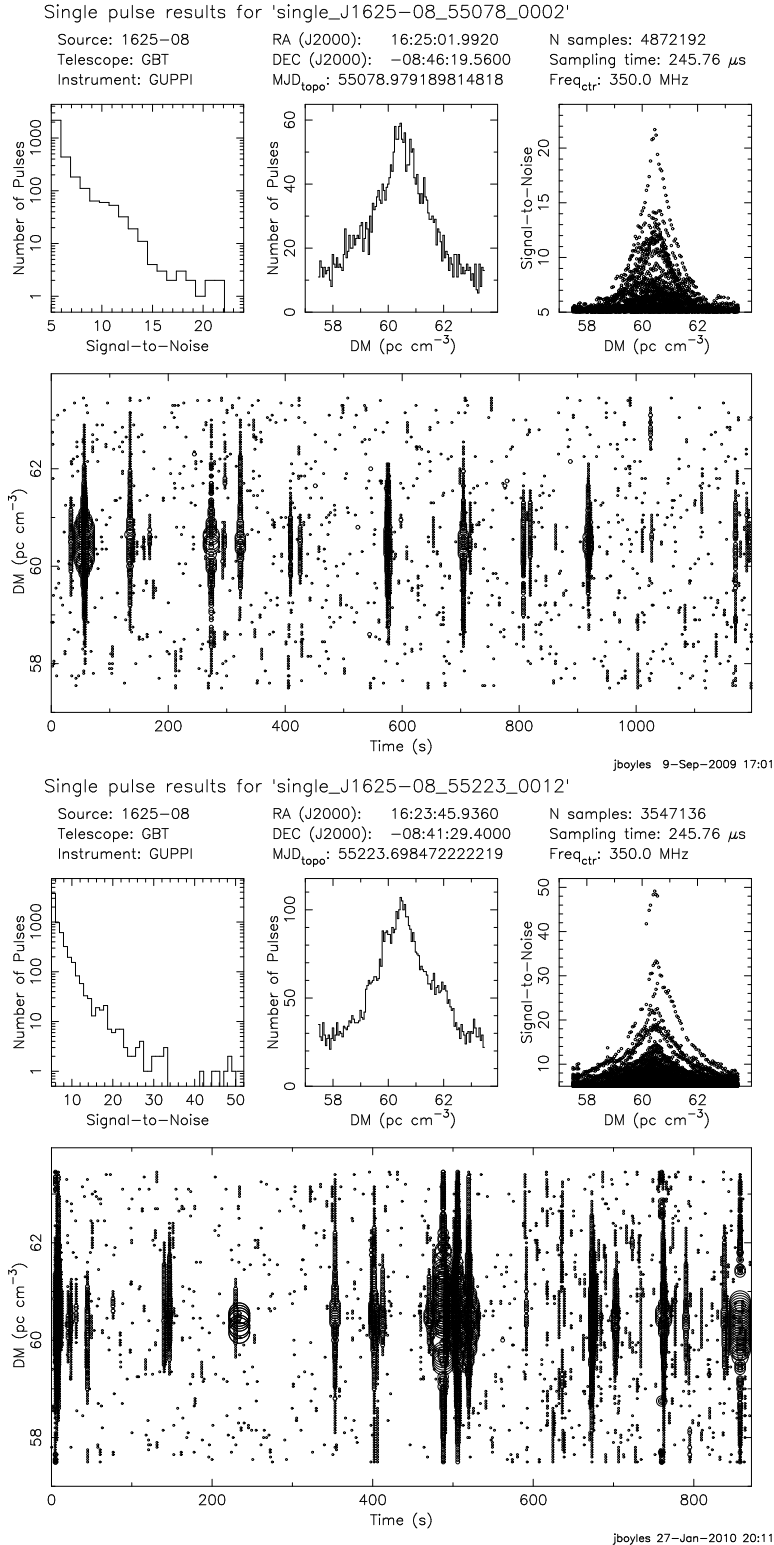


Figure 3.3: Two singlepulse plots for J1623-0841 at two different pointing in the sky taken at 350 MHz with the GBT. The top being offset by 20' and the bottom being on source.

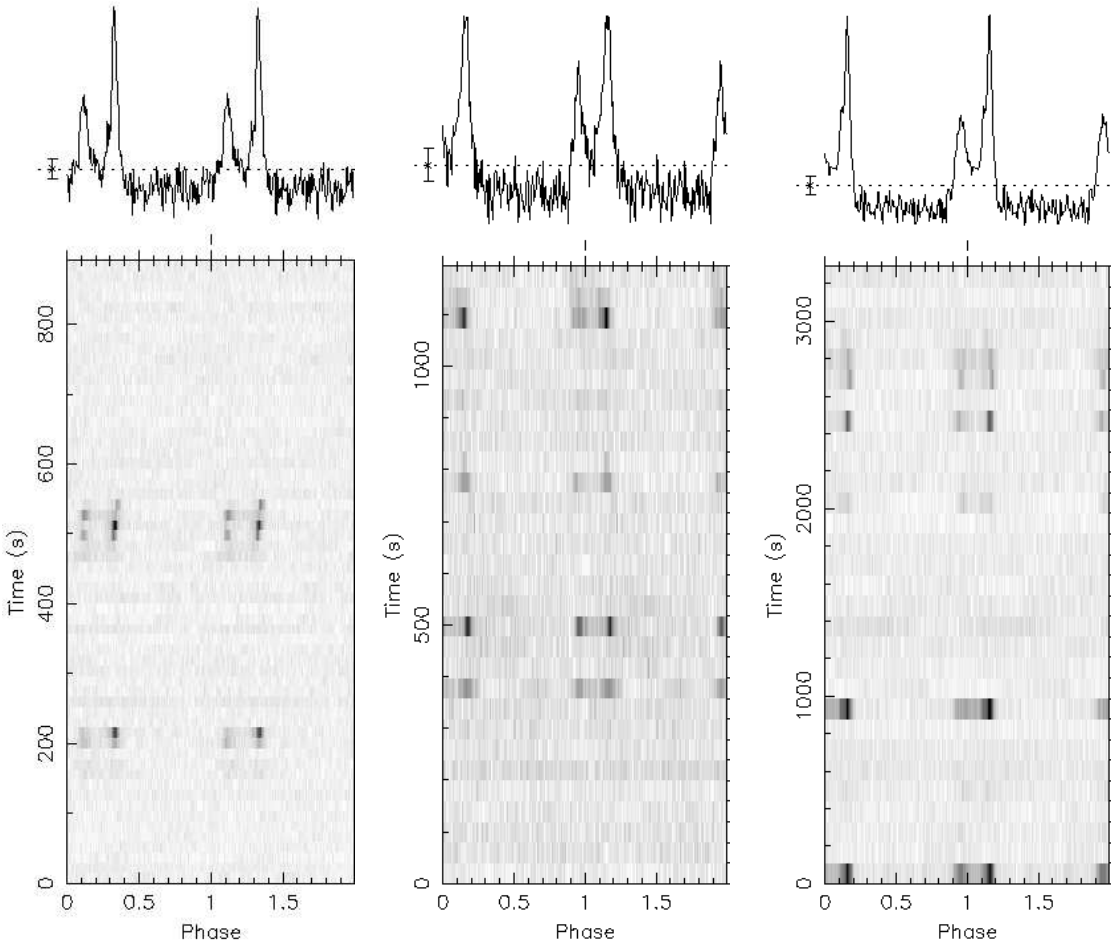


Figure 3.4: Three separate observations of PSR J1739–2521 showing the intermittent nature of this source.

plot shows a higher pulse rate and pulses with higher signal to noise indicating our observations may be sensitivity limited, i.e. we are not seeing all the pulses because we do not have enough sensitivity. However a difference in system temperature between each observation could cause the same result to be seen and can not be ruled out.

3.3.2 PSR J1739–2521

PSR J1739–2521 is the longest period RRAT presented in this work and is the only one that does not have a simple single Gaussian profile and the pulse profile can be seen in Figure 3.4. PSR J1739–2521 has a large offset between the initial observations and final position but unlike PSR J1623–0841 does not seem to have a higher pulse detection rate, which could be an indication that the radio emission is truly turning on and off.

When PSR J1739–2521 was discovered, it was inferred to have a period of ~ 1.2 seconds. Further analysis showed this was not correct and the cause of this incorrect period was due to the fact that both peaks produce single pulses that are detected in the single pulse search. This causes the algorithm that determines the period from single pulses to give a wrong value. Both peaks producing detections in the search, also makes it hard to determine a pulse rate for the source. Each detection must be looked at by eye to determine if a single pulse actually produced two detections in the single pulse search.

3.3.3 PSR J1754–3014

PSR J1754–3014 was originally reported in McLaughlin et al. (2006) with a period of 0.442617 seconds and a DM of 98 pc cm^{-3} . In Keane et al (2011) it was reported to have a period of 1.32049 seconds and a DM of 293 pc cm^{-3} . Here we report a period of 1.32049 seconds and a DM of 99.4 pc cm^{-3} . The difference between our period and McLaughlin et al. (2006) is due to the misidentification of

a terrestrial radio pulse as astrophysical pulse (Keane et al. 2011). The difference between our DM and Keane et al (2011), I believe, is due to PSR J1754–3014’s DM being mixed up with PSR J1839–0141’s new DM. McLaughlin et al. (2006) reported that there was a 32% chance that this RRAT had a different period due to low pulse counts.

3.3.4 PSR J1839–0141

PSR J1839–0141 was originally reported in McLaughlin et al. (2006) with a period of 0.93190 seconds and a DM of 307 pc cm^{-3} . Here it is reported with a period of 0.93326 seconds and a DM of 293.4 pc cm^{-3} . The large difference in DM may be due to the coarse frequency resolution of the PMPS and is less than a 2σ difference from the discovery DM. The discovery period is different by 1.5 ms but it was reported in McLaughlin et al. (2006) that there was a small probability that the period may be different due to low pulse counts and low detection rate. It was only seen in one of ten observations reported in McLaughlin et al. (2006) and has never been seen again with the Parkes telescope since its discovery.

Table 3.1 contains all the observations of PSR J1839–0141 used in this work. The longest single observation of PSR J1839–0141 without a detection is 3593 seconds. If this is used calculate a flux density limit for when PSR J1839–0141 is not emitting, a limit of $5.9 \mu\text{Jy}$ is obtained assuming a detection limit of 6σ for emission at 820 MHz. If the assumption that PSR J1839–0141 is not truly emitting while off, then a null fraction of 98.3% is calculated by taking the total time on and

topocentric MJD start time (days)	time visible (seconds)	start time since start MJD (seconds)	stop time since start MJD (seconds)	observation length (seconds)
55011.205081018517	104	1892	1996	3901
55013.207037037035	90	1785	1875	2697
55041.079328703701	65	123	188	2996
55186.809212962966	120	720	840	1197
55267				3593
55303.439293981479	98	1800	1898	6147
55339.340335648150	128	504	642	6588
55339.340335648150	60	1202	1262	
55339.340335648150	58	2937	2995	
55359				3394
55401.184699074074	56	1240	1296	5575
55432				3593
55460				5172
55494				3593
55522				3593
55550.663599537038	307	1757	2064	3593
55585.547928240740	97	873	970	3593
55612.549386574072	50	1742	1792	2838
55613.544618055559	33	2185	2218	4193
55617.601006944446	95	687	782	1008
55660				3593
55707				3593
55737.329652777778	55	2344	2399	3593
55780.077858796300	14	676	690	3593
55825.914444444446	55	0	55	3593

Table 3.1: Table containing all observations of PSR 1839–0141. Integer MJDs have no detection of PSR 1839–0141 in either periodicity searches or singlepulse searches.

RRAT PSRJ name	Original RaJ HH:MM:SS	Original DecJ DD:MM:SS	Final RaJ HH:MM:SS	Final DecJ DD:MM:SS	Δ Position arcmin
J1623–0841	16:25:02	−08:46:20	16:23:42	−08:41:36	20.55
J1739–2521	17:39:50	−25:13:16	17:39:33	−25:21:16	9.06
J1754–3014	17:54:16	−30:11:37	17:54:30	−30:14:43	4.67
J1839–0141	18:39:53	−01:36:21	18:39:07	−01:41:56	12.8
J1848–1243	18:48:02	−12:47:23	18:48:17	−12:43:26	5.45

Table 3.2: Table containing the discovery position and final position for five RRATs. PSR J1739–2521 and J1839–0141 were both discovered outside the FWHM of the telescope beam size of their survey. PSR J1623–0841 was discovered at 350 MHz with the GBT and its beam is $\sim 36'$.

dividing it by the total observed time.

3.3.5 PSR J1848–1243

PSR J1848–1243 was originally reported with a period of 6.7953 seconds and here we report it to have a period of 0.41438 seconds which is a factor of 16.40 different. PSR J1848–1243 had a 32% chance that its period was incorrect when it was discovered (McLaughlin et al. 2006).

Figure 3.5 shows both a singlepulse detection and folded detection of PSR J1848–1243. The pulsar can be seen in clearly in both detections though weakly in the folded detection. Also note that PSR J1848–1243 can be seen throughout the whole observation time in the folded detection but only about 20 pulses are seen in the singlepulse plot. This is the trend of many pulsar and PSR J1848–1243 may not be a RRAT, just a pulsar missed in the periodicity search during the many processing of the PMPS.

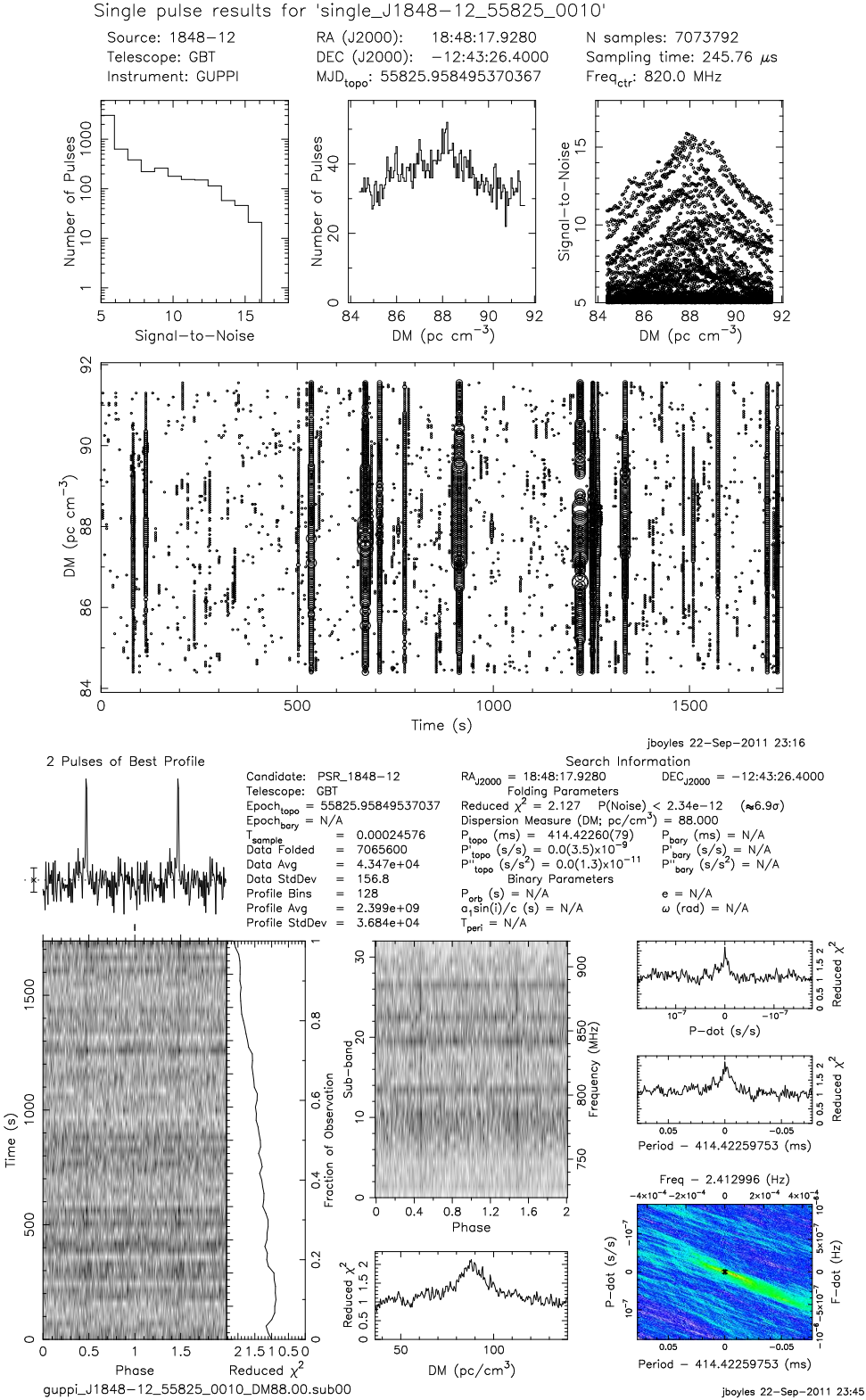


Figure 3.5: A singlepulse plot of PSR J1848-1243 (top) and a folded detection (bottom) shown.

3.4 Summary and Further Work

We present pulsar timing solutions for five of the nineteen that have been obtained for the RRATs population. Obtaining timing solutions are just the first step in understanding this unique population. Further analysis to be conducted includes looking for long term periodicities in the detection rates of PSR J1839–0141 and PSR J1739–2521. Both seem to turn on and off and may have an underlying periodicity associated with them. PSR J1839–0141 is the most promising because it is only seen at most once per observation with PSR J1739–2521 shows up multiple times with different cadences within an individual observation.

Statistical comparisons between the pulsar and RRAT populations may provide additional insight to the RRATs population. From a simple look at Figure 3.2 it seems like the RRATs have longer periods, higher magnetic fields, and smaller characteristic ages than the population of normal pulsars as a whole. Further work with the Kolmogorov-Smirnov test (KS-test), following that which was done in Keane et al (2011), will quantify these results and provide supporting evidence for such statements.

The five RRATs reported in this work are detectable without the single pulse search and may be more like normal pulsar then previously thought. The RRATs may actually be a distinct class of neutron stars but not all objects found only in the single pulse search are RRATs. Sensitivity limits of the current instruments or distant objects like suggested by Weltevrede et al. (2006) make up part of this class of pulsars that are not very erratic.

Parameter	PSR J1623–0841	PSR J1739–2521
Timing Parameters		
Right Ascension (J2000)	16:23:42.711(10)	17:39:32.83(10)
Declination (J2000)	−08:41:36.4(5)	−25:21:16(24)
Spin Period (s)	0.503014992514(6)	1.81846116407(19)
Period Derivative (s s ^{−1})	$1.9582(6) \times 10^{-15}$	$2.9(3) \times 10^{-16}$
Dispersion Measure (pc cm ^{−3})	60.433(16)	186.4
Reference Epoch (MJD)	55048	55612
Span of Timing Data	54635–55522	55339–55825
Number of TOAs	36	32
RMS Residual (μ s)	764	4845
Derived Parameters		
Galactic Longitude (degrees)	5.77	2.3
Galactic Latitude (degrees)	27.3	3.0
Distance (kpc)	3.3	3.5
Distance Off Plane (kpc)	1.5	0.18
Surface Magnetic Field (10^{12} Gauss)	1.00	0.735
Spin-down Luminosity (10^{31} ergs s ^{−1})	19.3	0.00607
Characteristic Age (Myr)	4.07	99.2
W ₅₀ 350 MHz (ms)	6.05(18)	N/A
W ₅₀ 820 MHz (ms)	4.81(8)	497(20)

Table 3.3: Fitted and derived parameters for newly discovered RRATs.

Parameter	PSR J1754–3014	PSR J1839–0141
Timing Parameters		
Right Ascension (J2000)	17:54:30.08(5)	18:39:07.03(3)
Declination (J2000)	−30:14:42(6)	−01:41:56.0(9)
Spin Period (s)	1.3204902915(3)	0.93326564072(6)
Period Derivative (s s^{-1})	$4.424(12) \times 10^{-15}$	$5.943(3) \times 10^{-15}$
Dispersion Measure (pc cm^{-3})	99.38(10)	293.4
Reference Epoch (MJD)	55025	55612
Span of Timing Data	54998–55585	55011–55825
Number of TOAs	24	16
RMS Residual (μs)	3612	1803
Derived Parameters		
Galactic Longitude (degrees)	359.8	30.0
Galactic Latitude (degrees)	−2.3	2.0
Distance (kpc)	2.2	6.2
Distance Off Plane (kpc)	0.08	0.22
Surface Magnetic Field (10^{12} Gauss)	2.44	2.38
Spin-down Luminosity (10^{31} ergs s^{-1})	2.41	9.19
Characteristic Age (Myr)	4.72	2.49
W_{50} 350 MHz (ms)	27.5(2)	N/A
W_{50} 820 MHz (ms)	24.6(7)	7.3(2)

Table 3.4: Fitted and derived parameters for newly discovered RRATs.

Parameter	PSR J1848–1243
Timing Parameters	
Right Ascension (J2000)	18:48:17.980(8)
Declination (J2000)	−12:43:26.6(5)
Spin Period (s)	0.41438334869(2)
Period Derivative (s s^{-1})	$4.403(17) \times 10^{-16}$
Dispersion Measure (pc cm^{-3})	88.0
Reference Epoch (MJD)	55613
Span of Timing Data	55267–55825
Number of TOAs	156
RMS Residual (μs)	1361
Derived Parameters	
Galactic Longitude (degrees)	21.2
Galactic Latitude (degrees)	−5.1
Distance (kpc)	2.4
Distance Off Plane (kpc)	0.21
Surface Magnetic Field (10^{12} Gauss)	0.432
Spin-down Luminosity (10^{31} ergs s^{-1})	7.78
Characteristic Age (Myr)	14.9
W_{50} 820 MHz (ms)	4.8(5)

Table 3.5: Fitted and derived parameters for newly discovered RRATs.

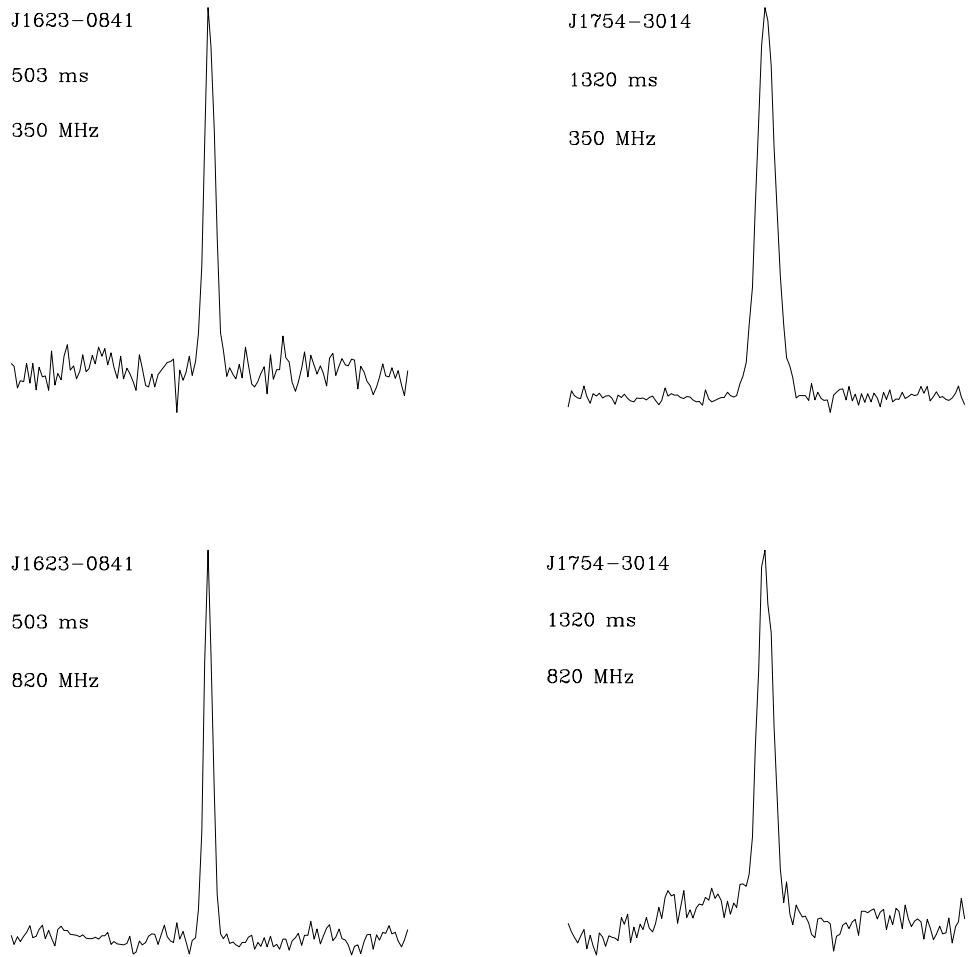


Figure 3.6: Pulse profiles for PSR J1623–0841 and PSR J1754–3014 at 350 MHz and 820 MHz. The profiles are created by folding each observation and summing all profiles together.

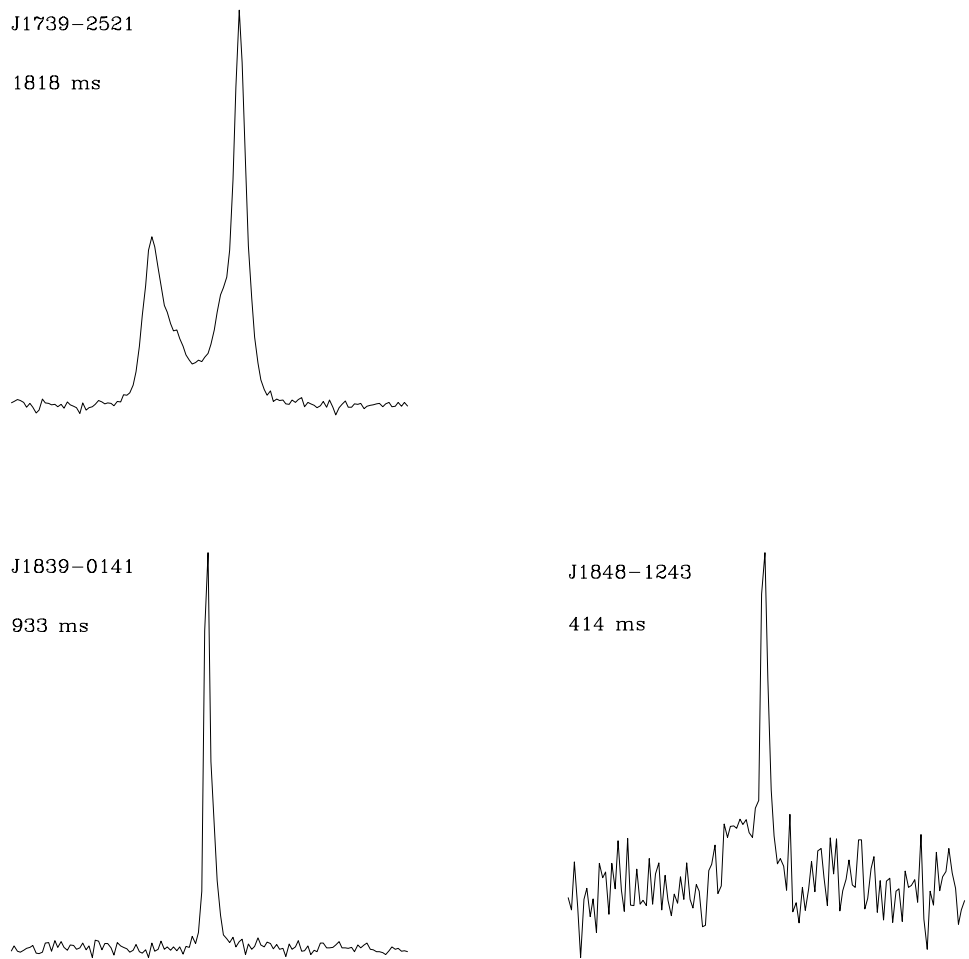


Figure 3.7: Pulse profile at 820 MHz for the rest for the rest of the RRATs. Both of PSR J1739–2521 and PSR J1839–0141 profiles are a sum of data only when the pulsar is on. PSR J1848–1243’s profile is created in the same way as PSR J1625–0841 and PSR J1754–3014.

Chapter 4

Young Radio Pulsars in Galactic Globular Clusters

Abstract

Currently three isolated radio pulsars and one binary radio pulsar with no evidence of any previous recycling are known in 97 surveyed Galactic globular clusters. As pointed out by Lyne et al., the presence of these pulsars cannot be explained by core-collapse supernovae, as is commonly assumed for their counterparts in the Galactic disk. We apply a Bayesian analysis to the results from surveys for radio pulsars in globular clusters and find the number of potentially observable non-recycled radio pulsars present in all clusters to be < 3600 . Accounting for beaming and retention considerations, the implied birth rate for any formation scenario for all 97 clusters is < 0.25 pulsars per century assuming a Maxwellian distribution of velocities with a dispersion of 10 km s^{-1} . The implied birth rates for higher velocity dispersions are substantially higher than inferred for such pulsars in the Galactic disk. This suggests that the velocity dispersion of young pulsars in globular clusters is significantly lower than those of disk pulsars. These numbers may be substantial overestimates due to the fact that the currently known sample of young pulsars is observed only in metal-rich clusters. We propose that young pulsars may only be formed in globular clusters with metallicities with $\log[\text{Fe}/\text{H}] > -0.6$. In this case, the potentially observable population of such young pulsars is 447_{-399}^{+1420} (the error

bars give the 95% confidence interval) and their birth rate is $0.012^{+0.037}_{-0.010}$ pulsars per century. The mostly likely creation scenario to explain these pulsars is the electron capture supernova of a OMgNe white dwarf.

4.1 Introduction

Since the first discovery of PSR B1821–24 in M28 (Lyne et al. 1987), 143 pulsars¹ have been discovered in 27 globular clusters (GCs). While the majority of GC pulsars are thought to have been formed in low-mass X-ray binary systems, in which the neutron star has been spun up to millisecond periods by the transfer of matter from an evolved companion (see, e.g. Camilo & Rasio 2005 for a recent review), a small minority of the GC pulsar population appear to be similar to the isolated “normal” pulsars which inhabit the disk of our Galaxy (i.e. spin periods (P) of several hundred ms, characteristic ages (τ_c) of 10^7 – 10^8 yr, and inferred dipole magnetic field strengths (B) of 10^{11} – 10^{12} Gauss). These pulsars were originally discussed by Lyne et al. (1996) who noted that, since no significant star formation has occurred in GCs in the last billion years (Briley et al. 1994), this population appears to be highly anomalous. Lyne et al. (1996) also note that the young pulsars appear in metal-rich GCs. This trend has persisted despite fifteen years of intense searches of most of the cluster population. A goal of this work is to investigate the statistical and astrophysical significance of this result.

Recent improvements in observational systems over the past decade have led

¹For an up-to-date list of known globular cluster pulsars, see <http://www.naic.edu/~pfreire/GCpsr.html>

to a wealth of discoveries of pulsars in GCs. Sensitive radio surveys for pulsars have been conducted on almost 100 GCs to date. The two most fruitful have been Terzan 5 (Ransom et al. 2005) and 47 Tucanae (Freire et al. 2001) with 34 and 23 pulsars respectively. Neither of these clusters harbor any normal pulsars, which we will henceforth define as being pulsars with spin periods $P > 100$ ms and inferred magnetic field strengths $B > 10^{11}$ Gauss. This is somewhat surprising, given that the significant selection effects known to hamper the detection of binary and millisecond pulsars in clusters (Camilo & Rasio 2005) are not as severe for normal isolated pulsars.

Clearly, some physical mechanism is at work which produces these apparently young pulsars in GCs in a different way to how we believe they are formed in the disk of our Galaxy. One possible method is the collapse of a white dwarf via an electron capture supernova in a binary or collisional system (Ivanova et al. 2008). In this paper, we revisit the statistics of the normal pulsars based on the results of recent surveys, and recent studies of the Galactic population of normal pulsars (Faucher-Gigu  re & Kaspi 2006 (hereafter FK06); Ridley & Lorimer 2010). In §4.2, we review the current sample of normal pulsars in GCs. In §4.3, we compile a list of flux-density detection limits for 97 GCs based on published searches and some recent unpublished results. In §4.4, we use these limits to characterize the population of young pulsars. In §4.5 we discuss the intrinsic population and birth rate of young pulsars in GCs. In §4.6 we discuss formation scenarios and future work with young globular cluster pulsars.

4.2 The current sample of young pulsars in GCs

At least three, possibly four, young pulsars are known in two or three GCs. These four pulsars are B1718–19 in NGC 6342, B1745–20 in NGC 6640, and J1823–3021B and J1823–3021C in NGC 6624. The properties of these pulsars are summarized in Table 4.2 and their GC properties relevant to this data analysis can be seen in Table 4.3. As can be seen by inspecting their position with respect to other normal Galactic field pulsars on the $P-\dot{P}$ diagram shown in Figure 4.1, these pulsars appear to be consistent with the distribution of normal pulsars in the Galactic disk.

Two long-period pulsars are not included in this compilation. Firstly, the 110-ms pulsar B2127+11A in GC NGC 7078 which is known to have a negative period derivative due to contamination by the cluster potential and nearby stars (Wolszczan et al. 1989). As discussed by these authors, the pulsar most likely has a small intrinsic period derivative indicating that it has undergone some recycling in a binary system which has subsequently been disrupted due to close encounters in the cluster. It is also noted that a recent measurement of the second period derivative of $\ddot{P} = 3.2 \times 10^{-29} \text{ s}^{-1}$ for this pulsar is entirely consistent with encounters with nearby stars in the cluster (Jacoby et al. 2006). Another long-period pulsar which we do not consider to be young is the 110-ms pulsar J1750–37A in GC NGC 6441 (Freire et al. 2008). This is a member of an eccentric binary system and its low period derivative places it closer to the region of the $P-\dot{P}$ diagram occupied by the double neutron star binary systems and the eccentric neutron star–white dwarf

binaries (see Figure 4.1).

One other caveat needs to be discussed with the sample of young pulsars present in this paper. PSR B1718–19 may not truly be a member of NGC 6342 and is the only pulsar located near NGC 6342. An earlier discussion of this subject is presented in Bailes et al. (2005) and a further expansion will be presented here. The original paper used PSR B1718–19’s position, binary status, and dispersion measure (DM) to argue for its association with NGC 6342. Its position of 2.3° away from the cluster’s center is 3 times greater than the half-mass radius of the cluster. All other young pulsars presented in Table 4.2 and a majority of all globular cluster pulsars with timing solutions are found within the half-mass radius. The DM of 75.7 pc cm⁻³ for PSR B1718–19 is somewhat below the predicted values of 120 pc cm⁻³ using $DM = 20/\sin(b)$ pc cm⁻³ (Lyne et al. 1995) where $b = 9.72^\circ$, 130 pc cm⁻³ (Taylor & Cordes 1993), or 229 pc cm⁻³ (Cordes & Lazio 2002). These DM models are uncertain, but factors in the range of 1.5 to 3 are larger than the known differences for sources within $|b| < 10^\circ$ of the Galactic plane. The unusual binary nature of PSR B1718–19 gives support to its association with NGC 6342 due to its existence as a eclipsing low-mass binary pulsar (Freire 2005) and due to the fact that the proportion of pulsars with binary companions is about two orders of magnitude greater for GC pulsars than Galactic field pulsars (Lyne et al. 1995). In the following sections, given the lack of clear evidence for or against the association, the results are discussed both with and without the inclusion of PSR B1718–19 and will be explicitly stated when PSR B1718–19 is not included.

PSR	B1718–19	B1745–20	J1823–3021B	J1823–3021C
Cluster	NGC 6342	NGC 6440	NGC 6624	NGC 6624
P (ms)	1004	288	379	406
\dot{P} (s s $^{-1}$)	1.6×10^{-15}	4.0×10^{-16}	3.0×10^{-17}	2.2×10^{-16}
DM (pc cm $^{-3}$)	75.7	219.4	86.9	86.7
B (G)	1.3×10^{12}	3.4×10^{11}	1.1×10^{11}	3.0×10^{11}
τ_c (yrs)	9.8×10^6	1.1×10^7	2.0×10^8	2.9×10^7
S_{1400} (mJy)	0.30	0.37	1.04	0.71
Binary?	Yes	No	No	No
Reference	Lyne et al. (1993)	Freire et al. (2008)	Lynch et al. (2011)	Lynch et al. (2011)

Table 4.1: The four young pulsars currently known in GCs

4.3 Sensitivity limits for young pulsars in GCs

To carry out the statistical analysis of this sample, it is necessary to have a substantial compilation of upper limits from GCs that have been searched for such pulsars. Table 4.3 gives our compilation of flux density limits at 1400 MHz for searches of each cluster, S_{\min} and GC properties relevant to this work. The main surveys that were used are Hessels et al. (2007), Lynch & Ransom (2011), Lynch et al. (2011), and Possenti et al. (2010). The rest of the GCs had their flux limits taken from the most recent discovery paper. If the paper did not quote a flux limit, one was derived using the survey parameters from the paper using the radiometer equation for pulsars which gives

$$S_{\min} = \frac{\beta(S/N_{\min})T_{\text{sys}}}{G\sqrt{n_p t_{\text{int}} \Delta f}} \sqrt{\frac{\delta}{1-\delta}}, \quad (4.1)$$

where β is a digitization correction factor, S/N_{\min} is the minimum signal-to-noise ratio, T_{sys} is the system temperature of the telescope, G is the gain of the telescope, n_p is the number of polarizations summed, t_{int} is the observation time, Δf is the bandwidth of the backend, and δ is the fractional pulse width (Lorimer & Kramer 2005).

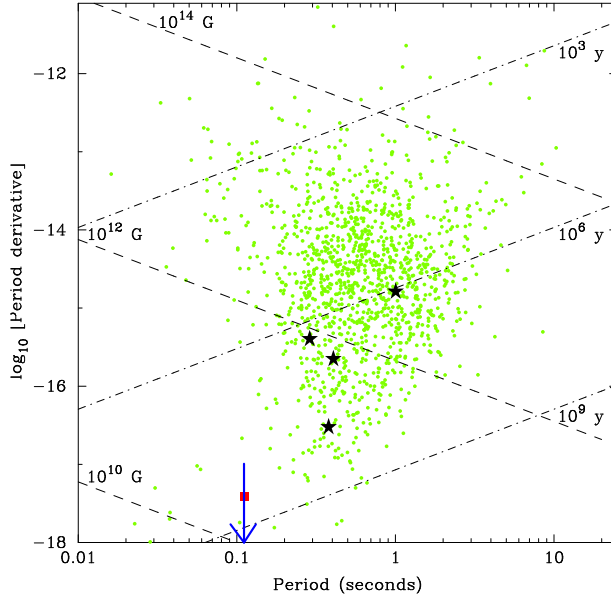


Figure 4.1: $P-\dot{P}$ diagram showing young globular cluster pulsars as black stars and PSR J1750–37A as a red square. PSR B2127+11A is shown as a blue arrow with the arrow representing the limit on period derivative at the bottom of the diagram. Dashed lines are lines of constant magnetic field and dot dash lines are lines of constant characteristic age. The pulsar population data are taken from the ATNF pulsar database (Manchester et al 2005).

The parameters t_{int} , Δf , and n_p are all taken from the relevant survey paper.

The values for G and β can be obtained from the websites or papers that give the telescope and backend specifications. S/N_{\min} and δ are parameters that are chosen to have values of 8 and 0.1 respectively. T_{sys} can be expressed as:

$$T_{\text{sys}} = T_{\text{rec}} + T_{\text{CMB}} + T_{\text{gsyn}} + T_{\text{spill}} + T_{\text{RFI}}, \quad (4.2)$$

where T_{rec} is the receiver temperature, T_{CMB} is the cosmic background temperature, T_{gsyn} is the Galactic synchrotron temperature, T_{spill} is the spillover temperature from sources in the side lobes of the telescope, and T_{RFI} is the increase in system temperature due to terrestrial radio frequency interference (RFI). The values of T_{rec} ,

T_{CMB} , and T_{gsyn} are well known, but T_{spill} and T_{RFI} can vary greatly with time and telescope position causing large uncertainties in T_{sys} and can only truly be obtained by proper calibration. Due to pulsar survey observations rarely ever having accurate calibration, the expression for T_{sys} has been simplified to include only the T_{rec} , T_{CMB} , and T_{gsyn} . One last fact to mention is that, due to these pulsars having long periods, DM smearing and scattering are unlikely to be important and are not considered in this work.

For any surveys which were not carried out at 1400 MHz, the quoted limits are scaled from the observing frequency to 1400 MHz using a simple power law $S \propto \nu^{-1.6}$, which is consistent with the average spectral behavior for a large sample of normal pulsars (Lorimer et al. 1995).

4.4 The potentially observable population of young pulsars in GCs

For all clusters listed in Table 4.3, we can use the flux density limits to model the most likely number of potentially observable pulsars² in each cluster. Using a binomial data model, we carry out a simple Bayesian analysis described below. This method rests on a key simplifying assumption about the luminosity function of young pulsars. Following Faucher-Giguère & Kaspi (2006), we will assume that the parent population follows a log-normal luminosity function defined (at 1400 MHz) to have a mean in the base-10 logarithm of L (in mJy) to be -1.1 and a standard deviation of 0.9. This assumption is reasonable if we consider that the spin-down

²The estimates in this section do not account for beaming effects, or the fact that many pulsars will escape the cluster potential and will be missed by the surveys. We discuss these issues in §4.5.

evolution of isolated pulsars in GCs is the same as the Galactic disk. Variations on the mean and standard deviation of the log-normal luminosity function have been applied to our analysis using models from Ridley & Lorimer (2010). These values are in the range of -1.04 to -1.19 for the mean of the luminosity function in the base-10 and in the range of 0.91 to 0.98 for the standard deviation.

We can model the number of pulsars in a particular cluster, N , given a “detection probability” θ and an observed sample of n pulsars. Bayes’ theorem gives the joint posterior probability density for N and θ as

$$p(N, \theta|n) \propto p(n|N, \theta)p(N, \theta). \quad (4.3)$$

Here $p(n|N, \theta)$ is the probability of observing n pulsars from a parent population of N with some θ , and $p(N, \theta)$ is the joint prior probability density for N and θ . The prior distribution for N is assumed to be uniform in the range n to ∞ . Graphically, θ is the ratio of the area under the luminosity function for $L > L_{\min}$ to the total area under the function. We evaluate θ numerically using Monte Carlo integration of the Faucher-Giguère & Kaspi (2006) luminosity function and four luminosity functions from Ridley & Lorimer (2010). The prior distribution for θ is assumed to be independent of N and uniform in the range θ_{\min} to θ_{\max} , which are defined to be the minimum and maximum probabilities from the five distribution functions. The simplest choice for a likelihood function is the binomial distribution, i.e.

$$p(n|N, \theta) = \frac{N!}{n!(N-n)!} \theta^n (1-\theta)^{N-n}, \quad (4.4)$$

where θ depends on the luminosity limit and the assumed parent luminosity function.

For the majority of cases in which there are no detections in a cluster, $n = 0$ and the likelihood term simplifies considerably to

$$p(n|N, \theta) = (1 - \theta)^N. \quad (4.5)$$

For the cases of NGC 6440 and NGC 6342, where there is one detection, i.e. $n = 1$, we have

$$p(n|N, \theta) = N\theta(1 - \theta)^{N-1}, \quad (4.6)$$

while for the two pulsars in NGC 6624, $n = 2$ which leads to

$$p(n|N, \theta) = \frac{N(N-1)}{2}\theta^2(1 - \theta)^{N-2}. \quad (4.7)$$

Having found the joint posterior distribution $p(N, \theta|n)$, we then marginalize over θ to get the posterior distribution for N using the appropriate choice for the likelihood function (i.e. Eq. 4.5, 4.6, or 4.7 depending on the value for n in each case) and give the 95% percentile-based credible intervals for N (i.e. the 0.025 and 0.975 percentiles) as well as the median in Table 4.4. Examples of these discrete probability density functions can be seen in Figure 4.2 for four GCs. 47 Tuc shows the typical shape of a discrete probability density function for a GC with no young pulsars.

4.5 The intrinsic population and birth rates of young GC pulsars

The results from the previous sections do not take into account the population of young pulsars whose emission beams do not intersect our line of sight or the population of young pulsars which escaped the gravitational potential of their parent GCs. Both of these issues are addressed in this section.

4.5.1 Results for all GCs

Retention fractions (f_R), the fraction of pulsars which do not have a large enough birth velocity to escape the cluster's gravitational potential, are calculated for each GC. These f_R are obtained by using the escape velocity of the GC and a velocity distribution function. Hobbs et al. (2005) showed that a Maxwellian distribution fits the Galactic population of pulsars well for many categories (all, young, recycled, etc.) of pulsars, hence we choose the velocity distribution function to have the form of a Maxwellian with a dispersion σ_v . Caution does need to be taken with this choice of velocity distribution function because no physical mechanism is presented in Hobbs et al. (2005) to explain this Maxwellian distribution and the low velocity end of this distribution is not well constrained due to the fact low velocity pulsar's proper motions are difficult to measure. Multiple values were chosen for σ_v : 265 km s⁻¹ from Hobbs et al. (2005), an intermediate value of 130 km s⁻¹, 50 km s⁻¹, 20 km s⁻¹, and 10 km s⁻¹ as a lower value. Many separate values have been chosen because it is most likely that these young GC pulsars are formed from electron capture supernovae for which the accompanying natal kick may be 10 times

smaller than in the case of core collapse supernova (Ivanova et al. 2008, Kitaura et al. 2006). The escape velocities were taken from Gnedin et al. (2002) except for ESO 452 which came from Webbink (1985). The retention fractions are calculated by numerically integrating the Maxwellian velocity distribution function from 0 to the escape velocity of the GCs.

Each retention fraction was used to calculate a theoretical upper limit for the number of young pulsars produced for every GC

$$N_{\text{created}} = \frac{N}{f_R f_{\text{beam}}}, \quad (4.8)$$

where N represents the number of pulsars predicted by the binomial method, i.e the median in Table 4.4, and f_{beam} is the beaming fraction for pulsars. The value taken for the pulsar beaming fraction is 0.1 (Tauris & Manchester 1998). This value represents an upper limit on the number of pulsars created in a particular GC. The number of pulsars created in a GC is then divided by the average life time of a young pulsar (43 Myr) to obtain upper limits on the birth rates (\mathcal{R}) for each GC. An average lifetime of 43 Myr is derived by taking the total number of Radio-Loud pulsars (1,200,000) and dividing it by the pulsar birthrate (2.8 psrs per century) in FK06. All results from the binomial analysis are contained within Table 4.4.

One GC, M22, has median value of zero and no young pulsars are expected to be contained within it. This results in a birth rate of zero for M22. To calculate a birth rate for this GC, it is assumed that the cluster contains one pulsar and an upper limit is constructed using this assumption.

4.5.2 Metal-rich GCs

Up to this point, the analysis presented uses flux density limits and luminosity models as the only considerations for observable pulsars contained within the cluster. Lyne et al. (1996) note that the young pulsars appear in metal-rich GCs and this trend has persisted despite fifteen years of intense searches of most of the cluster population. In this section metallicity will also be added as a consideration. For the following discussion Terzan 5 will be excluded due to the possibility that it is not a true GC but a merger of two astrophysical objects that are bound in the Galactic halo (Ferraro et al. 2009). Also excluded will be B1718–19 in NGC 6342 due to the uncertainty about its membership to its cluster (see §4.2).

The GCs NGC 6440 and NGC 6624 have metallicities that are greater than the 90th percentile of metal rich clusters. These two clusters are two of the three highest metallicity clusters that contain either young or old millisecond pulsars. The probability of selecting two GCs in the top three of a ranked list from a sample of 25 GCs is 0.92 %. If NGC 6342 is also included in this sample then we have three of the top five highest metallicity clusters with a probability of selecting three of the top five of 0.38 %. The inclusion of Terzan 5 (the highest metallicity cluster with any known pulsars) in both of these previous scenarios, changes the probability values from 0.92 % to 1.71 % and 0.38 % to 0.68 %. The conjecture can be proposed that metal-poor clusters have been selected against for the purpose of surveying GCs due to the belief that metal-rich GCs contain more pulsars overall. Figure 4.3 shows a plot of metallicity versus survey luminosity limit, indicating a random distribution

with no bias towards either low or high metallicity clusters.

Figure 4.4 shows the empirical cumulative distribution function (CDF) of the number of predicted young pulsars with the binomial method versus metallicity. GCs with distances greater than 20 kpc are excluded from this CDF because their large distances produce high luminosity limits and in turn creates jumps in the CDF. The cause of these jumps seen in Figure 4.4 is due to high survey limits on specific GCs. The first large jump in the CDF at a metallicity of ~ -0.55 is due to NGC 6342, the GC with the highest survey luminosity limit.

The GCs with the most known pulsars, Ter 5 and 47 Tuc, have high metallicities and have been used in many simulations. One of these presented in Ivanova et al. (2008) attempts to model the number of young/high magnetic field pulsars in these clusters. In these simulations, 3 and 2 young pulsars are predicted to exist in the cores of Ter 5 and 47 Tuc respectively with the most likely creation scenario being the merger of two stars. If beaming and luminosity limits from Table 4.3 are taken into account, the chances of seeing those 2-3 pulsars are extremely small.

4.6 Discussion

4.6.1 Flux Luminosity Limits

The results of the binomial analysis depend greatly on the luminosity limits provided from searching these GCs. One can see by comparing the discrete probability density functions of NGC 6342 and NGC 6440 seen in Figure 4.2, that the range of values that each function covers differs greatly. This is a direct result of

NGC 6342's flux luminosity limit being much greater than that of NGC 6440. Thus clusters with high flux luminosity limits do not significantly constrain the population/birth rates of these GCs.

Another factor not mentioned is the influence of RFI on searching GCs. The relative impact of RFI on long-period pulsars is much more severe than for millisecond pulsars (MSPs). There is a lot more long-period RFI and the dispersion discrimination between RFI and long-period pulsars is not nearly as great as for MSPs. Therefore this creates a bias against finding such pulsars because they may be ignored assuming they are RFI which is hard to quantify and fully account for.

4.6.2 Birth Rates in GCs

For most GCs, the birth rates found are only upper limits with the exception of NGC 6342, NGC 6440, and NGC 6624. Empirical CDFs of these values can be seen in Figure 4.5 for the 97 GCs surveyed. The upper limits on birth rates for velocity dispersions of 265, 130, 50, 20, and 10 km s⁻¹ are 3568, 422, 24.8, 1.67, and 0.25 pulsars per century respectively. The higher birth rates obtained from the higher velocity dispersions is an effect of needing to produce more pulsars to get enough pulsars at the low velocity end of the Maxwellian distribution. These values for birth rates provided in this work are much higher than the predicted birth of 2.8 pulsars per century for the Galaxy as a whole for larger velocity dispersions (Faucher-Giguère & Kaspi 2006). The impact on the Galactic population from pulsars escaping GCs will be discussed elsewhere (Lynch et al., in prep). For the

purposes of this paper, these very high implied birth rates suggest that a very different formation process for young pulsars is occurring in GCs, as well as the possibility that some GCs do not produce young pulsars at all. The major difference in the formation scenario appears to be the lower velocity dispersion at birth.

4.6.3 Role of cluster metallicity

In Section 5.2, evidence is presented that young pulsars are only present in higher metallicity GCs. Another way to highlight this is to use a simple population model with the GC’s mass as the only variable. A pulsar to mass ratio (PMR) is derived using the results of the binomial analysis for NGC 6440 and NGC 6624, each having 10 and 21 pulsars predicted respectively. We do not include the GC NGC 6342 when creating this model because of the uncertain cluster membership of B1718–19 (see §4.2). With NGC 6440’s mass of 811,000 M_{\odot} and NGC 6624’s mass of 257,000 M_{\odot} a PMR of 31 pulsars per 1,068,000 M_{\odot} is obtained. Using the PMR each of the 97 GCs are revisited and an intrinsic population is predicted for each GC by multiplying the PMR by the GC mass. Using the flux density limits in Table 4.3, the observable population is drawn from the Faucher-Giguère & Kaspi (2006) luminosity model. The results of this simulation can be seen in a histogram in Figure 4.6 and Table 4.4. Seventy-four percent of the GCs are predicted to have no observable young pulsars using this model. However, for the remaining GCs, a total of 67 young pulsars should be observable which disagrees with the current population of 3 by over an order of magnitude. These results show that mass is not

a single determining factor in a GC containing young pulsar.

Based on the observed population of young pulsars in the higher metallicity GCs, it may be suggested that lower metallicity GCs may not produce any young pulsars. Figure 4.5 may be used to predict birth rates as a function of metallicity. Given that no young pulsars are observed with metallicities below -0.6 , this value is adopted as a cut-off value. In this case, the population of young pulsars in GCs with $\log[\text{Fe}/\text{H}] > -0.6$ is 447^{+1420}_{-399} , at 95% confidence level. This implies an upper limit on the birth rate for GCs with $\log[\text{Fe}/\text{H}] > -0.6$ of $0.012^{+0.037}_{-0.010}$ pulsars per century.

4.6.4 Formation scenarios

A few possible situations need to be examined that could explain this current population of normal pulsars in globular clusters.

4.6.4.1 Blue Stragglers

Blue stragglers are the product of the merger of two or possibly three $\sim 1 M_{\odot}$ main sequence stars (Leonard, 1989) or binary accretion of a binary companion(s) (McCrea, 1964). They cannot be the progenitors of the young pulsars because they are not massive enough to core collapse.

4.6.4.2 Electron Capture Supernovae

The creation of these normal pulsars from electron capture supernova (ECS) of Oxygen-Neon-Magnesium (ONeMg) white dwarfs is another possible avenue. There are three main types of ECSs: accretion-induced collapse (AIC), evolution-induced collapse (EIC), and merger-induced collapse (MIC), of which AIC is the most common (Ivanova et al. 2008). From conservation of magnetic flux, a five order of magnitude change in surface magnetic field is available from an AIC of a white dwarf into a neutron star. This would require a white dwarf to have at least 10^7 Gauss magnetic field to produce the magnetic field of the young pulsar with the largest magnetic field contained within a GC. White dwarfs have been observed with magnetic field above 2×10^6 Gauss and could account up to 10% of the white dwarf population (Liebert et al 2003). ECSs could be an avenue for the creation of young pulsars. Not all white dwarfs that pass the Chandrasekhar limit will collapse via ECS, some will be type Ia supernova.

ECS provide two qualities that are needed to explain the presence of young pulsars in GCs. The first is the low velocity dispersion which is needed to keep these young pulsars in their host GCs. The initial formation of the white dwarf results in a small velocity kick of a few km/s from either stellar winds or an asymmetric kick during the helium flash (Fregeau et al. 2009). The energetics of the ECS of the white dwarf would produce a small velocity kick (Dessart et al. 2006) and, combined with the velocity kick from previous stages of evolution, would provide a total velocity that is small and would allow most neutron stars created via ECS to be retained by

the GC. The second is the higher metallicity of GCs which host young pulsars. An ECS ejects a few $0.001 M_{\odot}$ worth of mass, of which $\sim 25\%$ is ^{56}Ni (Dessart et al. 2006). ^{56}Ni decays into ^{56}Co with a half-life of $\simeq 6$ days and then ^{56}Co decays into ^{56}Fe with a half-life of $\simeq 77$ days. This provides a source of iron creating the higher metallicity for clusters in which all known young pulsars have been detected.

A simple statistical analysis can give an order of magnitude estimate of the possible population of heavy mass ($1.0\text{--}1.4 M_{\odot}$) white dwarfs available for ECSs. It is taken that all GCs have the same initial mass function (IMF) and the differences seen between current GC's mass functions are due to the dynamical history of the cluster (Paust et al. 2010). The IMF is a multi-part power-law presented in equation 4 of Kroupa (2002) and with $\alpha_3 = -2.7$ from Scola (1986). Each GC is assumed to have the same age of 12.4 Gyr for purposes of predicting an initial mass of the GC (Krauss & Chaboyer 2001). An initial mass is obtained for each GC by using the mass lost fractions presented in Kroupa (2002) for $\alpha_3 = -2.7$. The number of main sequence stars available for heavy white dwarfs (mass range of 6.0 - $8.0 M_{\odot}$) are calculated for each GC with a total of $\sim 150,000$ white dwarfs formed in these 97 GCs. The use of values for α_3 greater than -2.7 serves only to decrease the numbers of stars in this mass range while choosing the Salpeter index of $\alpha_3 = -2.35$ only increases the number of stars available by a factor of 2 (Salpeter 1955). Assuming an interaction age of 10^9 years and that each heavy white dwarf creates one ECS, an occurrence rate of 1.5×10^{-2} ECSs per century is obtained and is shown on Figure 4.5 as a solid horizontal black line.

This predicted ECS rate is an order of magnitude less than the birth rates of

pulsars for the lowest velocity dispersion. A few factors could bring these values into closer agreement. A decrease in the interaction age would increase the ECS rate. This is a very plausible possibility because there is an accumulation of ECSs at more recent times due to dynamical evolution (it may take a long time for a given capture to form an accreting binary) and individual evolution (it may take several Gyrs to accrete enough mass to cause an ECS). Lower luminosity limits without the detection of more young pulsars would decrease the young pulsar birth rate and bring the two rates closer to agreement. A detailed N -body simulation should be used to refine the ECS rate but this is beyond the scope of this work. It is possible that ECSs have only occurred in higher metallicity cluster and not all GCs should be considered in calculating the birthrate of young pulsars. The work presented here suggests that ECS is the most likely creation scenario for young pulsars in GCs.

4.6.4.3 Galactic Bulge Pulsars

One other possibility is that these young pulsars are part of the Galactic field population and are captured by their host GC. The time it would take to travel the distances to the GCs and the time it would take for these pulsars to relax into the core of their host GC have been proposed as evidence against this method. One key fact is neglected here; these are all bulge GCs that contain this population of young pulsars. Their distances from the Galactic center range from 1.2–1.7 kpc and the radius of the Galactic bulge is ~ 1.5 kpc. The time for a pulsar to travel from the outer 0.5 kpc of the Galactic bulge would be short ($\sim 10^6$ years) even for a

Globular Cluster	l ($^{\circ}$)	b ($^{\circ}$)	D (kpc)	D_{GC} (kpc)	r_t (pc)	S_{min} (mJy pc 2)	Mass (M_{\odot})	V_{σ} (km s $^{-1}$)
NGC 6325	0.9	8.0	7.8	1.1	15.8	54.8	223,000	5.9
NGC 6355	359.5	5.4	9.2	1.4	31.6	77.5	252,000	N/A
Terzan 2	356.3	2.3	7.5	0.8	24.0	none	3,290	N/A
Terzan 4	356.0	1.3	7.2	1.0	23.3	none	N/A	N/A
HP 1	357.4	2.1	8.2	0.5	20.4	none	95,700	N/A
Liller 1	354.8	-0.1	8.2	0.8	36.5	9.9	289,000	N/A
Terzan 1	357.5	1.0	6.7	1.3	22.8	77.5	5,360	N/A
Ton 2	350.8	-3.4	8.2	1.4	25.3	none	7,330	N/A
Terzan 5	3.8	1.6	6.9	1.2	21.9	11.6	374,000	N/A
NGC 6440	7.7	3.8	8.5	1.3	13.0	9.8	811,000	N/A
Terzan 6	358.5	-2.1	6.8	1.3	43.6	7.3	300,000	N/A
UKS 1	5.1	0.7	7.8	0.7	45.6	54.8	145,000	N/A
Terzan 9	3.6	-1.9	7.1	1.1	21.3	17.0	9,570	N/A
NGC 6522	1.0	-3.9	7.7	0.6	34.8	54.8	300,000	6.7
NGC 6528	1.1	-4.1	7.9	0.6	33.1	54.8	152,000	N/A
NGC 6558	0.2	-6.0	7.4	1.0	28.5	63.3	98,400	3.1
NGC 6624	2.7	-7.9	7.9	1.2	47.4	16.0	257,000	5.4

Table 4.2: Parameters for Bulge Globular Clusters. D_{GC} is the distance from the Galactic center and D is the distance from the Sun to the Globular cluster.

moderate birth velocity kick and the core relaxation time for each GC is an order of magnitude less than the characteristic age of the pulsars that hosts them allowing enough time for them to settle into the core which is where 3 of the 4 pulsars are found. The fourth, PSR B1718–19, has a characteristic age about equal to NGC 6342’s relaxation time and this could explain why PSR B1718–19 is not located in the host GC’s core. This could also explain why these young pulsars are towards the higher end of the age distribution for non-recycled pulsars. The metallicity of the Galactic center is higher than that of the Galactic disk and stars migrating from the bulge to bulge GCs could explain why GCs with young pulsars have higher metallicities compared to the overall GC population.

The population of bulge pulsars is relatively unexplored. Outside of Galactic center surveys (Deneva et al, 2009; Johnston et al, 2006; Klein et al, 2004; & Kramer et al, 2000) and the surveys of bulge GCs (Table 4.3), the population is unknown. The most sensitive published survey to explore this region is the Parkes Multi-beam survey (Manchester et al, 2001). For pulsars with a period of 100-1000 ms the survey has a limiting flux of 0.16 mJy and this translates into a L_{\min} of 7.8 mJykpc² for a distance of 7.0 kpc (front edge of bulge) and 12 mJykpc² for a distance of 8.6 kpc (top and bottom of bulge directly above and below Galactic center). These L_{\min} values represent the upper edge of the pulsar luminosity function presented in FK06 and show that the Galactic bulge has not been surveyed well enough to constrain its pulsar population especially considering DM smearing and scattering would further hinder the detection of these pulsars.

Another chance for pulsars to be captured will occur when the GC passes through the plane of the Galaxy as it orbits the Galactic center. The orbital timescales for globular clusters around the galaxy are hundreds of Myrs and this is longer than the 43 Myr average lifetime of a normal pulsar. This means that any pulsars picked up would have to have been picked up on the most recent pass of the GC through the Galactic disk. Figure 4.1 shows a small population of pulsars that would live long enough to be found in a GC if capture occurred due to this scenario.

The plausibility of star capture by a GC is discussed in Mieske & Baumgardt (2007; henceforth MB07) and their arguments will be applied here in the following discussions. Table 4.6.4.2 lists all GCs within 1.5 kpc of the Galactic center and their characteristics relevant to the MB07 analysis. MB07 found that the capture prob-

ability decreases with increasing number of cluster particles (N_{GC}) and decreases with increasing initial velocity over cluster velocity dispersion ratio ($\frac{V_{\text{int}}}{\sigma_{\text{GC}}}$). Assuming an average particle mass of $0.5 M_{\odot}$, the range of clusters reviewed matches with the range of Galactic bulge clusters, however the range of $\frac{V_{\text{int}}}{\sigma_{\text{GC}}}$ do not. GC velocity dispersions range from $\sim 1.0 - 19 \text{ km s}^{-1}$, which are an order of magnitude less than typical pulsar velocities in previous studies (see Hobbs et al. 2005, for a recent study). The closest scenario of $\frac{V_{\text{int}}}{\sigma_{\text{GC}}}$ equal to unity will be the only one considered from here.

To obtain a comparison of capture rates between pulsars and MB07, a few other considerations need to be put into place. Using the FK06 model for the Galactic pulsar population, the mass density of pulsars is found to be $8.2 \times 10^{-6} M_{\odot} \text{ pc}^{-3}$ for the Galactic bulge assuming a uniform pulsar per mass distribution throughout the Galaxy. This value is five orders of magnitude less than the value of $0.25 M_{\odot} \text{ pc}^{-3}$ used in MB07. Even if the entire pulsar population were placed inside the Galactic bulge, this would increase the mass density by only an order of magnitude. The resulting differences in mass density would produce significantly lower values for the rates found by MB07. The value of 265 km s^{-1} will be adopted as the velocity dispersion for field pulsars (σ_{field}). For a σ_{field} of 200 km s^{-1} MB07 concludes that no stars will be captured in any mass cluster within a Hubble time. If the additional constraints for pulsars of lower capture probability due to higher initial velocities and lower capture rates due to lower mass density are included, the conclusion can be drawn that no pulsars are likely to be captured by a GC. Imposing further constraints of beaming, luminosity limits, and finite radio-loud lifetimes for

pulsars would further hinder the detection of a pulsar if one were to be captured by a GC. We therefore rule out this possibility as an origin for the young pulsars in GCs.

4.6.5 Suggested Future Work

All the work presented here only provides a statistical study at the young pulsar population in GCs and neglects the dynamics and history of each GC. Clearly N-body simulations similar to those presented in Ivanova et al. (2008) of the GCs and their possible interactions with the Galactic stellar and post-stellar populations would place better constraints on the values presented here and would further the understanding of GC's dynamics and evolutionary history.

To improve upon the observational constraints used in this work, it is clearly desirable to search all GCs as deeply as possible using existing facilities. We highlight here some GCs of particular interest.

There are a few exceptions, most notably NGC 6342 which has the highest minimum detectable flux density of any of the 97 GCs and has not to our knowledge been surveyed since the discovery of B1718–19 by Lyne et al. (1993). A new search with the currently available telescopes could reduce the S_{\min} by a factor of 10 and provide evidence for or against PSR B1718–19 association with NGC 6342 (Bailes et al. 2005, Freire 2005).

Another high metallicity bulge GC to be searched is NGC 6637 (M 69). This cluster, at a distance of 8.8 kpc, also has a high two-body encounter rate, Γ . This

parameter is often used to assess the plausibility of pulsar content in GCs (see, e.g., Hui et al. 2010).

Most of the GCs presented in this work have been searched to the sensitivity limit of the telescope for which they are visible. The next generation of radio telescopes will be needed to present better constraints on this work. The Square Kilometer Array (SKA) would be an ideal telescope to accomplish this task. The SKA would provide over a factor of one hundred increase in telescope gain over the GBT, Parkes, and Jodrell Bank telescopes and over a factor of thirty in telescope gain over Arecibo. This improvement in gain alone would allow for deep searches, with luminosity limits less than the mean in the Faucher-Giguère & Kaspi (2006) model, in only an hour or two for GCs less than twenty kpc away (see Smits et al, 2009 for pulsar work with the SKA). Before the advent of the SKA, MeerKAT, the South African SKA precursor, will be able to reduce these minimum detectable flux density limit by a factor of 10 when completed (Booth et al, 2009).

Acknowledgments

This work was supported by NSF grant AST-0907967 and a WVEPSCoR Research Challenge Grant. We would like to thank the scientific editor and anonymous referee for their help and comments during the submission process.

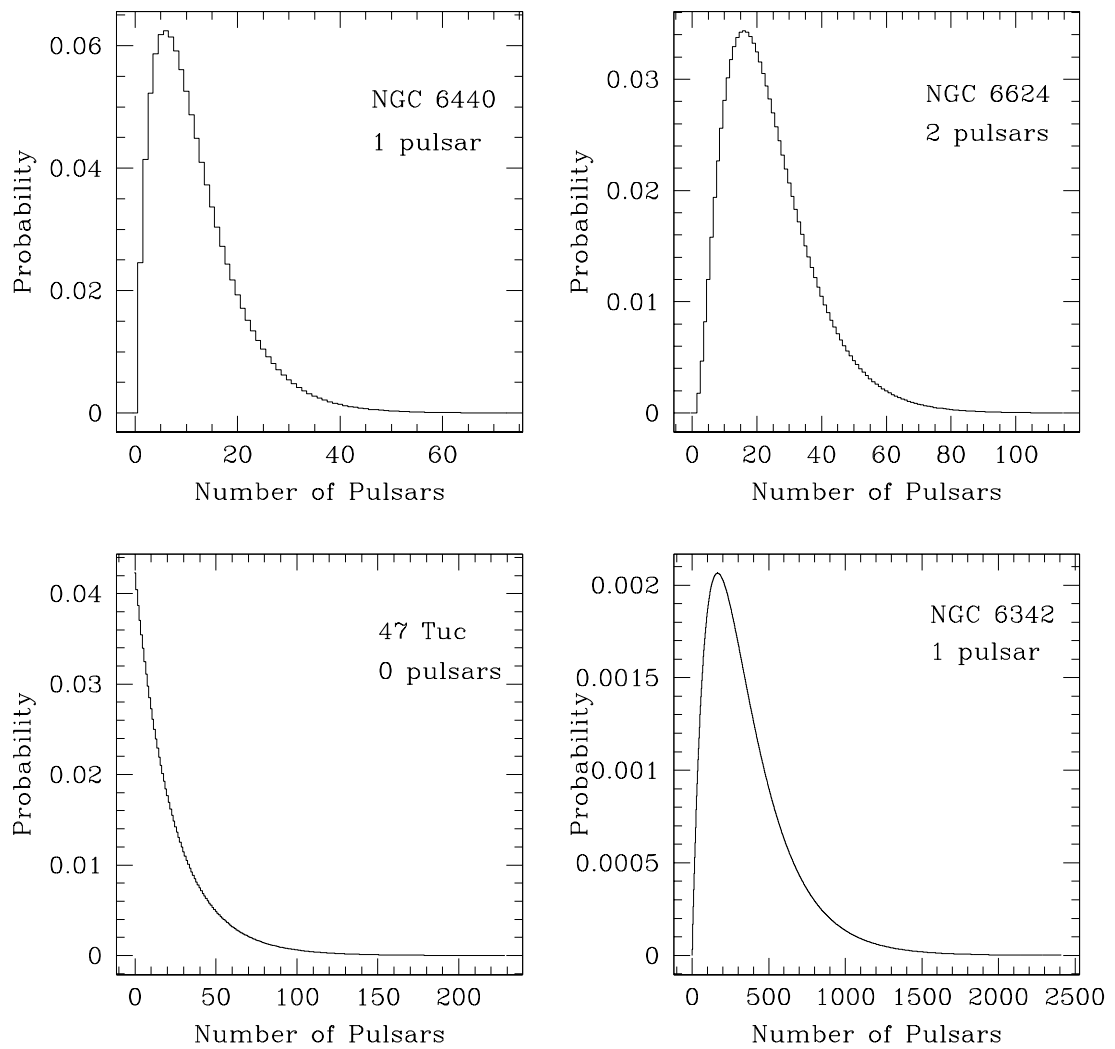


Figure 4.2: Examples of discrete posterior probability density functions for the number of potentially observable pulsars in GCs using the Bayesian analysis.

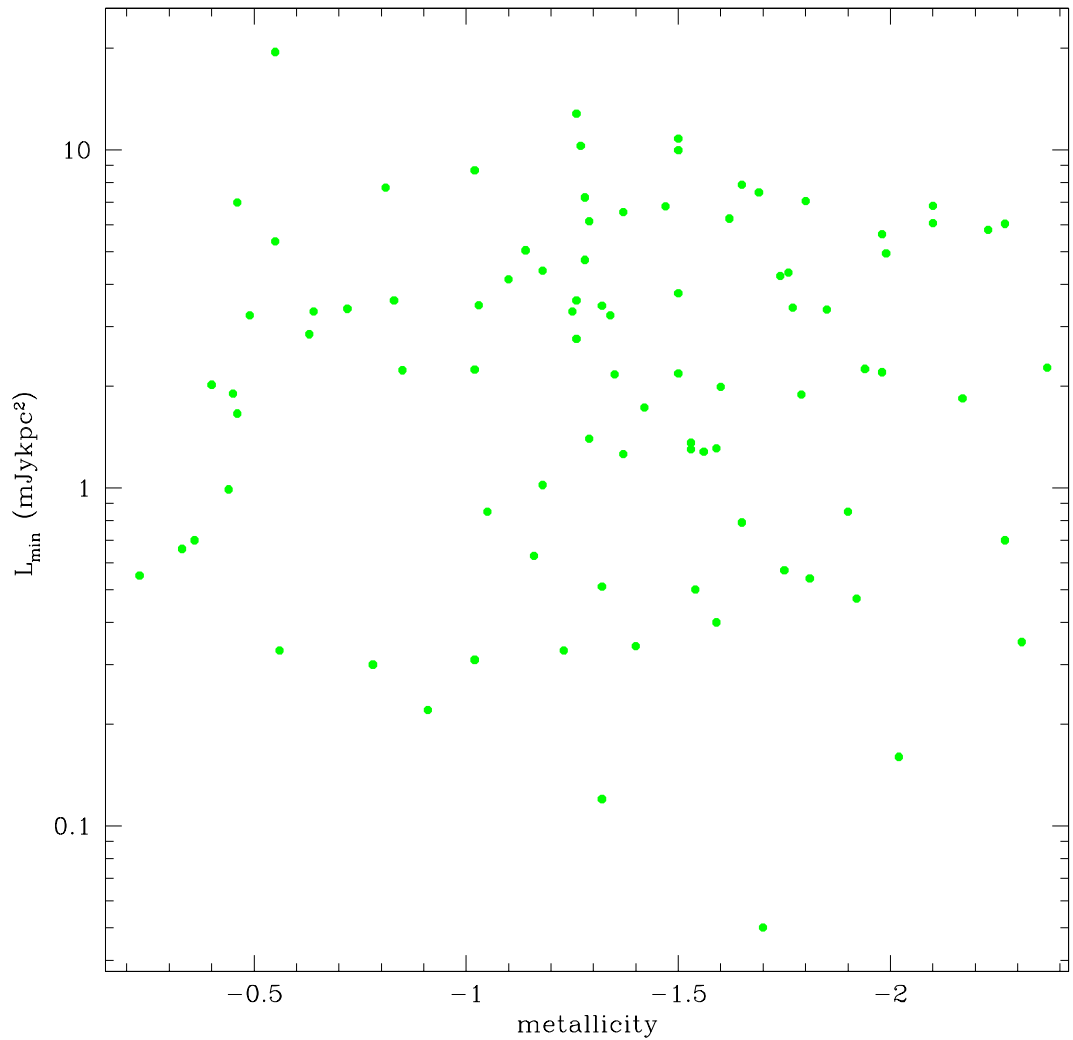


Figure 4.3: 1400 MHz luminosity survey limits as a function of metallicity with six GCs excluded with distances greater than 20 kpc. The luminosities are randomly distributed and show no bias against low or high metallicity GCs.

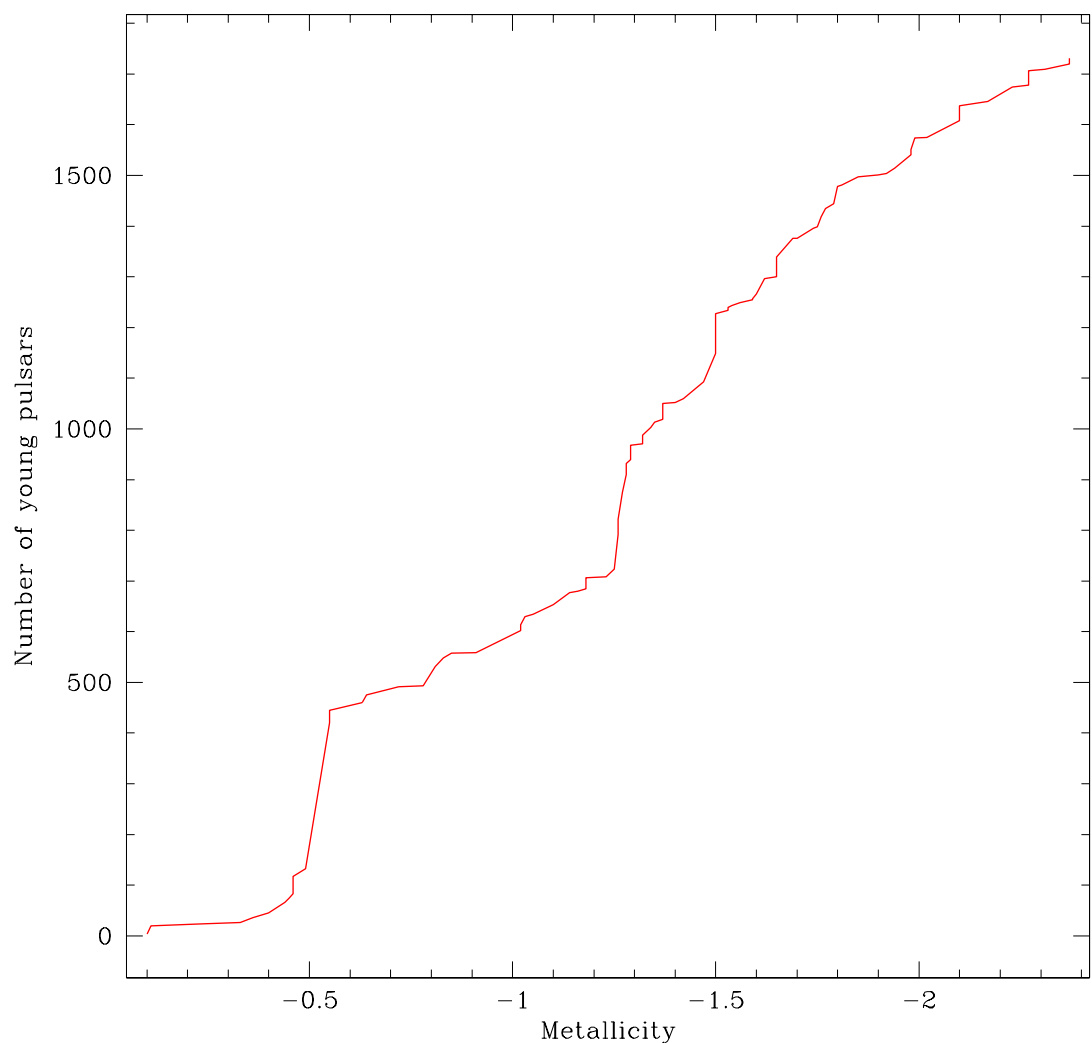


Figure 4.4: CDF of young pulsars predicted by the binomial analysis as a function of metallicity.

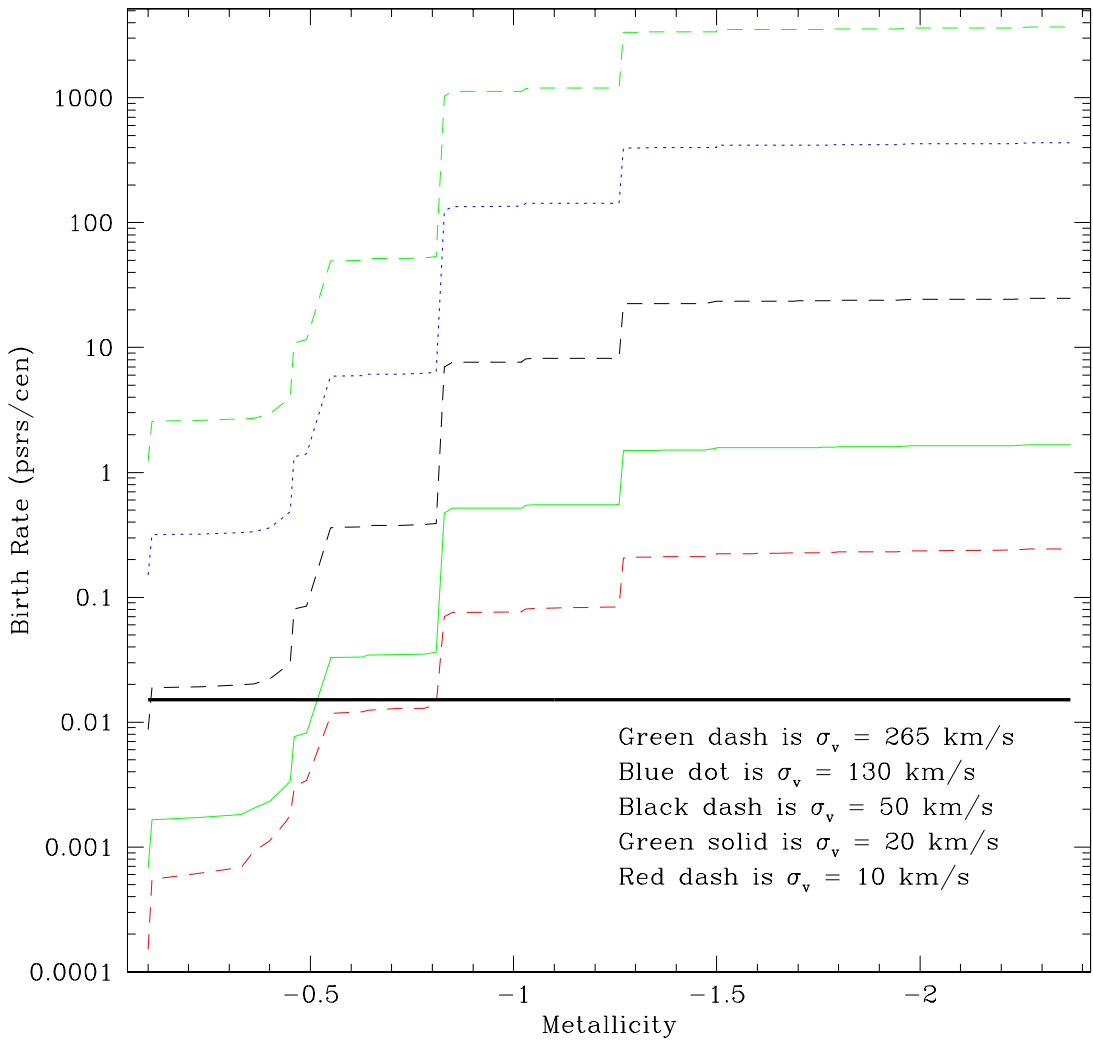


Figure 4.5: CDF of birth rate versus metallicity.

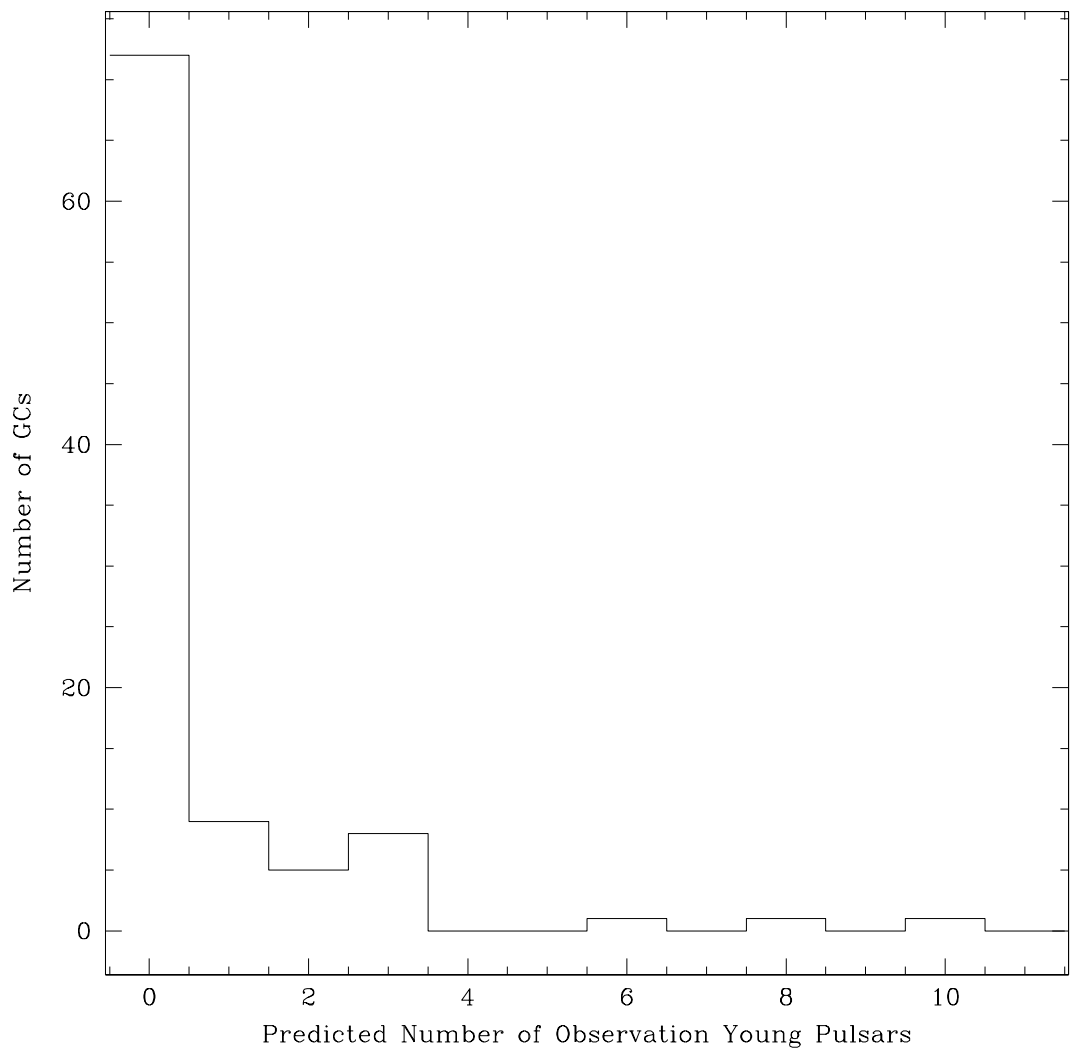


Figure 4.6: Histogram of number of predicted observable young pulsars per Globular Cluster using a model only dependent on the mass of the GC.

Table 4.3: Parameters for globular clusters searched for pulsars. GC parameters from Harris (1996).

Globular Cluster	Dist. (kpc)	S_{min} (1400) (μJy)	V_{esc} (km s^{-1})	Metallicity log[Fe/H]	Mass M_\odot	Number of Young Pulsars	Search Reference
47 Tuc	4.5	167.6	68.8	-0.72	1,500,000	0	Freire et al 2001
NGC 288	8.9	6.5	13.3	-1.32	112,000	0	Lynch & Ransom 2011
NGC 1261	16.3	38.8	3.4	-1.27	341,000	0	Possenti unpublished 2010
Pal 2	27.2	34	27.8	-1.42	410,000	0	Hessels et al 2007
NGC 1851	12.1	30.1	51.8	-1.18	551,000	0	Freire et al 2004
NGC 2298	10.8	4.1	18.4	-1.92	84,900	0	Lynch & Ransom 2011
NGC 2808	9.6	54.8	72.8	-1.14	1,420,000	0	Possenti unpublished 2010
E3	8.1	54.8	3.0	-0.83	3,290	0	Possenti unpublished 2010
NGC 3201	4.9	54.8	22.0	-1.59	254,000	0	Possenti unpublished 2010
NGC 4147	19.3	19	18.3	-1.80	74,700	0	Hessels et al 2007
NGC 4372	5.8	54.8	21.5	-2.17	329,000	0	Possenti unpublished 2010
NGC 4590	10.3	54.8	18.2	-2.23	223,000	0	Possenti unpublished 2010
NGC 4833	6.6	77.5	31.8	-1.85	410,000	0	Possenti unpublished 2010
NGC 5024	17.9	19	33.4	-2.10	826,000	0	Hessels et al 2007
NGC 5053	17.4	20	8.9	-2.27	125,000	0	Hessels et al 2007
NGC 5139	5.2	48.3	60.4	-1.53	3,350,000	0	Possenti unpublished 2010
NGC 5272	10.2	21	37.2	-1.50	957,000	0	Hessels et al 2007
NGC 5286	11.7	54.8	52.6	-1.69	713,000	0	Possenti unpublished 2010
NGC 5466	16.0	22	9.5	-1.98	179,000	0	Hessels et al 2007
Pal 5	23.2	32	3.2	-1.41	30,000	0	Hessels et al 2007
NGC 5897	12.5	5.5	13.4	-1.90	211,000	0	Lynch & Ransom 2011
NGC 5904	7.5	25	47.7	-1.29	857,000	0	Hessels et al 2007
NGC 5927	7.7	54.8	33.9	-0.49	338,000	0	Possenti unpublished 2010
NGC 5946	10.6	54.8	25.3	-1.29	281,000	0	Possenti unpublished 2010
NGC 5986	10.4	3.7	37.0	-1.59	599,000	0	Lynch & Ransom 2011
M 80	10.0	5.7	48.7	-1.75	502,000	0	Lynch et al 2011
NGC 6121	2.2	131.4	34.2	-1.16	195,000	0	Lyne et al 1988
ESO452	8.3	54.8	5.9	-1.50	75,000	0	Possenti unpublished 2010
NGC 6144	8.9	54.8	14.1	-1.76	169,000	0	Possenti unpublished 2010
NGC 6139	10.1	77.5	59	-1.65	566,000	0	Possenti unpublished 2010
NGC 6171	6.4	54.8	25	-1.02	182,000	0	Possenti unpublished 2010
NGC 6205	7.1	27	39.1	-1.53	775,000	0	Hessels et al 2007
NGC 6218	4.8	54.8	28.5	-1.37	217,000	0	Possenti unpublished 2010
NGC 6235	11.5	54.8	16.8	-1.28	73,300	0	Possenti unpublished 2010
NGC 6254	4.4	66.6	29.5	-1.56	252,000	0	Possenti unpublished 2010
Pal 15	45.1	38	4.3	-2.07	40,300	0	Hessels et al 2007
NGC 6266	6.8	22.1	97.8	-1.18	1,220,000	0	Chandler 2003
NGC 6273	8.8	54.8	58.4	-1.74	1,100,000	0	Possenti unpublished 2010
NGC 6284	15.3	54.8	28.6	-1.26	361,000	0	Possenti unpublished 2010
NGC 6287	9.4	77.5	30.4	-2.10	188,000	0	Possenti unpublished 2010
NGC 6293	9.5	54.8	41.7	-1.99	329,000	0	Possenti unpublished 2010
NGC 6304	5.9	54.8	38.4	-0.45	217,000	0	Possenti unpublished 2010
M 92	8.3	5.1	47.1	-2.31	489,000	0	Lynch & Ransom 2011
NGC 6325	7.8	54.8	42.5	-1.25	223,000	0	Possenti unpublished 2010
NGC 6333	7.9	54.8	37.7	-1.77	422,000	0	Possenti unpublished 2010
NGC 6342	8.5	270	22.9	-0.55	96,600	1	Biggs & Lyne 1996
NGC 6355	9.2	77.5	40.3	-1.37	252,000	0	Possenti unpublished 2010
Liller 1	8.2	9.9	41.2	-0.33	289,000	0	Lynch et al 2011
Ter 1	6.7	77.5	7.4	-1.03	5,360	0	Possenti unpublished 2010
NGC 6388	9.9	54.8	124	-0.55	2,170,000	0	Possenti unpublished 2010
NGC 6402	9.3	54.8	39.1	-1.28	1,040,000	0	Possenti unpublished 2010
NGC 6401	10.6	77.5	38.3	-1.02	286,000	0	Possenti unpublished 2010
NGC 6397	2.3	31.5	48.3	-2.02	115,000	0	Possenti unpublished 2010
Pal 6	5.8	6.7	28.0	-0.91	228,000	0	Lynch et al 2011
NGC 6426	20.6	25	14.7	-2.15	117,000	0	Hessels et al 2007
Ter 5	6.9	11.6	50.5	-0.23	374,000	0	Ransom et al 2005
NGC 6440	8.5	9.8	85.2	-0.36	811,000	1	Freire et al 2008
NGC 6441	11.6	12.4	102	-0.46	1,570,000	0	Freire et al 2008
Ter 6	6.8	7.3	38.3	-0.56	300,000	0	Lynch et al 2011
NGC 6453	11.6	80.4	22.4	-1.50	169,000	0	Possenti unpublished 2010
UKS 1	7.8	54.8	25.4	-0.64	145,000	0	Possenti unpublished 2010
NGC 6496	11.3	54.8	19.7	-0.46	200,000	0	Possenti unpublished 2010
Ter 9	7.1	17.0	9.8	-1.05	9,570	0	Lynch & Ransom 2011
NGC 6517	10.6	3.0	82.9	-1.23	526,000	0	Lynch et al 2011
NGC 6522	7.7	54.8	42.3	-1.34	300,000	0	Possenti unpublished 2010
NGC 6528	7.9	54.8	26.4	-0.11	152,000	0	Possenti unpublished 2010
NGC 6535	6.8	41	10.0	-1.79	20,000	0	Hessels et al 2007
NGC 6539	7.8	47.0	35.8	-0.63	536,000	0	D' Amico et al 1993

Table 4.3: Continued

Globular Cluster	Dist. (kpc)	S_{min} (1400) (μJy)	V_{esc} (km s^{-1})	Metallicity log[Fe/H]	Mass M_\odot	Number of Young Pulsars	Search Reference
NGC 6540	5.3	77.5	27.6	-1.35	36,400	0	Possenti unpublished 2010
NGC 6544	3.0	38.8	93.5	-1.40	108,000	0	Possenti unpublished 2010
NGC 6541	7.5	9.6	42.2	-1.81	572,000	0	Lynch unpublished 2010
NGC 6558	7.4	63.3	32.1	-1.32	98,400	0	Possenti unpublished 2010
NGC 6584	13.5	54.8	24.3	-1.50	303,000	0	Possenti unpublished 2010
NGC 6624	7.9	16.0	35.3	-0.44	257,000	2	Lynch et al 2011
M 28	5.5	4.1	63.8	-1.32	551,000	0	Lynch unpublished 2010
NGC 6642	8.1	54.8	30.7	-1.26	109,000	0	Possenti unpublished 2010
NGC 6652	10.0	77.5	37.5	-0.81	109,000	0	Possenti unpublished 2010
M 22	3.2	5.7	44.7	-1.70	644,000	0	Lynch et al 2011
NGC 6681	9.0	77.5	39.3	-1.62	179,000	0	Possenti unpublished 2010
NGC 6712	6.9	6.7	27.7	-1.02	257,000	0	Lynch et al 2011
NGC 6717	7.1	54.8	21.6	-1.26	47,500	0	Possenti unpublished 2010
NGC 6723	8.7	54.8	27.3	-1.10	357,000	0	Possenti unpublished 2010
NGC 6749	7.9	32	20.4	-1.60	123,000	0	Hessels et al 2007
NGC 6752	4.0	31.5	32.9	-1.54	317,000	0	Possenti unpublished 2010
NGC 6760	7.4	37	40.1	-0.40	357,000	0	Hessels et al 2007
NGC 6779	9.4	25	28.7	-1.98	230,000	0	Hessels et al 2007
Pal 10	5.9	23	17.2	-0.10	53,100	0	Hessels et al 2007
NGC 6809	5.4	77.5	19.7	-1.94	269,000	0	Possenti unpublished 2010
NGC 6838	4.0	19	16.7	-0.78	43,000	0	Hessels et al 2007
NGC 6934	15.6	28	28.1	-1.47	295,000	0	Hessels et al 2007
NGC 6981	17.0	6.0	16.6	-1.42	168,000	0	Lynch & Ransom 2011
NGC 7006	41.2	19	19.8	-1.52	303,000	0	Hessels et al 2007
NGC 7078	10.4	21	62.1	-2.37	1,190,000	0	Hessels et al 2007
NGC 7089	11.5	6.0	48.1	-1.65	104,000	0	Lynch & Ransom 2011
NGC 7099	8.1	10.8	34.1	-2.27	241,000	0	Ransom et al 2004
Pal 12	19.0	6.2	5.5	-0.85	15,900	0	Lynch & Ransom 2011
Pal 13	26.0	21	3.5	-1.88	6,500	0	Hessels et al 2007

Table 4.4: Binomial analysis of young pulsars in globular clusters.

Globular Cluster	Median	2.5 th percentile	97.5 th percentile	$\log(f_{R1})$ 50 km s ⁻¹	$\log(f_{R3})$ 10 km s ⁻¹	$\log(\mathcal{R})f_{R1}$ (psrs cen ⁻¹)	$\log(\mathcal{R})f_{R3}$ (psrs cen ⁻¹)	N _{predicted} mass model
47 Tuc	16	0	88	-0.39	0.00	-3.04	-3.43	1
NGC 288	3	0	17	-2.30	-0.42	-1.85	-3.74	0
NGC 1261	53	1	297	-4.08	-1.99	1.15	-0.92	0
Pal 2	167	6	968	-1.37	-0.02	-1.03	-2.40	0
NGC 1851	21	0	115	-0.66	0.00	-2.65	-3.32	0
NGC 2298	3	0	16	-1.89	-0.17	-2.26	-3.99	3
NGC 2808	24	0	133	-0.34	0.00	-2.92	-3.26	0
E3	17	0	93	-4.24	-2.15	0.82	-1.25	0
NGC 3201	6	0	36	-1.66	-0.08	-2.19	-3.77	0
NGC 4147	34	1	192	-1.90	-0.17	-1.20	-2.93	0
NGC 4372	9	0	49	-1.70	-0.09	-1.99	-3.59	0
NGC 4590	28	1	155	-1.90	-0.18	-1.28	-3.01	0
NGC 4833	16	0	87	-1.21	0.00	-2.22	-3.43	0
NGC 5024	29	1	163	-1.15	0.00	-2.02	-3.17	0
NGC 5053	29	1	162	-2.83	-0.82	-0.35	-2.35	0
NGC 5139	6	0	36	-0.50	0.00	-3.35	-3.86	8
NGC 5272	10	0	57	-1.03	0.00	-2.61	-3.64	1
NGC 5286	37	1	205	-0.64	0.00	-2.42	-3.07	0
NGC 5466	27	0	149	-2.74	-0.75	-0.46	-2.45	0
Pal 5	101	3	575	-4.16	-2.07	1.51	-0.56	0
NGC 5897	4	0	25	-2.30	-0.41	-1.73	-3.62	0
NGC 5904	7	0	39	-0.75	0.00	-3.04	-3.80	2
NGC 5927	15	0	84	-1.13	0.00	-2.32	-3.46	0
NGC 5946	29	1	164	-1.49	-0.03	-1.68	-3.13	0
NGC 5986	2	0	14	-1.03	0.00	-3.30	-4.34	3
M 80	3	0	19	-0.73	0.00	-3.43	-4.16	6
NGC 6121	3	0	20	-1.13	0.00	-3.03	-4.16	0
ESO452	17	0	98	-3.36	-1.30	-0.04	-2.10	0
NGC 6144	20	0	113	-2.23	-0.36	-1.10	-2.97	0
NGC 6139	39	1	218	-0.53	0.00	-2.51	-3.05	0
NGC 6171	10	0	59	-1.50	-0.04	-2.13	-3.60	0
NGC 6205	7	0	37	-0.97	0.00	-2.82	-3.80	1
NGC 6218	6	0	35	-1.34	-0.01	-2.51	-3.84	0
NGC 6235	35	1	197	-2.01	-0.23	-1.08	-2.86	0
NGC 6254	6	0	36	-1.30	-0.01	-2.55	-3.85	0
Pal 15	878	30	5409	-3.77	-1.70	2.07	0.00	0
NGC 6266	5	0	29	-0.13	0.00	-3.80	-3.94	3
NGC 6273	20	0	110	-0.54	0.00	-2.80	-3.34	0
NGC 6284	69	2	391	-1.34	-0.01	-1.46	-2.78	0
NGC 6287	33	1	185	-1.26	0.00	-1.85	-3.11	0
NGC 6293	23	0	130	-0.90	0.00	-2.38	-3.28	0
NGC 6304	9	0	51	-0.99	0.00	-2.69	-3.69	0
M 92	2	0	13	-0.76	0.00	-3.57	-4.34	2
NGC 6325	15	0	86	-0.87	0.00	-2.58	-3.46	0
NGC 6333	16	0	88	-1.01	0.00	-2.42	-3.43	0
NGC 6342	288	40	1047	-1.61	-0.06	-0.56	-2.11	0
NGC 6355	31	1	176	-0.93	0.00	-2.21	-3.15	0
Liller 1	3	0	21	-0.91	0.00	-3.25	-4.16	0
Ter 1	16	0	90	-3.06	-1.03	-0.36	-2.40	0
NGC 6388	25	0	142	-0.04	0.00	-3.20	-3.24	1
NGC 6402	22	0	124	-0.97	0.00	-2.32	-3.30	0
NGC 6401	43	1	244	-0.99	0.00	-2.01	-3.00	0
NGC 6397	1	0	8	-0.73	0.00	-3.90	-4.64	1
Pal 6	1	0	10	-1.36	-0.02	-3.27	-4.62	2
NGC 6426	55	1	308	-2.18	-0.33	-0.72	-2.56	0
Ter 5	3	0	18	-0.69	0.00	-3.47	-4.16	2
NGC 6440	10	2	34	-0.22	0.00	-3.41	-3.64	3
NGC 6441	8	0	45	-0.12	0.00	-3.62	-3.74	3
Ter 6	2	0	13	-0.99	0.00	-3.34	-4.34	1
NGC 6453	56	2	316	-1.64	-0.07	-1.24	-2.81	0
UKS 1	15	0	86	-1.49	-0.03	-1.97	-3.42	0
NGC 6496	34	1	189	-1.80	-0.13	-1.30	-2.97	0
Ter 9	4	0	25	-2.70	-0.72	-1.33	-3.32	0
NGC 6517	2	0	13	-0.24	0.00	-4.10	-4.34	3
NGC 6522	15	0	84	-0.88	0.00	-2.58	-3.46	0
NGC 6528	16	0	88	-1.44	-0.03	-1.99	-3.40	0
NGC 6535	9	0	50	-2.67	-0.70	-1.01	-2.98	0
NGC 6539	13	0	74	-1.07	0.00	-2.45	-3.53	0
NGC 6540	10	0	57	-1.38	-0.02	-2.25	-3.62	0
NGC 6544	2	0	13	-0.16	0.00	-4.17	-4.34	0
NGC 6541	3	0	18	-0.88	0.00	-3.28	-4.16	3
NGC 6558	16	0	90	-1.20	0.00	-2.23	-3.43	0
NGC 6584	51	1	287	-1.54	-0.05	-1.39	-2.88	0
NGC 6624	21	5	58	-1.09	0.00	-2.23	-3.32	0
M28	1	0	7	-0.45	0.00	-4.18	-4.64	10
NGC 6642	17	0	93	-1.25	0.00	-2.15	-3.40	0
NGC 6652	38	1	213	-1.02	0.00	-2.04	-3.06	0
M 22	0	0	4	-0.82	0.00	-1.74 ^a	-4.64 ^a	0
NGC 6681	30	1	168	-0.96	0.00	-2.20	-3.16	0
NGC 6712	2	0	12	-1.38	-0.02	-2.96	-4.32	1
NGC 6717	13	0	72	-1.69	-0.09	-1.83	-3.43	0
NGC 6723	19	0	108	-1.40	-0.02	-1.96	-3.33	0
NGC 6749	9	0	53	-1.76	-0.12	-1.92	-3.56	0
NGC 6752	3	0	17	-1.17	0.00	-2.99	-4.16	1
NGC 6760	9	0	53	-0.94	0.00	-2.74	-3.69	0
NGC 6779	10	0	58	-1.33	-0.01	-2.30	-3.62	0
Pal 10	4	0	24	-1.98	-0.21	-2.06	-3.82	0

Table 4.4: Continued

Globular Cluster	Median	2.5^{th} percentile	97.5^{th} percentile	$\log(f_{R1})$ 50 km s^{-1}	$\log(f_{R3})$ 10 km s^{-1}	$\log(\mathcal{R})f_{R1}$ (psrs cen^{-1})	$\log(\mathcal{R})f_{R3}$ (psrs cen^{-1})	$N_{\text{predicted mass model}}$
NGC 6809	10	0	59	-1.80	-0.13	-1.83	-3.50	0
NGC 6838	2	0	12	-2.01	-0.23	-2.32	-4.10	0
NGC 6934	33	1	184	-1.36	-0.01	-1.75	-3.10	0
NGC 6981	8	0	46	-2.02	-0.24	-1.71	-3.49	0
NGC 7006	237	8	1384	-1.80	-0.13	-0.46	-2.13	0
NGC 7078	11	0	60	-0.48	0.00	-3.11	-3.60	2
NGC 7089	4	0	24	-0.74	0.00	-3.30	-4.04	3
NGC 7099	4	0	22	-1.13	0.00	-2.90	-4.03	1
Pal 12	10	0	59	-3.45	-1.39	-0.18	-2.25	0
Pal 13	79	2	446	-4.04	-1.96	1.29	-0.78	0

^a Values are upper limits assuming M22 contains one pulsar.

f_R is the retention fraction for a given velocity dispersion.

\mathcal{R} is the birthrate in pulsars per century for the median value.

Birthrates are upper limits for a given globular cluster except for those with detected young pulsars.

Chapter 5

Conclusions and Future Work

5.1 Green Bank 350-MHz surveys

In chapter 2 we explored the pulsar population at a radio frequency of 350-MHz. So far this survey has resulted in the discovery of twenty-six new pulsars and many redetected pulsars up to a DM of 307 pc cm^{-3} . Among these 26, there are six binary systems, five millisecond pulsars, two partially recycled pulsars, and one rotating radio transient. The periods of these new sources range from 1.69 millisecond to 5.023 seconds covering the whole range of pulsar periods, but due to interstellar medium effects, the DM range only covered from 3.27 to 66.98 pc cm^{-3} . The discoveries from this survey have led to a wealth of multi-wavelength observations

In the high energy region, two of these sources, PSR J1023+0038 and PSR J2256–1022 were detected with FERMI Gamma-ray satellite and both show pulsations. At least three sources, PSR J1023+0038, PSR J2256–1022, and PSR J2222–0137, have X-ray detected counterparts and PSR J1023+0038 shows pulsations in the X-ray. Optical companions have been detected for PSR J1023+0038 and J0348+0432 but none has been found for PSR J2222–0137, though it is the closest pulsar found in this survey. VLBA could provide distances to many of these sources, but usually only sources of interest have VLBA observation conducted with them.

This includes PSR J1023+0038 with an distance of 1.6 kpc and PSR J2222–0137 with a distance of 250 pc. Masses of two pulsars, PSR J1023+0038 with a mass of $1.67 M_{\odot}$ and PSR J2222–0137 with a mass of $1.49 M_{\odot}$, have been measured, both using different techniques.

The optical limit of 24.5 mags and the current parallax measurement suggests that PSR J2222–0137 and its companion are a double neutron star system. If confirmed, this would make it the closest, least eccentric double neutron system known, with an eccentricity two orders of magnitude lower than any previously measured for a double neutron star system. Searches across many radio frequencies have been undertaken with no detection of the companion as a pulsar.

The GBT 350-MHz drift-scan pulsar survey was primer for the new Green Bank North celestial Cap (GBNCC) survey. The GBNCC takes advantage of the newest Green Bank pulsar instrument called the Green Bank Ultimate Pulsar Instrument (GUPPI; Ransom et al 2009). The survey will cover all the sky visible from the Green Bank and so far has found more than ten new pulsars including one, J0645+51, already added to existing pulsar timing arrays.

Such a large survey would allow the luminosity function for pulsars at low frequencies to be explored. Similar modeling has been done with the Parkes Multi-beam Pulsar Survey (PMPS) and is widely used for examining the pulsar population (Faucher-Giguère & Kaspi 2006; Ridley & Lorimer 2010). These works are focused at 1400 MHz and require scaling to be used for population modeling at other frequencies. Such scaling may provide incorrect numbers of pulsars due to the exclusion of steep spectral index pulsars that may only observable at lower frequencies and

pulsars with gigahertz-peaked spectral turnovers (Kijak et al 2011). Although a number of low-frequency pulsar surveys have been carried out over the years, the non-uniformities in sensitivity make it difficult to model this effect currently. The GBNCC will be an excellent survey to explore the frequency evolution of the pulsar luminosity function at lower frequencies.

5.2 Rotating Radio Transients

In chapter 3 we took a look at a small population of the rotating radio transients. Here we obtained five timing solutions and looked at properties of each rotating radio transient to determine where or how they fit into the population of neutron stars. Some of these sources are like normal pulsars, just here emissions shows a greater range of single pulse fluxes then what is seen in most pulsars. Others are truly erratic and the pulsar model needs to explain the exotic behavior such as pulsars that spend most of their time not emitting in the radio.

So far only about thirty percent of the known RRATs have timing solutions. Further work needs to be done in obtaining more solutions to characterize the population. Along with this, full Stokes observations should occur to measure other properties of the RRATs emission. Lastly more of this sporadic population needs and will be found in survey across the pulsar radio spectrum.

5.3 Globular Cluster Pulsars

In chapter 4 we looked at the unusual population of long period pulsars in Galactic globular clusters. Three globular clusters contain four of these objects. Using Bayesian statistics and luminosity limits, we inferred a possible population of long period pulsars and constructed a possible birthrate to examine sources for this population. The collapse of a O-Ne-Mg white dwarf was determined to be the most likely creation mechanism for these neutron stars. Also noted was that these pulsars were hosted by globular clusters that had high iron metallicity, possibly providing a link between core collapse supernovae and the metallicity of the host globular clusters.

Most globular cluster have been searched to the sensitivity limit available for telescopes that can observe them. A few exceptions exist like NGC 6342 that have very large flux density limits and could easily be improved with the newest generation of instruments. Along with clusters not searched that deeply, there are a few like NGC 6637 that have favorable cluster properties and may contain pulsars both normal and recycled. Further theoretical work also need to be done to better understand core collapse supernovae and the effects they could have on the stellar environment of globular clusters.

5.4 Next Generation Radio Telescopes

All the projects undertaken in this work would benefit from the next generation of telescopes. In the long term the square kilometer array (SKA) will be the

ultimate instrument for all radio studies in its frequency bands. The SKA is only in the design stage, so the next telescopes will be SKA precursor like MeerKAT or new interferometeries like LOFAR will allow for greater sensitivity then the current generation of telescopes.

Bibliography

- Anderson, P. W., & Itoh, N. 1975, Nature, 256, 25
- Anderson, 1992 *Ph.D. Thesis*, Cal Tech
- Archibald, A. M., et al. 2009, Science, 324, 1411
- Baade, W., & Zwicky, F. 1934, Proceedings of the National Academy of Science, 20, 254
- Backer, D. C., Kulkarni, S. R., Heiles, C., Davis, M. M., & Goss, W. M. 1982, Nature, 300, 615
- Backer, D. C., Foster, R. S., & Sallmen, S. 1993, Nature, 365, 817
- Bailes, M., Zhu, J., & Richter, S. 2005, Binary Radio Pulsars, 328, 195
- Bhat, N. D. R., Cordes, J. M., Camilo, F., Nice, D. J., & Lorimer, D. R. 2004, ApJ, 605, 759
- Biggs, J. D., & Lyne, A. G. 1996, MNRAS, 282, 691
- Booth, R. S., de Blok, W. J. G., Jonas, J. L., & Fanaroff, B. 2009, arXiv:0910.2935
- Briley, M. M., Bell, R. A., Hesser, J. E., & Smith, G. H. 1994, Canadian Journal of Physics, 72, 772
- Camilo, F., Lorimer, D. R., Freire, P., Lyne, A. G., & Manchester, R. N. 2000, ApJ, 535, 975
- Camilo, F., et al. 2001, ApJ, 548, L187
- Camilo, F., & Rasio, F. A. 2005, Binary Radio Pulsars, 328, 147
- Champion, D. J., Ransom, S. M., Lazarus, P., et al. 2008, Science, 320, 1309
- Chandler, A. 2003 *Ph.D. Thesis*, Cal Tech
- Cordes, J. M., & Lazio, T. J. W. 2002, arXiv:astro-ph/0207156
- Cordes, J. M., Freire, P. C. C., Lorimer, D. R., et al. 2006, ApJ, 637, 446
- Cordes, J. M., & Shannon, R. M. 2008, ApJ, 682, 1152
- D'Amico, N., Bailes, M., Lyne, A. G., Manchester, R. N., Johnston, S., Fruchter, A. S., & Goss, W. M. 1993, MNRAS, 260, L7
- Damashek, M., Taylor, J. H., & Hulse, R. A. 1978, ApJ, 225, L31
- Deller, A. T., Tingay, S. J., Bailes, M., & Reynolds, J. E. 2009, ApJ, 701, 1243

- Deneva, J. S., Cordes, J. M., & Lazio, T. J. W. 2009, ApJ, 702, L177
- Dessart, L., Burrows, A., Ott, C. D., Livne, E., Yoon, S.-C., & Langer, N. 2006, ApJ, 644, 1063
- Dewey, R. J., Taylor, J. H., Weisberg, J. M., & Stokes, G. H. 1985, ApJ, 294, L25
- Eatough, R. P., Molkenthin, N., Kramer, M., Noutsos, A., Keith, M. J., Stappers, B. W., & Lyne, A. G. 2010, MNRAS, 407, 2443
- Faucher-Giguère, C.-A., & Kaspi, V. M. 2006, ApJ, 643, 332
- Ferraro, F. R., et al. 2009, Nature, 462, 483
- Foster, R. S., & Backer, D. C. 1990, ApJ, 361, 300
- Fregeau, J. M., Richer, H. B., Rasio, F. A., & Hurley, J. R. 2009, ApJ, 695, L20
- Freire, P. C., Camilo, F., Lorimer, D. R., Lyne, A. G., Manchester, R. N., & D'Amico, N. 2001, MNRAS, 326, 901
- Freire, P. C., Gupta, Y., Ransom, S. M., & Ishwara-Chandra, C. H. 2004, ApJ, 606, L53
- Freire, P. C. C. 2005, Binary Radio Pulsars, 328, 405
- Freire, P. C. C., Ransom, S. M., Bégin, S., Stairs, I. H., Hessels, J. W. T., Frey, L. H., & Camilo, F. 2008, ApJ, 675, 670
- Freire, P. C. C., Bassa, C. G., Wex, N., et al. 2011, MNRAS, 412, 2763
- Gnedin, O. Y., Zhao, H., Pringle, J. E., Fall, S. M., Livio, M., & Meylan, G. 2002, ApJ, 568, L23
- Gold, T. 1969, Nature, 221, 25
- Hankins, T. H., Kern, J. S., Weatherall, J. C., & Eilek, J. A. 2003, Nature, 422, 141
- Harris, W. E. 1996, AJ, 112, 1487
- Hessels, J. W. T., Ransom, S. M., Stairs, I. H., et al. 2006, Science, 311, 1901
- Hessels, J. W. T., Ransom, S. M., Stairs, I. H., Kaspi, V. M., & Freire, P. C. C. 2007, ApJ, 670, 363
- Hessels, J. W. T., Ransom, S. M., Kaspi, V. M., Roberts, M. S. E., Champion, D. J., & Stappers, B. W. 2008, 40 Years of Pulsars: Millisecond Pulsars, Magnetars and More, 983, 613
- Hewish, A., Bell, S. J., Pilkington, J. D. H., Scott, P. F., & Collins, R. A. 1968, Nature, 217, 709

- Hobbs, G., Lorimer, D. R., Lyne, A. G., & Kramer, M. 2005, MNRAS, 360, 974
- Hobbs, G., et al. 2010, Classical and Quantum Gravity, 27, 084013
- Hotan, A. W., van Straten, W., & Manchester, R. N. 2004, PASA, 21, 302
- Hui, C. Y., Cheng, K. S., & Taam, R. E. 2010, ApJ, 714, 1149
- Jacoby, B. A., Cameron, P. B., Jenet, F. A., Anderson, S. B., Murty, R. N., & Kulkarni, S. R. 2006, ApJ, 644, L113
- Johnston, S., Kramer, M., Lorimer, D. R., Lyne, A. G., McLaughlin, M., Klein, B., & Manchester, R. N. 2006, MNRAS, 373, L6
- Kaplan, D. L., et al. 2005, PASP, 117, 643
- Keane, E. F., Kramer, M., Lyne, A. G., Stappers, B. W., & McLaughlin, M. A. 2011, MNRAS, 415, 3065
- Kijak, J., Lewandowski, W., Maron, O., Gupta, Y., & Jessner, A. 2011, *Astron. Astrophys.*, 531, A16
- Kitaura, F. S., Janka, H.-T., & Hillebrandt, W. 2006, *Astron. Astrophys.*, 450, 345
- Klein, B., Kramer, M., Müller, P., & Wielebinski, R. 2004, Young Neutron Stars and Their Environments, 218, 133
- Kramer, M., Klein, B., Lorimer, D., Müller, P., Jessner, A., & Wielebinski, R. 2000, IAU Colloq. 177: Pulsar Astronomy - 2000 and Beyond, 202, 37
- Kramer, M., Lyne, A. G., Hobbs, G., et al. 2003, ApJ, 593, L31
- Kramer, M., Stairs, I. H., Manchester, R. N., et al. 2006, Science, 314, 97
- Krauss, L. M., & Chaboyer, B. 2001, arXiv:astro-ph/0111597
- Kroupa, P. 2002, Science, 295, 82
- Kurkela, A., Romatschke, P., & Vuorinen, A. 2010, Physics Review D, 81, 105021
- Lattimer, J. M., & Prakash, M. 2001, ApJ, 550, 426
- Leonard, P. J. T. 1989, AJ, 98, 217
- Li, X.-D. 2006, ApJ, 646, L139
- Liebert, J., Bergeron, P., & Holberg, J. B. 2003, AJ, 125, 348
- Lorimer, D. R., Yates, J. A., Lyne, A. G., & Gould, D. M. 1995, MNRAS, 273, 411
- Lorimer, D. R. & Kramer, M. 2005 Handbook of Pulsar Astronomy

- Luo, Q., & Melrose, D. 2007, MNRAS, 378, 1481
- Lynch, R. S., & Ransom, S. M. 2011, arXiv:1101.0763
- Lynch, R. S., Ransom, S. M., Freire, P. C. C., & Stairs, I. H. 2011, ApJ, 734, 89
- Lynch, R. S., Ransom, S. M., Freire, P. 2011, in preparation
- Lynch, R. S. 2011 in preparation
- Lyne, A. G., Brinklow, A., Middleditch, J., Kulkarni, S. R., & Backer, D. C. 1987, Nature, 328, 399
- Lyne, A. G., Biggs, J. D., Brinklow, A., McKenna, J., & Ashworth, M. 1988, Nature, 332, 45
- Lyne, A. G., Biggs, J. D., Harrison, P. A., & Bailes, M. 1993, Nature, 361, 47
- Lyne, A. G., Manchester, R. N., & D'Amico, N. 1996, ApJ, 460, L41
- Lyne, A. G., et al. 2004, Science, 303, 1153
- Manchester, R. N., Lyne, A. G., D'Amico, N., et al. 1996, MNRAS, 279, 1235
- Manchester, R. N., et al. 2001, MNRAS, 328, 17
- Manchester, R. N., Hobbs, G. B., Teoh, A., & Hobbs, M. 2005, VizieR Online Data Catalog, 7245, 0
- McCrea, W. H. 1964, MNRAS, 128, 147
- McLaughlin, M. A., et al. 2006, Nature, 439, 817
- Mieske, S., & Baumgardt, H. 2007, *Astron. Astrophys.*, 475, 851
- Morris, D. J., et al. 2002, MNRAS, 335, 275
- Paust, N. E. Q., et al. 2010, AJ, 139, 476
- Phinney, E. S. 1992, Royal Society of London Philosophical Transactions Series A, 341, 39
- Phinney, E. S. 1993, Pulsars as Physics Laboratories, 39
- Possenti, A., et al. 2011, unpublished
- Radhakrishnan, V., & Cooke, D. J. 1969, ApJ letters, 3, 225
- Ransom, S. M. 2001, *Ph.D.thesis*, Harvard University
- Ransom, S. M., Eikenberry, S. S., & Middleditch, J. 2002, AJ, 124, 1788

- Ransom, S. M., Stairs, I. H., Backer, D. C., Greenhill, L. J., Bassa, C. G., Hessels, J. W. T., & Kaspi, V. M. 2004, ApJ, 604, 328
- Ransom, S. M., Hessels, J. W. T., Stairs, I. H., Freire, P. C. C., Camilo, F., Kaspi, V. M., & Kaplan, D. L. 2005, Science, 307, 892
- Ransom, S. M., Demorest, P., Ford, J., McCullough, R., Ray, J., DuPlain, R., & Brandt, P. 2009, American Astronomical Society Meeting Abstracts, 214, #605.08
- Ridley, J. P., & Lorimer, D. R. 2010, MNRAS, 404, 1081
- Rosen, R., et al. 2010, Astronomy Education Review, 9, 010106
- Salpeter, E. E. 1955, ApJ, 121, 161
- Sayer, R. W., Nice, D. J., & Taylor, J. H. 1997, ApJ, 474, 426
- Scalo, J. M. 1986, Fund. Cosmic Phys., 11, 1
- Shapiro, I. I. 1964, Physical Review Letters, 13, 789
- Shklovskii, I. S. 1970, Sov. Astron., 13, 562
- Sieber, W. 1973, Astron. Astrophys., 28, 237
- Smits, R., Kramer, M., Stappers, B., Lorimer, D. R., Cordes, J., & Faulkner, A. 2009, Astron. Astrophys., 493, 1161
- Srinivasan, G. 1989, A&A Rev., 1, 209
- Stairs, I. H., Manchester, R. N., Lyne, A. G., et al. 2001, MNRAS, 325, 979
- Stokes, G. H., Taylor, J. H., Welsberg, J. M., & Dewey, R. J. 1985, Nature, 317, 787
- Tauris, T. M., & Manchester, R. N. 1998, MNRAS, 298, 625
- Taylor, J. H., & Huguenin, G. R. 1969, Nature, 221, 816
- Taylor, J. H., Wolszczan, A., Damour, T., & Weisberg, J. M. 1992, Nature, 355, 132
- Taylor, J. H. 1992, Philosophical Transactions of the Royal Society of London, 341, 117-134 (1992), 341, 117
- Taylor, J. H., & Cordes, J. M. 1993, ApJ, 411, 674
- Webbink, R. F. 1985, Dynamics of Star Clusters, 113, 541
- Weltevrede, P., Stappers, B. W., Rankin, J. M., & Wright, G. A. E. 2006, ApJ, 645, L149
- Wolszczan, A., Kulkarni, S. R., Middleditch, J., Backer, D. C., Fruchter, A. S., & Dewey, R. J. 1989, Nature, 337, 531

Wolszczan, A., & Frail, D. A. 1992, Nature, 355, 145

Yan, W. M., et al. 2011, MNRAS, 414, 2087